

# A New Equivalence Principle Test Using a Rotating Torsion Balance

Ki-Young Choi

A dissertation submitted in partial fulfillment of  
the requirements for the degree of

Doctor of Philosophy

University of Washington

2006

Program Authorized to Offer Degree: Physics



University of Washington  
Graduate School

This is to certify that I have examined this copy of a doctoral dissertation by

Ki-Young Choi

and have found that it is complete and satisfactory in all respects,  
and that any and all revisions required by the final  
examining committee have been made.

Chair of the Supervisory Committee:

---

Jens H. Gundlach

Reading Committee:

---

Jens H. Gundlach

---

Blayne R. Heckel

---

Gerald A. Miller

Date: \_\_\_\_\_



In presenting this dissertation in partial fulfillment of the requirements for the doctoral degree at the University of Washington, I agree that the Library shall make its copies freely available for inspection. I further agree that extensive copying of this dissertation is allowable only for scholarly purposes, consistent with "fair use" as prescribed in the U.S. Copyright Law. Requests for copying or reproduction of this dissertation may be referred to Proquest Information and Learning, 300 North Zeeb Road, Ann Arbor, MI 48106-1346, 1-800-521-0600, to whom the author has granted "the right to reproduce and sell (a) copies of the manuscript in microform and/or (b) printed copies of the manuscript made from microform."

Signature\_\_\_\_\_

Date\_\_\_\_\_



University of Washington

Abstract

A New Equivalence Principle Test Using a Rotating Torsion Balance

Ki-Young Choi

Chair of the Supervisory Committee:  
Professor Jens H. Gundlach  
Department of Physics

We used a rotating torsion balance to test the equivalence principle for Yukawa ranges from 1 m to  $\infty$ . The torsion balance was mounted on a turntable rotating with constant angular velocity. On the torsion pendulum Beryllium and Titanium test bodies were installed in a composition dipole configuration. A violation of the equivalence principle would yield to a differential acceleration of the two materials towards a source mass. For two months of data, we measured this acceleration with a sensitivity of  $5 \times 10^{-13}$  cm/s<sup>2</sup> toward local topological features and the Earth.

In addition, we analyzed the differential acceleration data toward astronomical sources. We measured the differential acceleration toward the Sun in a seven month long data run. The measured differential acceleration with a  $1\sigma$  uncertainty is

$$\Delta a^{sun}(\text{Ti-Be}) = (1.1 \pm 1.6) \times 10^{-13} \text{ cm/s}^2.$$

Furthermore, we measured the differential accelerations toward the galactic center and the cosmic microwave background dipole direction. The values with their associated  $1\sigma$  uncertainties are

$$\Delta a^{gal}(\text{Ti-Be}) = (0.4 \pm 1.7) \times 10^{-13} \text{ cm/s}^2$$

and

$$\Delta a^{CMB}(\text{Ti-Be}) = (-0.6 \pm 1.5) \times 10^{-13} \text{ cm/s}^2.$$



## TABLE OF CONTENTS

List of Figures . . . . .	iii
List of Tables . . . . .	v
Chapter 1: Introduction . . . . .	1
1.1 Equivalence Principle . . . . .	1
1.2 Motivation . . . . .	2
Chapter 2: Principles of the Measurements . . . . .	7
2.1 Torque on the Fiber . . . . .	7
2.2 Equation of Motion of the Pendulum . . . . .	9
2.3 Equivalence Principle Violating Signals . . . . .	10
2.4 Gravity Gradient Signal . . . . .	11
Chapter 3: Experimental Setup . . . . .	14
3.1 Overview of the Apparatus . . . . .	14
3.2 Pendulum . . . . .	15
3.3 Fiber Suspension System . . . . .	20
3.4 Autocollimator . . . . .	24
3.5 Turntable . . . . .	26
3.6 Gradiometer Pendulum and Gravity Gradient Compensators . . . . .	30
3.7 Environmental Monitors . . . . .	33
3.8 Shielding . . . . .	36
Chapter 4: Calibration and Data Analysis . . . . .	37
4.1 Calibration Constants . . . . .	37
4.2 Calibration of the Angular Deflection . . . . .	37
4.3 Data Taking Procedures . . . . .	39
4.4 Data Reduction . . . . .	40

4.5	Analyzing Data toward Astronomical Sources . . . . .	49
Chapter 5:	Investigation of Systematic Effects . . . . .	55
5.1	Gravity Gradient Effects . . . . .	55
5.2	Turntable Effects . . . . .	65
5.3	Tilt Effects . . . . .	66
5.4	Thermal Effects . . . . .	69
5.5	Magnetic Effects . . . . .	70
5.6	Summary of the Systematic Uncertainties . . . . .	74
Chapter 6:	The Source Integration . . . . .	75
6.1	The Source Strength . . . . .	75
6.2	The Location of the Apparatus . . . . .	77
6.3	Calculation . . . . .	77
6.4	Result and Discussion . . . . .	87
6.5	Gravity Gradients . . . . .	90
Chapter 7:	Results and Discussion . . . . .	95
7.1	Differential Acceleration in Earth's Field . . . . .	95
7.2	Differential Acceleration toward Astronomical Sources . . . . .	96
7.3	Conclusion . . . . .	101
Bibliography	. . . . .	104

## LIST OF FIGURES

Figure Number	Page
1.1 Current $2\sigma$ upper limit on new Yukawa interactions with $q_5 = B$ . . . . .	5
2.1 The simple composition dipole pendulum . . . . .	8
2.2 Top view of the simple composition dipole pendulum . . . . .	9
3.1 Overview of the Eöt-Wash III apparatus . . . . .	16
3.2 Cross-section view of the vacuum vessel on the various layers of shielding. . .	17
3.3 A 3 dimensional drawing of the Eöt-Wash III torsion pendulum . . . . .	18
3.4 The barrel shape of a test body . . . . .	21
3.5 Cutaway side view of the testbodies . . . . .	21
3.6 Schematic diagram of the magnetic damper . . . . .	23
3.7 Schematic diagram of the fiber positioner . . . . .	25
3.8 Schematic diagram of the autocollimator . . . . .	27
3.9 Schematic diagram of the turntable . . . . .	28
3.10 Cross section of the active thermal expansion foot . . . . .	30
3.11 Thermal model and flow chart of the simplified feed back loop . . . . .	31
3.12 Gradiometer pendulum . . . . .	32
3.13 A 3 dimensional drawing of all gravity gradient compensators . . . . .	34
4.1 Dynamic calibration . . . . .	38
4.2 An example of the raw data. . . . .	40
4.3 Data reduction and fits . . . . .	42
4.4 The data recorded during an earthquake. . . . .	44
4.5 One day data set . . . . .	45
4.6 A typical data set taken with two different pendulum orientations . . . . .	50
4.7 The $1\omega$ signals . . . . .	51
4.8 The $1\omega$ offset signals . . . . .	52
4.9 Cumulative results toward the Sun . . . . .	53
4.10 Cumulative results toward the galactic center . . . . .	54

5.1	The gradiometer pendulum in two configurations . . . . .	56
5.2	$Q_{21}$ measurements . . . . .	58
5.3	$Q_{31}$ measurements . . . . .	60
5.4	The deflection angle of the pendulum during tuning iterations . . . . .	62
5.5	The compensators configuration for the $q_{21}$ and $q_{31}$ measurements . . . . .	63
5.6	The tilt signal on bottom titlt sensor . . . . .	68
5.7	A picture of the setup of the temperature gradient test . . . . .	70
5.8	Temperature gradient mesurements . . . . .	71
5.9	Dependence of the signal on the temperature gradient . . . . .	72
5.10	Magnetic test . . . . .	73
6.1	The cyclotron room . . . . .	80
6.2	The CENPA building . . . . .	81
6.3	Topology 20 m around the pendulum . . . . .	83
6.4	Topology 8 km around the pendulum . . . . .	84
6.5	Preliminary Reference Earth Model . . . . .	86
6.6	The magnitude and direction of $ \vec{I}_\perp $ for $q_5=B$ . . . . .	89
7.1	New $2\sigma$ upper limit on the Yukawa interactions with $q_5 = B$ . . . . .	103

## LIST OF TABLES

Table Number	Page
3.1 The properties of the test bodies. . . . .	20
3.2 The location of the temperature senors. . . . .	35
4.1 The summary of the calibration runs. . . . .	39
4.2 The summary of the attenuation factors and phase shifts. . . . .	48
5.1 Calculated values of mass moments of the gradiometers and compensators. .	57
5.2 The summary of the $Q_{21}$ measurements. . . . .	57
5.3 The summary of the $Q_{31}$ measurements. . . . .	59
5.4 Progression of the tuning procedure of the pendulum moment. . . . .	61
5.5 Summary of the measurements of $q_{21}$ moments of the pendulum. . . . .	63
5.6 Summary of the measurements of $q_{31}$ moments of the pendulum. . . . .	64
5.7 Summary of the residual $Q_{21}$ and $Q_{31}$ fields. . . . .	64
5.8 The expected signals from gravity gradient fields. . . . .	65
5.9 The summary of the tilt angles. . . . .	66
5.10 The summary of the tilt sensitivities. . . . .	67
5.11 The expected signals of the tilt effect. . . . .	69
5.12 Systematic uncertainty budget for the angular deflection angle. . . . .	74
6.1 The significant effective masses of the cyclotron room. . . . .	78
6.2 The density and the charge-to-mass ratio ( $B/\mu$ and $L/\mu$ ) of the sources. . .	79
6.3 Description of the digitized contour maps. . . . .	81
6.4 Contributions (in %) to $ \vec{I}_\perp $ for $q_5 = B$ . . . . .	85
6.5 The charge-mass ratio of the earth. . . . .	87
6.6 Source strength of Eöt-Wash III experiment. . . . .	88
6.7 The calculated values of $Q_{lm}$ . . . . .	92
6.8 Contributions (in %) to gravity gradient fields $Q_{21}$ and $Q_{31}$ . . . . .	93
6.9 The comparison of the result with measured gravity gradient fields. . . . .	94

7.1	The summary of data taking sequence.	95
7.2	The summary of results for analyzing toward the Earth (included local masses).	96
7.3	The combined signals from the systematic effect corrections.	97
7.4	The result corrected with the systematic effects.	97
7.5	The summary of results for analyzing toward the Sun.	98
7.6	The summary of results for analyzing toward the galactic center.	99
7.7	The summary of results for analyzing toward the direction of the cosmic microwave background (CMB) dipole.	100

## ACKNOWLEDGMENTS

It is a pleasure to acknowledge the debt, both personal and scientific, I owe to so many people over the past several years as a graduate student.

It has been an exciting experience to work with Professor Jens Gundlach, whose insight and breadth of knowledge in physics have inspired and encouraged me as years evolved. His style of setting extremely high scientific standards and living up to it has left indelible marks on me. This thesis could not have finished without his guidance and corrections. Special thanks to Dr. Stephan Schlamminger, for his mentorship and friendship. He was there to discuss my personal and scientific problems in a most tolerant way. His wise suggestions and clear point of view and technical skills gave me support in many ways. Many thanks to Professor Eric Adelberger for not only having shared his wide knowledge of experimental and theoretical physics, but constructing and writing the whole package of the data analysis programs which was so important to this experiment. I would like to express special thanks to Professor Blayne Heckel for his time and expertise with me whenever I was at a loss with complexities of physics. I would like to thank Dr. Erik Swanson for having designed and built most of the electronics used in this experiment, as well as the data acquisition program. I also thank Dr. Steve Merkowitz and Dr. Ulrich Schmitz for having designed and built the data acquisition program and the active thermal extension leveling system.

I am thankful to Professors Kurt Snover and Gerald Miller who have graciously agreed to serve my supervisory committee. I would like to thank to Dr. C.D. Hoyle and Ted Cook for being great officemates and group members. In addition, I thank to Hank Simon, Jim Elms, David Hyde and Ron Musgrave for machining the precision pieces with extreme accuracy. Furthermore, I want to thank the staff of CENPA Barbara Fulton, Kate Higgins, Dick

Seymour and Doug Will for their support. Thanks to Greg Harper, Duncan Prindle and Erik Mohrmann who spent a lot of time playing volley ball with me in summer times. They made my life much more enjoyable and healthier at CENPA. Special thanks to Antonino Miceli for his friendship and all of our conversation about physics and personal problems for my entire graduate student life.

I would like to express my gratitude to my mother for her love, patience, encouragement and support. I am also grateful to my brother, sister and their family for their love and support. Finally, my deepest thanks go to my wife Sangyi Lee for her love and support and for waiting for me until I finished, and for Sung-Moo Choi.

## **DEDICATION**

To my parents



# Chapter 1

## INTRODUCTION

### 1.1 Equivalence Principle

Generally, we can describe the Equivalence Principle in two different ways. The first way is Newton's view. Following Newton's definition, the Equivalence Principle states that all objects fall with the same acceleration in a uniform gravitational field (the Universality of Free Fall). In other words, inertial and gravitational mass are identical. Gravitational mass is given by Newton's law of gravitation:

$$\vec{F}_{12} = G \frac{m_{g1} m_{g2}}{r_{12}^2} \hat{r}_{12}. \quad (1.1)$$

where  $\vec{F}_{12}$  is the gravitational force between two point masses which have a separation  $r_{12}$ ,  $G$  is the gravitational constant,  $m_{gj}$  refers to the gravitational mass of the  $j$ th object and  $\hat{r}_{12}$  is the unit vector pointing from mass 1 to mass 2. The inertial mass given by Newton's second law,

$$\vec{F} = m_i \vec{a}. \quad (1.2)$$

where  $\vec{F}$  is the applied force,  $\vec{a}$  is the acceleration of the object, and  $m_i$  is the inertial mass. Therefore, if  $m_i = m_g$ , the acceleration is the same for all bodies in a homogeneous gravitational field.

The other way to describe the Equivalence Principle is Einstein's view. In 1915, Einstein derived General Relativity which extended Newton's law of gravity. The so-called Einstein Equivalence Principle states that there is no difference between a uniformly accelerated reference frame and a homogeneous gravitational field. In other words, there is no physics experiment which can distinguish between a uniformly accelerated reference frame and a

homogeneous gravitational field. Because Einstein derived his theory of General Relativity from the Equivalence Principle, we can say that the Equivalence Principle is the foundation of General Relativity. In the decades following Einstein's discovery of the General Relativity, many other alternative metric theories of gravity have been postulated. Most of them, however, obey the Equivalence Principle.

## 1.2 Motivation

### 1.2.1 New Microscopic Composition Dependent Interaction

A new composition dependent interaction can be described by a Yukawa potential,

$$V_{12}(r) = \mp \frac{g^2}{4\pi} (q_5)_1 (q_5)_2 \frac{e^{-r/\lambda}}{r}, \quad (1.3)$$

where  $g$  is a coupling constant,  $q_5$  denotes the "charge" of a test particle,  $\lambda = \hbar/m_b c$  is the Compton wavelength of the virtual exchange boson, and the minus and plus signs refer to interactions mediated by scalar or vector bosons, respectively.

The differential acceleration between two test particles 1 and 2 toward a source S is

$$\Delta \vec{a} = \mp \frac{g^2}{4\pi u} (q_5)_s \Delta \left( \frac{q_5}{\mu} \right) \left( 1 + \frac{r}{\lambda} \right) \frac{e^{-r/\lambda}}{r^2} \hat{r}, \quad (1.4)$$

where  $u$  is the atomic mass unit,  $\Delta \vec{a} = \vec{a}_1 - \vec{a}_2$ ,  $\Delta \left( \frac{q_5}{\mu} \right) = \left( \frac{q_5}{\mu} \right)_1 - \left( \frac{q_5}{\mu} \right)_2$ ,  $\mu$  is the mass divided by atomic mass units,  $\left( \frac{q_5}{\mu} \right)$  denotes the charge-to-mass ratio, and  $(q_5)_s$  is the "charge" of the source mass. Therefore, the differential acceleration between two test bodies is proportional to the difference in charge-to-mass ratio of the test bodies. We have no bias as to what the "charge" of the Equivalence Principle violating interaction should be, but we assume the "charge" should be a function of the quantum numbers of its constituents. The most general vector charge of electrically neutral and stable matter is described as:

$$q_5 = B \cos \theta_5 + L \sin \theta_5, \quad (1.5)$$

where  $B$  is the baryon number,  $L$  is the lepton number, and  $\theta_5$  is a parameter that can have any value from  $-\frac{\pi}{2}$  to  $\frac{\pi}{2}$ . Of special interest is  $q_5 = B$  or  $q_5 = L$ , since they are conserved

quantum numbers in many theories. In addition  $q_5 = B - L$  is interesting, because this number is conserved in grand unified theories, which do not conserve B or L individually. Moreover, we are interested in other combinations of B and L such as  $q_5 = B - 2L$  or  $q_5 = 3B + L$  because  $B - 2L$  is isospin and  $3B + L$  counts the number of elementary fermions.

Theories containing scalar interactions are probably the most natural extensions of general relativity. For example, all string theories predict a scalar partner of the tensor graviton (the dilaton), both of which arise as products of left-moving and right-moving excitations of the string. A massless dilaton is usually rejected because it would produce large violation of the Equivalence Principle. However, Damour and Polyakov[1] discuss a string theory scenario containing a massless dilation that nevertheless generates a very small violation of the Equivalence Principle. They argue that string-loop modifications of the dilaton-matter couplings may provide a mechanism whereby cosmological evolution drives the dilaton to couple to matter so weakly that it could not have been detected in existing Equivalence Principle tests. This motivates us to perform more sensitive tests of the Equivalence Principle.

### *1.2.2 Dark Matter and Dark Energy*

From modern cosmology, we learn that the sum of all ordinary matter (i.e. luminous matter) is only about 4% of the critical value which is predicted for the current universe model. The missing 96% of energy is dark matter (23%) and dark energy (73%)[2]. Below, we will discuss how testing the Equivalence Principle could help understand dark matter and energy.

#### *The Galactic Dark Matter Problem*

The flat rotation curve<sup>1</sup> of the spiral galaxies cannot be explained by the gravitational attraction of the luminous matter[3][4]. Galactic dark matter provides an explanation of this discrepancy. Not much is known about galactic dark matter, except that it attracts ordinary matter and other dark matter and deflects photons. If there is a long range

---

<sup>1</sup>the relation between the rotational speed and radial distance

interaction between ordinary matter and dark matter other than gravity, it will violate the Equivalence Principle.

### *Dark Energy: Cosmological Scalar Fields*

One possible scenario for the dark energy is a scalar field[1][5][6]. A slowly-rolling scalar field would provide most of the energy density in the current universe. These so-called quintessence fields are normally assumed to couple to ordinary matter only gravitationally. However, Carroll[7] argues that one expects our low-energy universe to be governed by an effective theory where the unification-scale degrees of freedom are integrated out, leaving non-renormalizable Equivalence Principle violating interactions of the scalar field,  $\phi$ , to ordinary matter (the Standard Model particles). Although such couplings are suppressed by the appropriate powers of the unification mass  $M$ , he considers a coupling  $\beta(\phi/M)Tr(G_{\mu\nu}G^{\mu\nu})$  and showed how to analyze previous Equivalence Principle tests[8] with  $\beta$ , where  $G_{\mu\nu}$  is the field strength tensor of QCD, and  $\beta$  is a dimensionless coupling which is expected to be of order unity.

#### *1.2.3 Current Constraints of the Equivalence Principle Test*

We can rewrite Equation 1.3 for a Yukawa potential as

$$V_{AB}(r) = \alpha_5 \left( \frac{q_5}{\mu} \right)_1 \left( \frac{q_5}{\mu} \right)_2 G \frac{m_1 m_2}{r} e^{-r/\lambda}, \quad (1.6)$$

where  $\alpha_5 = \mp g^2/(4\pi u^2 G)$ ,  $u$  is the atomic mass unit. There are three parameters in this expression; the coupling strength  $\alpha_5$ , the interaction range  $\lambda$ , and the charge  $q_5$ . We used these parameters to set the limit on the new Yukawa interaction. Figure 1.1 shows the current  $2\sigma$  upper limit on new Yukawa interactions with  $q_5 = B$ .

#### *1.2.4 Goals of this Experiment*

Tests of the Equivalence Principle probe the classic Universality of Free Fall parameter:

$$\eta(A, B) = \frac{\Delta a}{a_s} = \frac{(m_g/m_i)_A - (m_g/m_i)_B}{[(m_g/m_i)_A + (m_g/m_i)_B]/2} \approx \left( \frac{m_g}{m_i} \right)_A - \left( \frac{m_g}{m_i} \right)_B \quad (1.7)$$

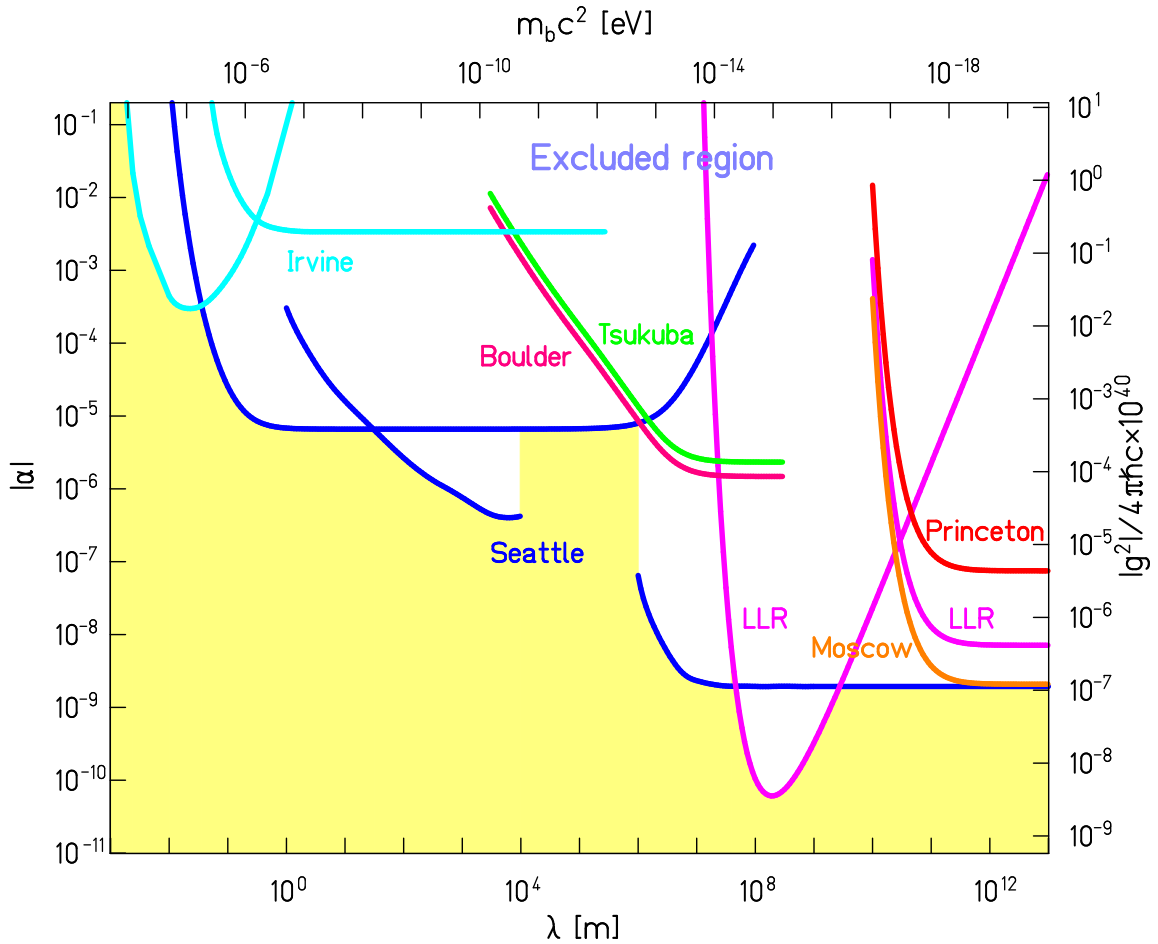


Figure 1.1: Current  $2\sigma$  upper limit on the Yukawa interactions with  $q_5 = B$ . The experimentally allowed region is shaded. The region excluded by previous results is labeled as follows: Seattle[8][9], Irvine[10][11], Tsukuba[12], Boulder[13], Moscow[14], Princeton[15], and LLR[16].

where  $\Delta a$  is the differential acceleration between two test masses  $A$  and  $B$  toward a source mass and  $a_s$  is the acceleration toward the source mass.

We measured the differential acceleration between masses of different composition. We determined the parameter  $\eta$  toward local masses, the Earth, the Sun and Galactic Dark Matter.

## Chapter 2

### PRINCIPLES OF THE MEASUREMENTS

Our instrument to test Equivalence Principle is the torsion balance. In this chapter, we discuss the principle of the measurement.

#### 2.1 Torque on the Fiber

Figure 2.1 shows a simple torsion pendulum consisting of test masses made of two different materials located at  $r_1$  and  $r_2$ , where  $F_1$  and  $F_2$  are the net forces on the two test masses. The fiber direction of the pendulum is opposite to the direction of the sum of the two net forces acting on the test masses and is given by:

$$\hat{n} = -\frac{(\vec{F}_1 + \vec{F}_2)}{|\vec{F}_1 + \vec{F}_2|}. \quad (2.1)$$

The torque on the fiber of the simple torsion pendulum is

$$\vec{\tau} = \vec{r}_1 \times \vec{F}_1 + \vec{r}_2 \times \vec{F}_2, \quad (2.2)$$

and the magnitude of the torque about the fiber axis can be expressed as

$$\tau = (\vec{r}_1 \times \vec{F}_1 + \vec{r}_2 \times \vec{F}_2) \cdot \hat{n} \quad (2.3)$$

$$= \frac{(\vec{F}_1 \times \vec{F}_2) \cdot \vec{r}_1 - (\vec{F}_1 \times \vec{F}_2) \cdot \vec{r}_2}{|\vec{F}_1 + \vec{F}_2|} \quad (2.4)$$

$$= \frac{(\vec{F}_1 \times \vec{F}_2) \cdot \vec{r}}{|\vec{F}_1 + \vec{F}_2|} \quad (2.5)$$

where  $\vec{r} = \vec{r}_1 - \vec{r}_2$ . Therefore the torque about the fiber of the simple torsion pendulum is

$$\vec{\tau} = \frac{(\vec{F}_1 \times \vec{F}_2) \cdot \vec{r}}{|\vec{F}_1 + \vec{F}_2|} \hat{n}. \quad (2.6)$$

This torque depends on the angle between the two forces acting on the test masses. In

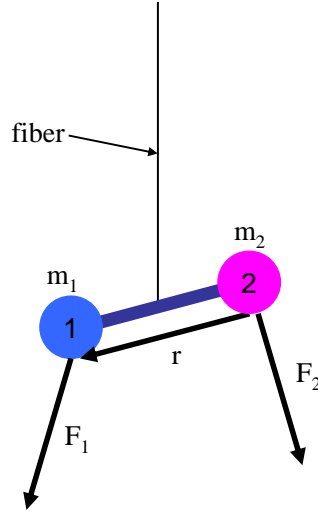


Figure 2.1: The simple composition dipole pendulum

addition if the forces on two test masses and  $\vec{r}$  lie in the same plane, there is no torque about the fiber. Therefore, the torsion balance is sensitive only to differential horizontal acceleration of the test masses. Figure 2.2 shows the top view of a simple composition dipole pendulum consisting of two test masses made of different materials and identical masses  $m$  and with a separation  $r$ . Then, the torque about the fiber can be expressed as:

$$\vec{\tau} = \frac{1}{2} m \vec{r} \times \Delta \vec{a}_\perp \quad (2.7)$$

$$= \frac{1}{2} m r (-\Delta a_x \sin \phi_d + \Delta a_y \cos \phi_d) \hat{z} \quad (2.8)$$

$$= \frac{1}{2} m r (-|\Delta a_\perp| \cos \phi_a \sin \phi_d + |\Delta a_\perp| \sin \phi_a \cos \phi_d) \hat{z} \quad (2.9)$$

$$= \frac{1}{2} m r |\Delta a_\perp| \sin(\phi_a - \phi_d) \hat{z} \quad (2.10)$$

where  $\Delta \vec{a}_\perp = (\vec{a}_1 - \vec{a}_2)_\perp$  is the horizontal differential acceleration between the two test masses,  $\phi_a$  is the angle of  $\Delta \vec{a}_\perp$  and  $\phi_d$  is the direction of the composition dipole with respect to the x coordinate, and  $\hat{z}$  is the direction along the fiber.

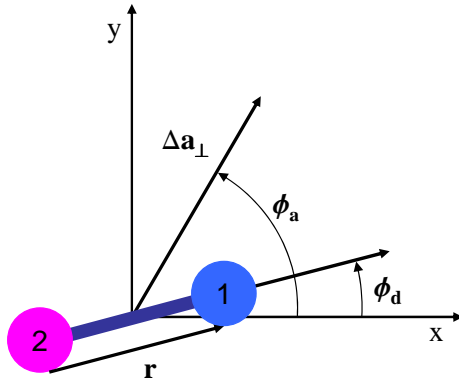


Figure 2.2: Top view of the simple composition dipole pendulum

## 2.2 Equation of Motion of the Pendulum

In our instrument, the torsion pendulum is suspended from an air bearing turntable by a tungsten fiber. The turntable is rotated with a constant angular speed  $\omega$ . Generally, the equation of motion of the pendulum in the lab frame is described by:

$$I\ddot{\Theta} + 2I\gamma(\dot{\Theta} - \dot{\phi}) = T(t) - \kappa(1 + i\epsilon)(\Theta - \phi), \quad (2.11)$$

where  $\Theta$  denotes the pendulum angle in the lab frame,  $\phi = \omega t$  is the turntable angle in the lab frame,  $I$  is a moment of inertia of the pendulum,  $\gamma$  is viscous damping coefficient,  $\kappa$  is a spring constant of the fiber,  $\epsilon = 1/Q$  is the inelastic loss angle,  $Q$  is the quality factor of the fiber, and  $T$  is an external torque on the pendulum. We define  $\theta = \Theta - \phi$  to be the angle of the pendulum in the rotating frame. The equation of motion of the pendulum in the rotating frame can be rewritten as:

$$\ddot{\theta} + 2\gamma\dot{\theta} + \omega_0^2(1 + i\epsilon)\theta = T(t)/I, \quad (2.12)$$

where  $\omega_0^2 = \kappa/I$ . In the rotating frame the torques on the pendulum can be expanded in Fourier coefficients. Thus

$$T(t) = \sum_{n=0}^{\infty} T_{0n} e^{i\omega_n t}, \quad (2.13)$$

where  $\omega_n = n\omega$ . The general solution of Equation 2.12 is:

$$\theta(t) = \theta_0 e^{-\gamma t} e^{i\sqrt{\omega_0^2 - \gamma^2 + i\epsilon\omega_0^2} t} + \sum_{n=0}^{\infty} \frac{\omega_0^2}{\omega_0^2 - n^2\omega^2 + i(2n\gamma\omega + \epsilon\omega_0^2)} \frac{T_{0n}}{\kappa} e^{in\omega t}. \quad (2.14)$$

In the ideal case where there is no free torsional oscillation ( $\theta_0 = 0$ ), the solution is:

$$\theta(t) = \sum_{n=0}^{\infty} \frac{\omega_0^2}{\omega_0^2 - n^2\omega^2 + i(2n\gamma\omega + \epsilon\omega_0^2)} \frac{T_{0n}}{\kappa} e^{in\omega t} \quad (2.15)$$

$$= \sum_{n=0}^{\infty} \frac{T_n(t)}{\kappa}, \quad (2.16)$$

where

$$T_n(t) = \frac{\omega_0^2}{\omega_0^2 - n^2\omega^2 + i(2n\gamma\omega + \epsilon\omega_0^2)} T_{0n} e^{in\omega t}. \quad (2.17)$$

### 2.3 Equivalence Principle Violating Signals

We test the Equivalence Principle by measuring the differential horizontal acceleration of two test masses. The differential horizontal acceleration of the test mass is given by:

$$\Delta a_{\perp} = \Delta \left( \frac{m_g}{m_i} \right) a_{source}, \quad (2.18)$$

where  $m_g$  and  $m_i$  are the gravitational and the inertial mass, and  $a_{source}$  denotes the acceleration toward the source mass.

According to Equation 2.10 and Equation 2.16, the angle of the pendulum is given by

$$\theta(t) = \frac{\frac{1}{2} mr |\Delta a_{\perp}|}{\kappa} \sin(\phi_a - \phi_d). \quad (2.19)$$

Let us consider  $\alpha$  to be the direction of the composition dipole in the rotating frame. Thus,

$$\theta = \frac{\frac{1}{2}mr|\Delta a_{\perp}|}{\kappa} \sin(\phi_a - \alpha - \phi) \quad (2.20)$$

where  $\phi_d = \alpha + \phi$  and  $\alpha$  is a constant. In our experiment, we measured  $\theta$  as a function of  $\phi$ . The harmonics of  $\theta(\phi)$  at the turntable rotation frequency is

$$\theta(\phi) = a_1 \sin(\phi_1 - \phi) \quad (2.21)$$

$$= a_1 \sin \phi_1 \cos(-\phi) + a_1 \cos \phi_1 \sin(-\phi) \quad (2.22)$$

$$= a_1^s \sin(-\phi) + a_1^c \cos(-\phi) \quad (2.23)$$

where

$$a_1 = \frac{\frac{1}{2}mr|\Delta a_{\perp}|}{\kappa} \quad (2.24)$$

$$\phi_1 = \phi_a - \alpha \quad (2.25)$$

$$a_1^s = a_1 \cos \phi_1 \quad (2.26)$$

$$a_1^c = a_1 \sin \phi_1. \quad (2.27)$$

## 2.4 Gravity Gradient Signal

The gravitational potential energy for two test masses separated by  $r_{12}$  is given by:

$$V_{12}(r) = -G \frac{m_1 m_2}{r_{12}}. \quad (2.28)$$

We can generalize the gravitational potential energy between the pendulum and the arbitrary source masses with

$$V_{PS} = -G \int d^3r \rho_p(\vec{r}) \int d^3r' \rho_s(\vec{r}') \frac{1}{|\vec{r} - \vec{r}'|}, \quad (2.29)$$

where  $\rho_p(\vec{r})$  and  $\rho_s(\vec{r}')$  denote the mass distribution densities of the pendulum and the source mass. We expand  $1/|\vec{r} - \vec{r}'|$  in a multipole expansion:

$$\frac{1}{|\vec{r} - \vec{r}'|} = 4\pi \sum_{l=0}^{\infty} \sum_{m=-l}^l \frac{1}{2l+1} \frac{r^l}{r'^{l+1}} Y_{lm}^*(\hat{r}) Y_{lm}(\hat{r}') \quad (2.30)$$

then,

$$V_{PS} = -4\pi G \sum_{l=0}^{\infty} \frac{1}{2l+1} \sum_{m=-l}^l \int d^3r \rho_p(\vec{r}) r^l Y_{lm}^*(\hat{r}) \int d^3r' \frac{\rho_s(\vec{r}')}{r'^{l+1}} Y_{lm}(\hat{r}') \quad (2.31)$$

$$= -4\pi G \sum_{l=0}^{\infty} \frac{1}{2l+1} \sum_{m=-l}^l q_{lm} Q_{lm} \quad (2.32)$$

where

$$q_{lm} = \int d^3r \rho_p(\vec{r}) r^l Y_{lm}^*(\hat{r}), \quad (2.33)$$

and

$$Q_{lm} = \int d^3r' \frac{\rho_s(\vec{r}')}{r'^{l+1}} Y_{lm}(\hat{r}'). \quad (2.34)$$

The  $q_{lm}$  are called the gravity gradient moments. These integrals contain only the properties of the pendulum. The  $Q_{lm}$  are called the gravity gradient fields and contain only information about the source mass distribution.

For notational convenience, we can transform the gravity gradient moments from the lab frame ( $\vec{r}$ ) to the rotating frame ( $\vec{r}_1$ ):  $q_{lm}(\vec{r}) \rightarrow \bar{q}_{lm}(\vec{r}_1)$ ,  $r = r_1$ ,  $Y_{lm}^*(\hat{r}) = Y_{lm}^*(\hat{r}_1) e^{-im\phi}$ .

$$q_{lm} = \bar{q}_{lm} e^{-im\phi}, \quad (2.35)$$

where

$$\bar{q}_{lm} = \int d^3r_1 \rho_p(\vec{r}_1) r_1^l Y_{lm}^*(\hat{r}_1). \quad (2.36)$$

Then the torque about the fiber of the pendulum is given by:

$$\tau = -\frac{\partial V}{\partial \phi} \quad (2.37)$$

$$= -4\pi i G \sum_{l=0}^{\infty} \frac{1}{2l+1} \sum_{m=-l}^l m \bar{q}_{lm} Q_{lm} e^{-im\phi}. \quad (2.38)$$

The twist angle of the fiber, not taking into account the attenuation of the pendulum, due to the torque is

$$\theta = \frac{\tau}{\kappa} \quad (2.39)$$

$$= -\frac{4\pi i G}{\kappa} \sum_{l=0}^{\infty} \frac{1}{2l+1} \sum_{m=-l}^l m \bar{q}_{lm} Q_{lm} e^{-im\phi}. \quad (2.40)$$

Because  $Y_{l(-m)} = (-1)^m Y_{lm}^*$ ,  $\bar{q}_{l(-m)} = (-1)^m \bar{q}_{lm}^*$  and  $Q_{l(-m)} = (-1)^m Q_{lm}^*$ .

$$\sum_{m=-l}^0 m \bar{q}_{lm} Q_{lm} e^{-im\phi} = \sum_{m=0}^l (-m) \bar{q}_{l(-m)} Q_{l(-m)} e^{im\phi} \quad (2.41)$$

$$= \sum_{m=0}^l (-m) \bar{q}_{lm}^* Q_{lm}^* e^{im\phi} \quad (2.42)$$

we can describe  $\theta$  as  $\theta_l^m$

$$\theta_l^m = -\frac{4\pi i G}{\kappa} \sum_{l=0}^{\infty} \frac{1}{2l+1} \sum_{m=1}^l m (\bar{q}_{lm} Q_{lm} e^{-im\phi} - \bar{q}_{lm}^* Q_{lm}^* e^{im\phi}) \quad (2.43)$$

$$= \frac{8\pi G}{\kappa} \sum_{l=0}^{\infty} \frac{1}{2l+1} \sum_{m=1}^l m \operatorname{Im}(\bar{q}_{lm} Q_{lm} e^{-im\phi}) \quad (2.44)$$

$$= \frac{8\pi G}{\kappa} \sum_{l=0}^{\infty} \frac{1}{2l+1} \sum_{m=1}^l m |\bar{q}_{lm}| |Q_{lm}| \sin(\phi_{\bar{q}_{lm}} + \phi_{Q_{lm}} - m\phi). \quad (2.45)$$

We are interested in the  $1\omega$  ( $m = 1$ ) signal.

$$\theta_l^{m=1} = \frac{8\pi G}{\kappa} \sum_{l=0}^{\infty} \frac{1}{2l+1} |\bar{q}_{l1}| |Q_{l1}| \sin(\phi_{\bar{q}_{l1}} + \phi_{Q_{l1}} - \phi). \quad (2.46)$$

## Chapter 3

### **EXPERIMENTAL SETUP**

#### **3.1 Overview of the Apparatus**

Our apparatus (Figure 3.1), called Eöt-Wash III, is located in the old cyclotron cave at the Center for Experimental Nuclear Physics and Astrophysics (CENPA). The CENPA building is located in the northeast corner of the campus of the University of Washington at a longitude of  $122.30^\circ$  West and latitude of  $47.66^\circ$  North. Our pendulum is located 76.2 cm from the wall on the west side of the cyclotron room and 241.3 cm above the floor (28.626 m above the sea level). A composition dipole pendulum is suspended from an 107.4 cm long 20  $\mu\text{m}$  diameter tungsten torsion fiber inside a vacuum vessel.

The entire vacuum vessel, including rotating thermal and magnetic shields, is suspended from an air-bearing turntable, which is rotating at a constant rate of about one revolution per 20 minutes. To measure the angular variation of the pendulum, an autocollimator is attached to the vacuum chamber. A collimated laser beam is reflected from a mirror on the pendulum and detected on a position sensitive photo-diode detector. The pressure inside the vacuum vessel is kept with an ion pump to better than  $1 \times 10^{-6}$  Torr during data taking. Two layers of magnetic shielding are mounted inside the vacuum vessel. To minimize systematic effects, a number of shields are installed inside and outside the vacuum chamber. On the inside, we have installed a magnetic and thermal shield both rotating with the vacuum chamber. In addition, a stationary magnetic and thermal shield is placed around the apparatus. A detail view of the shields is shown in Figure 3.2.

We use three different gravity gradient compensators ( $Q_{21}$ ,  $Q_{31}$ , and  $Q_{22}$ ) to null the gravity gradient effects which are due to our local source distribution. The compensators are installed outside the stationary thermal shield on a separate stand. All compensators

can be moved to different heights and each compensator can be rotated around the fiber axis.

To study systematic effects, we monitored 25 sensors. We recorded temperature at 15 different locations of the apparatus using temperature sensors (Analog Devices, Model 590). In addition, we monitored the tilt of the apparatus using two electronic tilt sensors (Applied Geomechanics Instruments, Model 755-1129) on the rotating platform, and one stationary electronic tilt sensor. We measured the pressure from the ion pump and the error signal from the feedback loop which was used to keep the turntable rotating at constant velocity.

### **3.2 Pendulum**

The most important part of the apparatus is the torsion pendulum, as shown in Figure 3.3. The Eöt-Wash III torsion pendulum consisted of eight test bodies and a pendulum body to which the eight test bodies are attached. The pendulum body is made from aluminum and is described in the next section. The eight test bodies are used to construct a composition dipole. Four test bodies are made from one material and the other four from another material. We have three sets of test bodies, made from beryllium, titanium and aluminum.

The pendulum is designed highly symmetrically. The center of mass of the pendulum is at the symmetry center of the pendulum. The pendulum itself has no multipole moments up to  $l=5$  by the design, except for the  $q_{00}$  moment (the mass) and the  $q_{44}$  moment which reflects its fourfold rotational symmetry. The total mass of the pendulum is  $70.2802 \pm 0.0001$  g. The height of the pendulum is  $7.8875 \pm 0.0005$  cm and the center of test bodies were located at  $2.9540 \pm 0.0005$  cm from the center of the pendulum and the horizontal distance between the two test bodies nearby is  $3.7680 \pm 0.0005$  cm. The calculated moment of inertia of the pendulum is  $377.33$  g/cm<sup>2</sup>.

#### *3.2.1 Pendulum Body*

The pendulum consists of an aluminum body, four mirrors, eight cone shape test body holders, 8 tuning screws and 2 fiber screws. The middle body part has a cylindrical shape

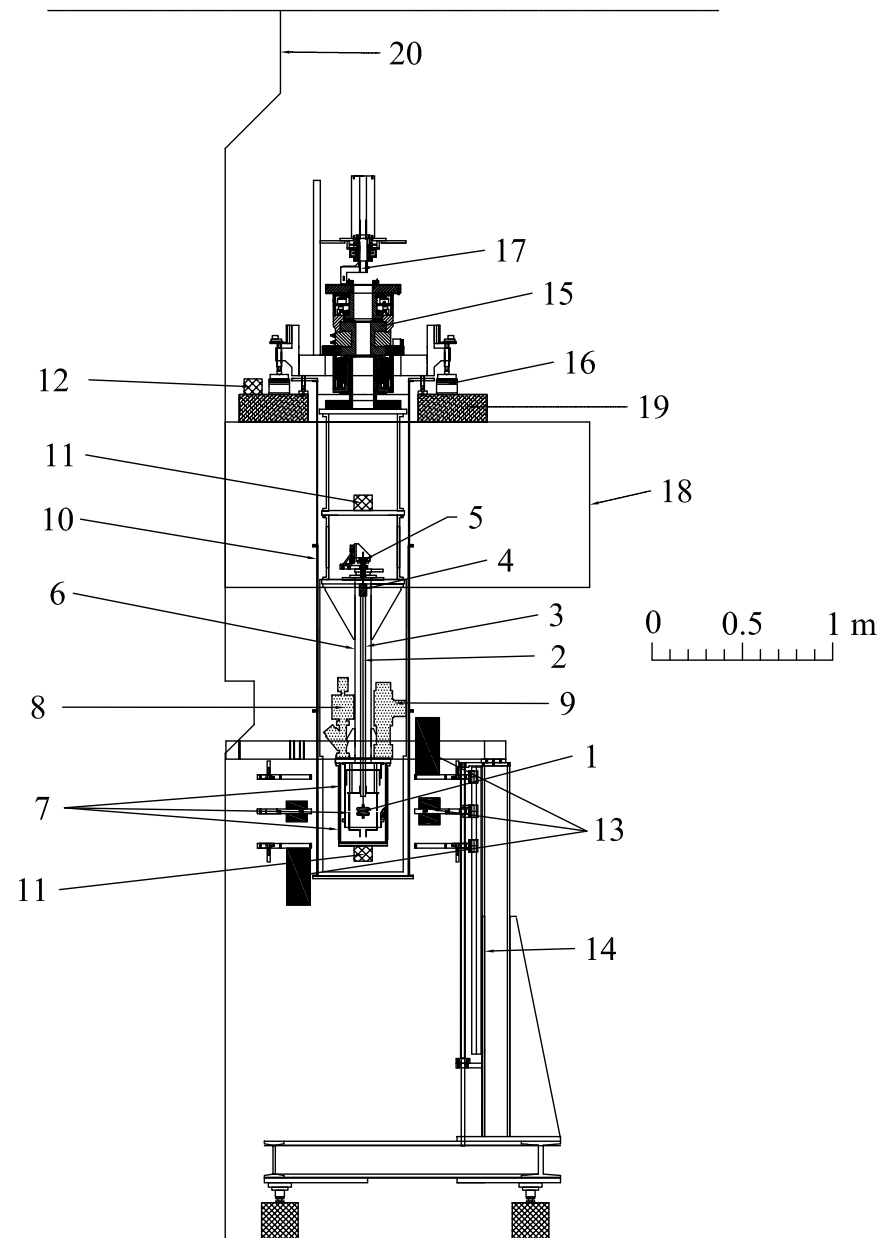


Figure 3.1: Overview of the Eöt-Wash III Apparatus. 1: pendulum, 2: torsion fiber, 3: heat shroud, 4: magnetic damper, 5: fiber positioner, 6: vacuum vessel, 7: rotational magnetic shields, 8: ion pump, 9: autocollimator, 10: stationary thermal shields and magnetic shield, 11: rotational tilt sensors, 12: stationary tilt sensor, 13: gravity gradient compensators, 14: compensator stand, 15: turn table, 16: thermal activated feet, 17: cable co-rotator, 18: concrete support attached on the wall of the cyclotron room, 19: concrete base plate, 20: wall of the cyclotron room.

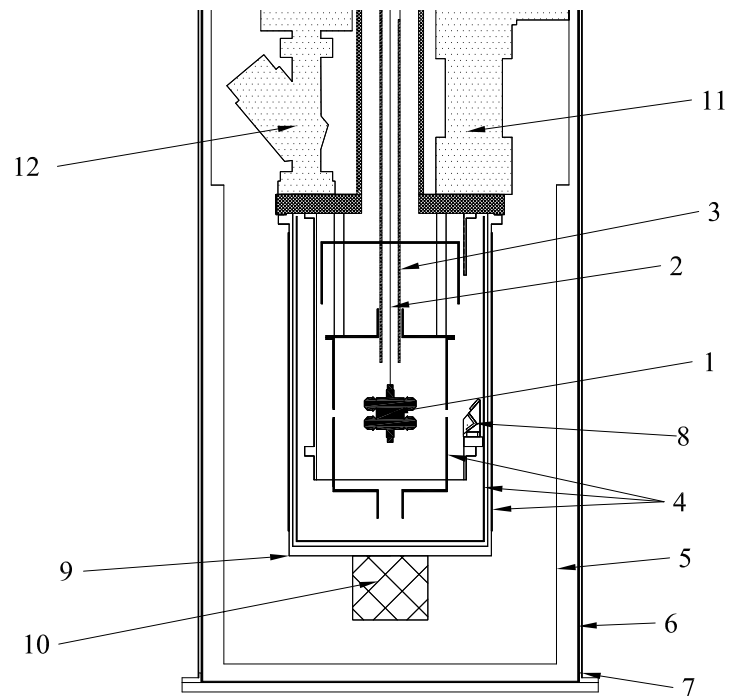


Figure 3.2: Cross-section view of the vacuum vessel on the various layers of shielding. 1: pendulum, 2: torsion fiber, 3: heat shroud, 4: co-rotating magnetic shields, 5: co-rotating thermal shield, 6: stationary magnetic shield , 7: stationary thermal shield, 8: the laser beam optics mirrors, 9: vacuum vessel, 10: co-rotating tilt sensors, 11: autocollimator, 12: ion pump.

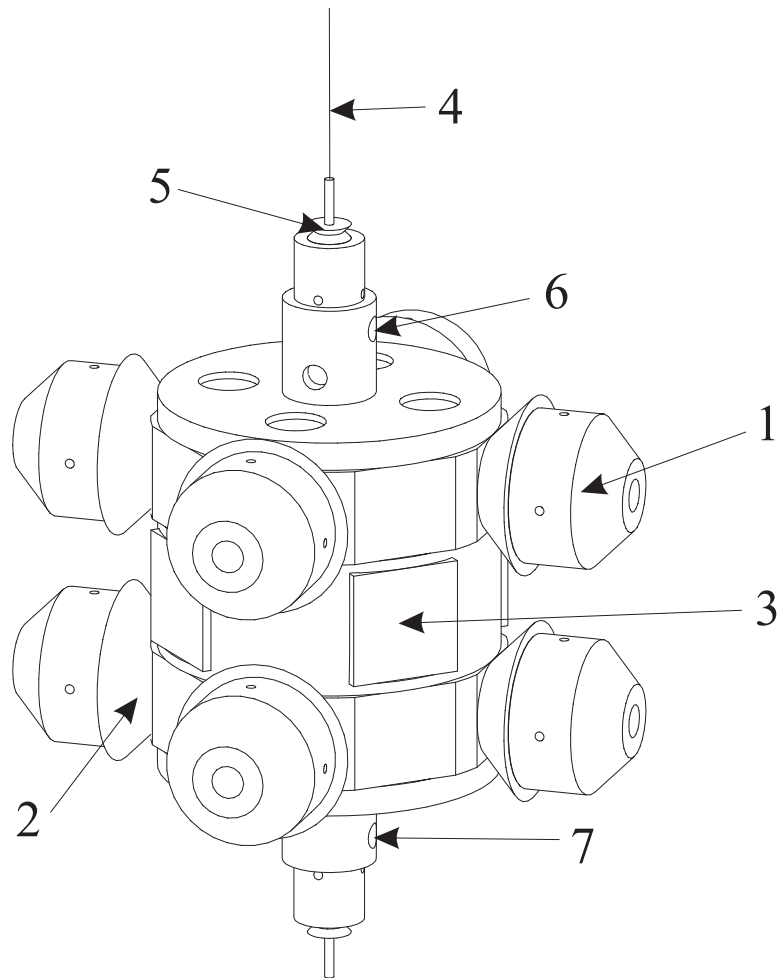


Figure 3.3: A 3 dimensional drawing of the Eöt-Wash III torsion pendulum. 1: test body, 2: test body holder, 3: mirror, 4: torsion fiber, 5: fiber screw, 6: upper tuning screw, 7: lower tuning screw.

to make the pendulum more rigid and to make the machining easier and more accurate. This part was made from two nearly identical parts and glued together with a tiny amount of vacuum compatible epoxy (Torr-Seal from Varian). Each part has a tuning ring, four holes for attaching the test body holders on the side of body, and four hidden screws to reduce the gravity gradient moments of the pendulum. There are eight conical test body holders and four mirrors fitted into machined recesses to the middle body with a small amount of Torr-Seal. On the top and the bottom of the pendulum are tapped holes in which small titanium screws are located. The screw position can be adjusted to reduce the gravity gradient moments of the pendulum due to machining imperfections. Two fiber screws were attached to the pendulum body. One is used to attach the fiber and the other is to maintain the symmetry of the pendulum. The fiber screws are made from copper. All the surfaces of the pendulum body were coated with a thin layer of gold.

### *3.2.2 Test Body*

Since the difference in the composition of the test bodies is the most important property to search for new interactions, the materials of the test bodies were chosen carefully to cover as broad a region of baryon number ( $B$ ) and lepton number ( $L$ ) as practical. We made test bodies out of beryllium, titanium and aluminum. Table 3.1 summarized the properties of the test bodies.

The test bodies have a barrel shape (Figure 3.4) that was designed to have vanishing mass moments up to  $l = 5$  (except for the  $q_{00}$ ). The test bodies are seated in the cone shaped test body holders and gold coated titanium screws were used to hold them into place. The barrel shape design of the test body and the cone shape design of the test body holder provided a reproducibility of test body placement on the holder to within  $5 \mu\text{m}$ . The test bodies are externally indistinguishable. The external shapes are identical and the external surfaces are coated with gold, however the titanium and aluminum test bodies had a hollow region (Figure 3.5) to account for the density difference of the materials. All test bodies have four pump out holes to prevent gas from being trapped inside the test bodies.

Table 3.1: The properties of the test bodies.

Quantity	Be	Ti	Al	Be - Ti	Be - Al
$B/\mu$	0.9986482	1.0010772	1.0006841	$-2.429 \times 10^{-3}$	$-2.036 \times 10^{-3}$
$L/\mu$	0.4438437	0.4594971	0.4818109	$-1.565 \times 10^{-2}$	$-3.797 \times 10^{-2}$
$f_s$	$-6.685 \times 10^{-3}$	$-9.113 \times 10^{-3}$	$-8.686 \times 10^{-3}$	$2.428 \times 10^{-3}$	$2.001 \times 10^{-3}$
$f_{EM}$	$4.949 \times 10^{-4}$	$2.054 \times 10^{-3}$	$1.490 \times 10^{-3}$	$-1.156 \times 10^{-3}$	$-9.954 \times 10^{-4}$
$f_w$	$3.013 \times 10^{-9}$	$3.156 \times 10^{-9}$	$3.151 \times 10^{-9}$	$-1.416 \times 10^{-10}$	$-1.362 \times 10^{-10}$

Here  $B/\mu$  and  $L/\mu$  are the charge to mass ratio.  $f_s$ ,  $f_{EM}$  and  $f_w$  are the fractional mass of the test bodies due to strong, electromagnetic and weak interaction, respectively[8].

The mass of each test body is  $4.84080 \pm 0.00005$  g. The height and the diameter of the barrel shaped test body are  $1.5885 \pm 0.0005$  cm and  $1.6865 \pm 0.0005$  cm, respectively.

### 3.3 Fiber Suspension System

This section describes the fiber suspension system which consisted of a torsion fiber, a magnetic damper, a heat shroud and a fiber positioner.

#### 3.3.1 Torsion Fiber

The torsion fiber is suspended from a magnetic damper and connected to a pre-hanger, which is a 2 cm long  $150 \mu\text{m}$  diameter gold coated tungsten fiber. The pre-hanger reduced the sensitivity to tilt. The torsional spring constant,  $\kappa$ , of the pre-hanger is large enough so that it does not participate in the torsional motion of the pendulum. One side of the pre-hanger is attached by a fiber screw to the magnetic damper. The other side is connected to the main torsion fiber by a copper clamping tube.

We used an 107.4 cm long  $20 \mu\text{m}$  diameter bare tungsten wire as the torsion fiber. The

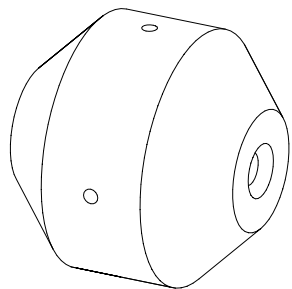


Figure 3.4: The barrel shape of a test body.

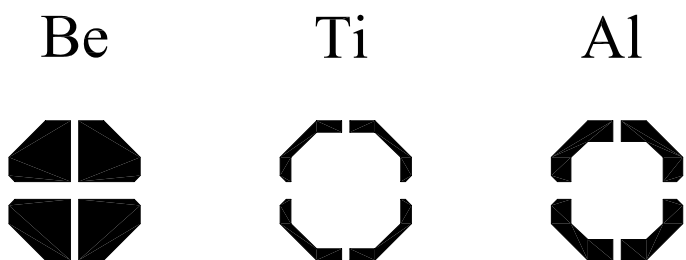


Figure 3.5: Cutaway side view of the testbodies.

fiber is crimped in a thin copper tube, which is glued into a "fiber screw". The fiber screw is attached to the top of the pendulum. The torsional spring constant,  $\kappa$ , of the fiber is  $0.0239 \pm 0.0002$  erg/rad, calculated using the free torsional oscillation period and the design moment of inertia of the pendulum.

### *3.3.2 Magnetic Damper*

A swing motion damper was necessary to reduce mechanical noise coupled into the torsion fiber. A magnetic eddy current damper was placed between the rotation shaft and the pre-hanger. Three soft beryllium copper leaf springs provided isolation from the vertical ground motion and the eddy current damper damped the vertical and pendulum motion without effecting the torsional motion. The magnetic damper is shown in Figure 3.6.

### *3.3.3 Heat Shroud*

Tungsten torsion fibers slowly unwind (drift) because they have a small helicity due to the manufacturing process. Thermal activation causes the equilibrium position of the fiber to change. The drift rate decreases slowly over the time but remains a strong function of temperature. Whenever the torsion fiber was not loaded by the pendulum mass, the drift rate returned to its initial rate of  $\geq 100 \mu\text{rad}/\text{hr}$ . To reduce the fiber drift rate, we heated the fiber using a massive polished copper tube (heat shroud), which surrounded the fiber along its entire length. To heat the shroud, we passed hot air ( $\sim 100^\circ\text{C}$ ) through a small tube attached to the shroud for 24 hours. Then, we ran the room temperature air through the shroud for 12 to 24 hours to cool the fiber to the operating temperature. This heat treatment typically took two or three days. Whenever the apparatus had been opened up to the air or the torsion fiber was not loaded, we had to perform the heat treatment. After the heat treatment, the drift rate was typically less than  $< 0.5 \mu\text{rad}/\text{hr}$ .

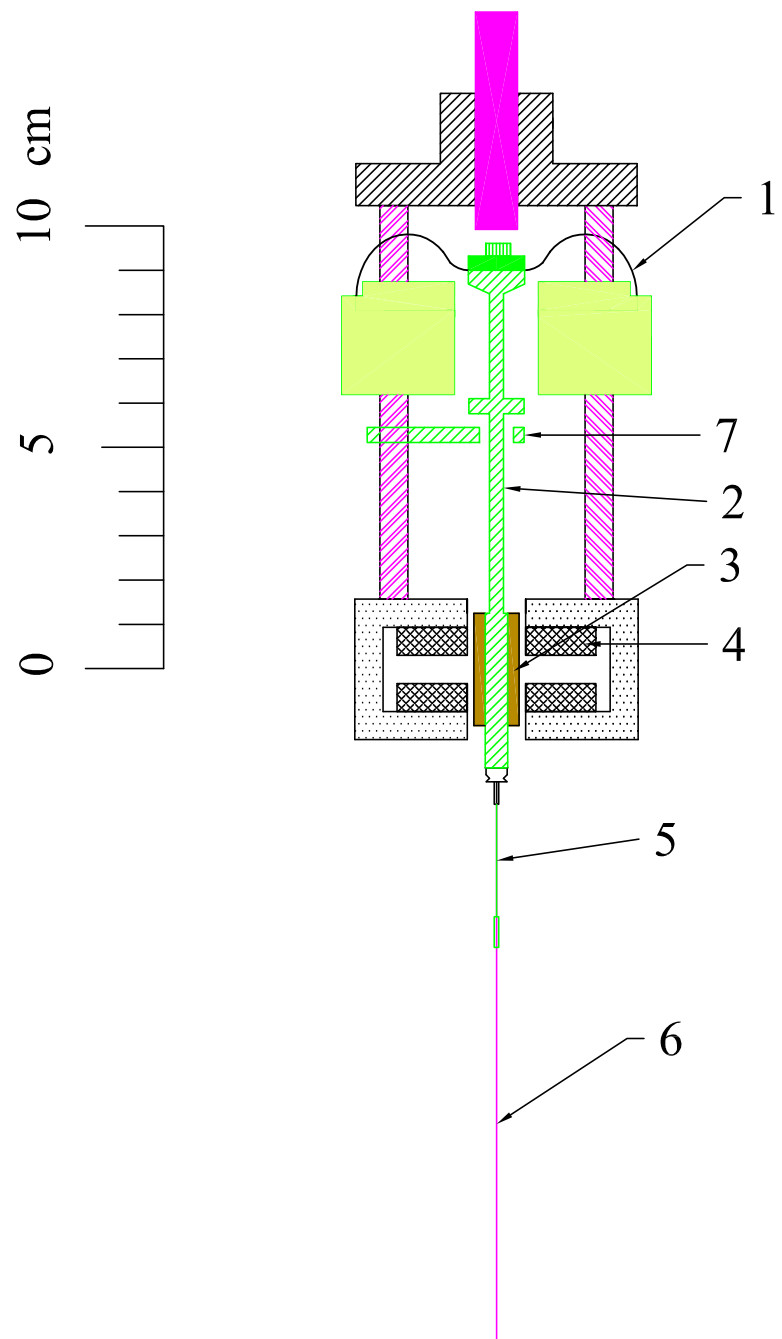


Figure 3.6: The schematic diagram of the magnetic damper. 1: beryllium copper leaf spring, 2: aluminum damper post, 3: copper slug, 4: magnet, 5: pre-hanger, 6: fiber, 7: stopper.

### 3.3.4 Fiber Positioner

The fiber positioner was located at the top of torsion balance, outside the vacuum vessel. It is used to adjust the lateral and vertical position of the torsion fiber and its rotational orientation. It connected to the magnetic damper with a bellows and an O-ring seal. The fiber positioner consisted of a X-Y translation stage, Z translation stage, and rotation stage connected to a shaft. The shaft connected to the magnetic damper. The electric controlled rotation stage (Newport Corporation, Model URM80APE) allowed us to rotate the pendulum and therefore the composition dipole direction and to align one of the pendulum mirrors with the autocollimator (see next section). The Z translation stage was used to change the vertical position of the pendulum by using an electric controlled micrometer (Newport Corporation, Model CMA25PP). The X-Y stage allowed us to adjust the horizontal position of the pendulum with two manual micrometers. The fiber positioner is shown in Figure 3.7.

## 3.4 Autocollimator

The angular deflection of the pendulum is measured with an autocollimator shown in Figure 3.8. A 50 mW, 785 nm laser diode (Mitsubishi ML64114R) located at focus of 30 cm lens produces a 5 mm diameter parallel beam. The diode laser light passes through an 1 mm diameter collimator, a polarizing beam splitter, a 1/4 wave plate, and an antireflective coated lens to enter the vacuum vessel. The beam reflects from a 45° mirror inside the vacuum and arrives at one of the pendulum mirrors. The light reflects off the pendulum mirror and goes into a corner cube mirror located below the 45° mirror. Finally, the light returns along the same path through the lens, the 1/4 wave plate and the polarizing beam splitter to the position sensitive detector located close to, but not at the focus of the lens. The beam size at this detector is 0.1 mm.

The position sensitive detector is a 3-terminal, analog resistive-division device. The resistance between the beam spot and the edges of detector is proportional to the distances between them. The ratio of the difference and sum of the currents in two terminals is interpreted as the position of the light beam. This normalization reduces any effects of

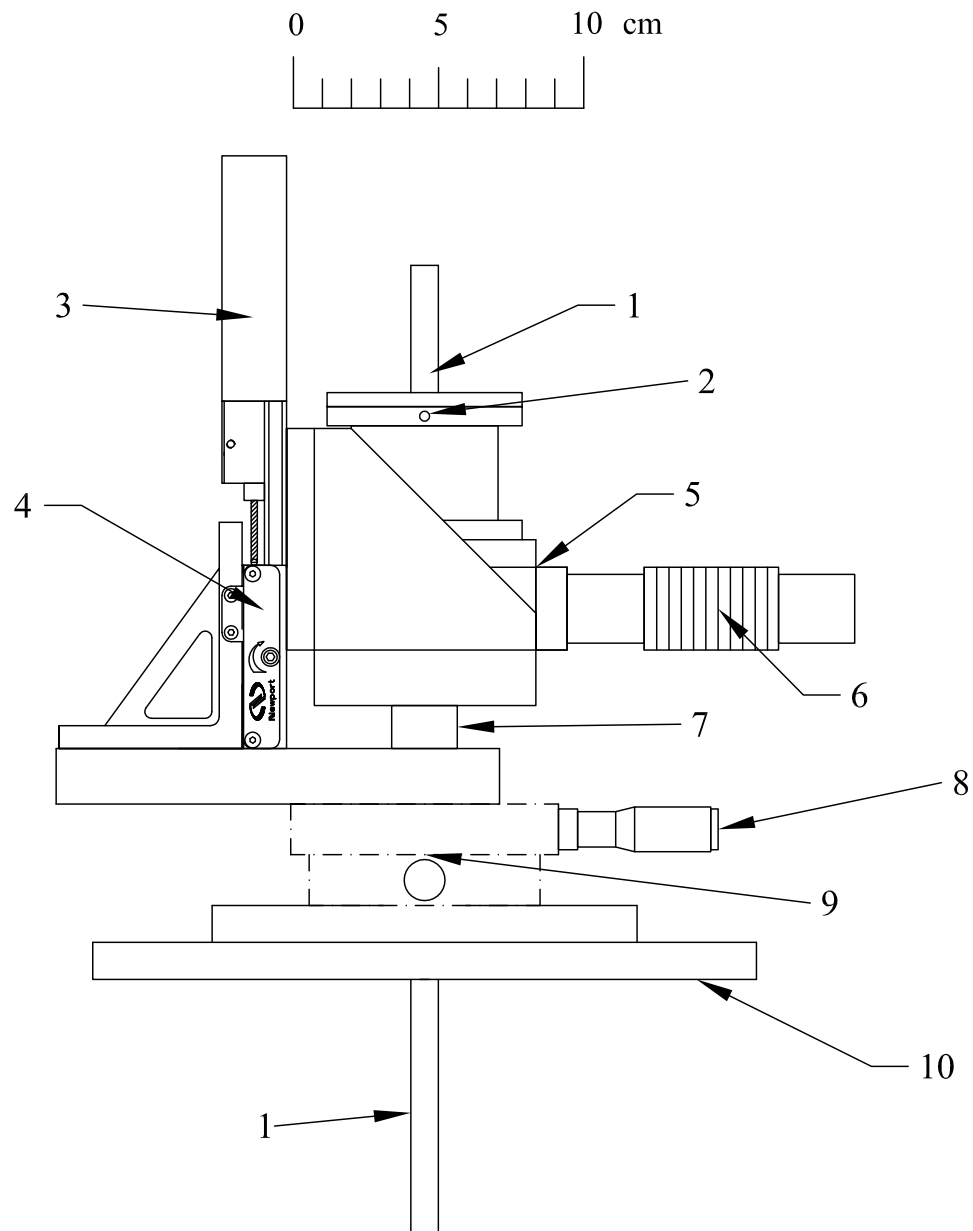


Figure 3.7: The schematic diagram of the fiber positioner. 1: shaft to magnetic damper, 2: tuning screw, 3: electric control micrometer, 4: Z stage, 5: rotation stage, 6: stepper motor, 7: inside below, 8: micrometer, 9: X-Y stage, 10: lid of vacuum vessel.

changes in the intensity of laser beam or the efficiency of the detector. A more detailed description can be found in section 3.4 of [17]. We use lock-in techniques to measure the difference and the sum currents. The intensity of laser beam is modulated with a TTL square wave at 142 Hz (Stanford Research System, Model DS430). The output signals of the position sensitive detector are passed through two lock-in amplifiers (Stanford Research System, Model SR830) synchronized with the TTL signal. The analog output of the lock-in amplifiers are digitized and recorded by the data taking computer.

### **3.5 Turntable**

We used an air bearing turntable (Professional Instruments Company, 10R Precision Turntable Model 9532) to rotate the entire vacuum vessel including the pendulum, the ion pump, the autocollimator, and several shields. The turntable was located above the apparatus and supported by a concrete base plate attached to the concrete beams that run between the cyclotron magnet and the wall of the cyclotron room(Figure 3.1). Figure 3.9 shows the details of the turntable.

The turntable was mounted on an aluminum support base plate to add heat capacity and mechanical stability. Three legs were attached to the aluminum plate. The legs consisted of bronze screws. Two of them were controlled by stepper motors to adjust the level of the turntable. The bronze screws sit on pillars of lead. Two of these were "active". We were able to change their height using thermal expansion. We measured the tilt of the turntable with two perpendicular rotational electric tilt sensors (Applied Geomechanics Inclinators: see section 3.7.1) which were located on the rotating platform near the fiber positioner and we minimize the tilt by using the two active thermal expansion feet (3.5.1). The resolved tilt of turntable is smaller than 3 nrad a day.

The angle of the turntable was measured by a centerless 36000 lines/rev optical encoder (Heidenhain Corporation, Model ER0725) which was directly mounted to the air bearing. The turntable is driven by a three-phase eddy current motor which was driven by three separate amplifiers driven by a three phase function generator. A digital signal processor

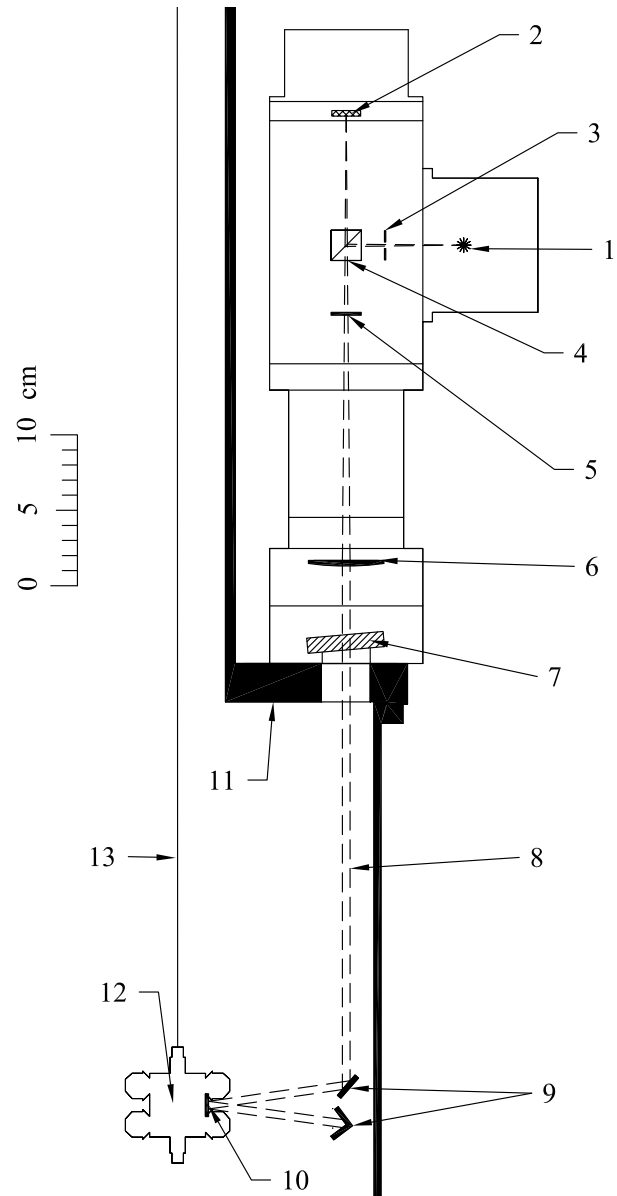


Figure 3.8: Schematic diagram of the autocollimator. 1: laser diode, 2: position sensitive detector, 3: collimator, 4: polarizing beam splitter, 5: 1/4 wave plate, 6: anti reflection coated lens, 7: antireflective window, 8: laser beam path, 9: reflectors, 10: pendulum mirror, 11: part of vacuum vessel, 12: pendulum, 13: torsion fiber.

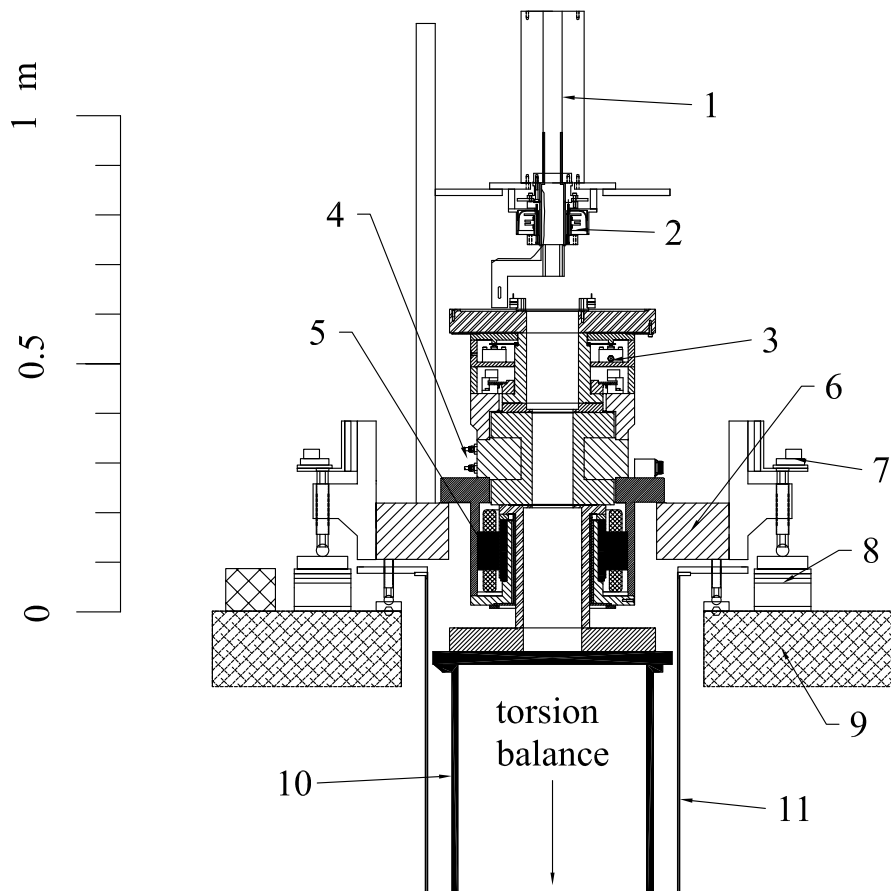


Figure 3.9: Schematic diagram of the turntable. 1: slip ring, 2: high voltage feedthrough for the ion pump, 3: optical angle encoder, 4: air bearing, 5: eddy current motor, 6: aluminum support base plate, 7: stepper motor, 8: active thermal expansion feet, 9: concrete bridge, 10: torsion balance holder, 11: thermal shield.

(DSP) was used to compute the feedback correction for the turntable rotation angle. The turntable rotation period was set to 1.5 times the free torsion period of the pendulum, about 20 minutes.

### *3.5.1 Active Thermal Extension Feet*

Our turntable rested on three feet. Two of them were active, which can change their height using temperature dependent expansion to compensate for the laboratory tilt. The feet were designed in 2001 by Ulrich Schmidt. Figure 3.10 shows cross section of the one foot. The expanding and shrinking components of one foot consisted of two lead rings which were soldered to a copper disk. Thermal energy could be pumped into or out of the copper disk by a peltier element, which was also thermally coupled to a brass block. The brass block was held at constant temperature by circulating water from a constant-temperature bath (Naslab Model RTE-221) through it. Two G10 rings thermally isolated the lead rings from the laboratory floor and a stainless steel disk on top, which the turntable rested on. The peltier element and the brass block were clamped to the copper disk by one bolt. Specially formed G10 pieces provide thermal isolation between the bolt, the copper disk and the brass block.

We measured the tilt with two perpendicular rotational electric tilt sensors (AGIs). The AGIs were mounted on the rotating top of the apparatus near the fiber positioner. The analog signals of the AGIs were digitized by the data acquisition system.

Due to the heat capacity and the heat resistance of the copper disk and the lead rings, the response of the expansion of the lead rings to a change in the heatflux provide by the peltier element is delayed by 6.7 seconds. Also the heat conductivity of the peltier element, which tends to bring back the temperature of the copper disk to the temperature of the constant-temperature bath, has to be taken into account. Therefore we need a model, which predicts the response of a foot to a change in heat input to the peltier element. Figure 3.11 shows the model used for calculating the response and the simplified flow chart of the feedback loop of the active thermal feet.

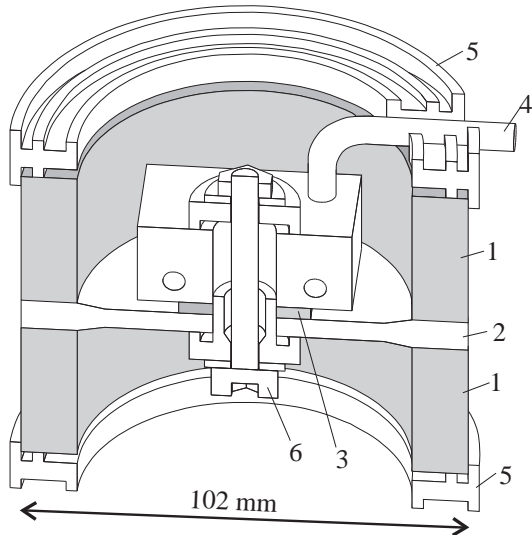


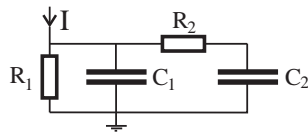
Figure 3.10: Cross section of the active thermal expansion foot. 1: lead ring, 2: copper disk, 3: peltier element and brass block, 4: connected to a constant-temperature bath, 5: G10 ring, 6: holding bolt.

### 3.6 Gradiometer Pendulum and Gravity Gradient Compensators

Figure 3.12 shows a gradiometer pendulum we developed to measure the strength of the  $Q_{21}$  and  $Q_{31}$  gravity gradient fields at the location of the pendulum. The gradiometer pendulum consists of four equally spaced aluminum disks that have chamfered holes to seat titanium balls. By changing the position of 16 titanium balls, we were able to separately create large  $q_{21}$  and  $q_{31}$  moments with magnitudes of  $35.78 \text{ gcm}^2$  and  $105.22 \text{ gcm}^3$ , respectively. In both of the two formations the moment of interest was maximized, while the other moments vanished by design. Thus we can measure each of the  $Q_{21}$  and  $Q_{31}$  ambient gravity gradient fields independently.

We used massive gravity gradient compensators to compensate the gravity gradients at the location of the pendulum. Figure 3.13 shows our  $Q_{21}$ ,  $Q_{22}$  and  $Q_{31}$  compensators. The  $Q_{21}$  compensator consisted of 48 trapezoid lead blocks divided into two half-annuli. One was placed above and one below the pendulum position, both carefully centered with

simple thermal model



I : heat flux peltier element  
 C<sub>1</sub>: heat capacity copper disk  
 C<sub>2</sub>: heat capacity lead rings  
 R<sub>1</sub>: heat resistance peltier element  
 R<sub>2</sub>: heat resistance copper disk

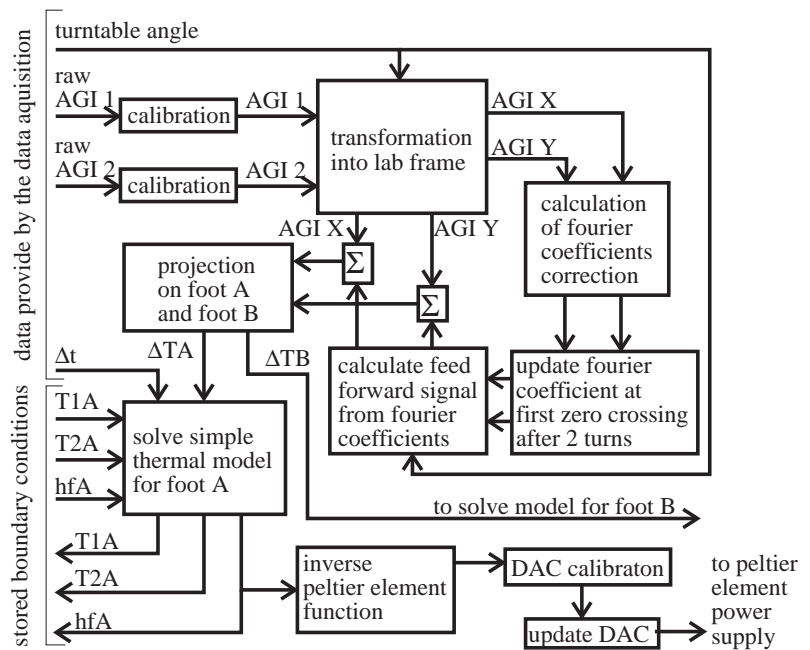


Figure 3.11: Thermal model and flow chart of the simplified feed back loop for active thermal feet.

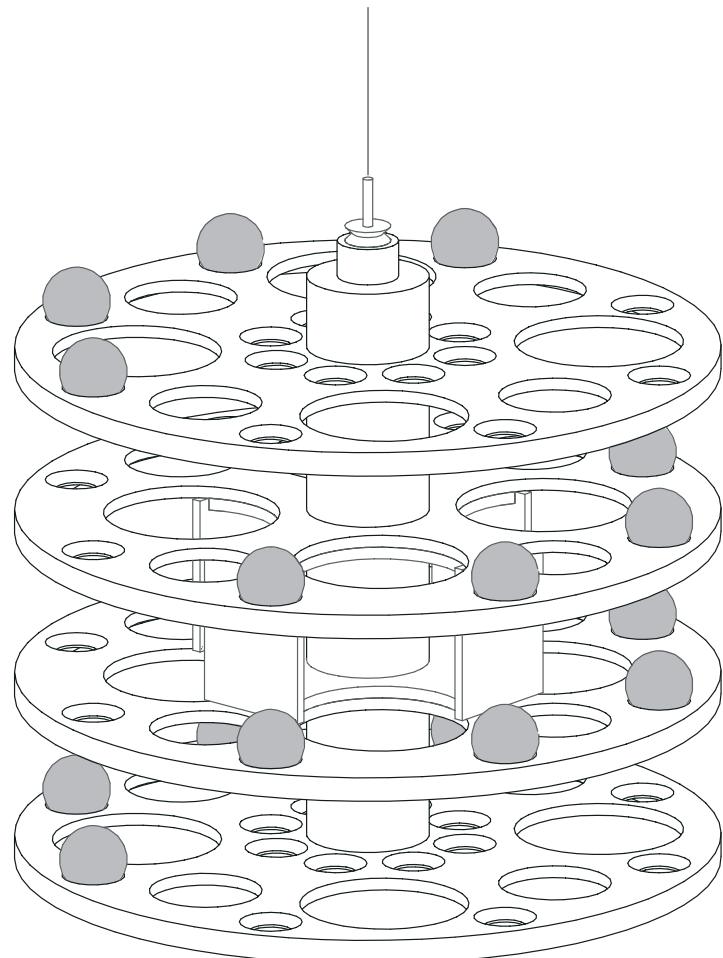


Figure 3.12: Gradiometer pendulum. Shown is the  $q_{31}$ -configuration to measure the  $Q_{31}$  gravity gradient.

respect to the turntable rotation axis. The total mass of the  $Q_{21}$  compensator was 878.7 kg. The  $Q_{22}$  compensator was constructed from 8 lead bricks. Four lead bricks cover  $90^\circ$  in azimuth and all lead bricks were symmetrical about the midplane. The  $Q_{31}$  compensator consisted of 24 aluminum blocks and four lead bars, arranged in a semicircle, roughly at the midplane. The total mass of the  $Q_{22}$  and  $Q_{31}$  compensators were 200.1 kg and 5.5 kg, respectively. Each of compensators was mounted on three different aluminum supporting plates, with which we were able to independently rotate the phase of the gravity gradient fields. All the compensators were supported by an aluminum structure (for more detailed discussion about gravity gradient fields see Chapter 5).

### **3.7 Environmental Monitors**

#### *3.7.1 Tilt*

We used three pairs of orthogonal electronic tilt sensors (Applied Geomechanics Instruments, Model 755). One pair of tilt sensors was mounted on the non-rotating aluminum supporting plate of the turntable and another two pairs of tilt sensors were installed close to the rotation axis at the top and bottom of the vacuum vessel. One pair (top AGI) is located at 170 cm above the pendulum and its signal is used as the reference signal for our active thermal expansion feet leveling system. The other pair (bottom AGI) is located at 23 cm below the pendulum. We used this sensor to infer the direction of local vertical near the pendulum position. The signal from the rotating tilt sensors was used to determine systematic effects (Chapter 5). The typical calibration was  $100 \mu\text{rad}/\text{V}$ .

#### *3.7.2 Linear Position*

Two linear position sensors (Linear Variable Differential Transformer) were installed near two active thermal expansion feet to measure the expansion of the leveling feet and calibrate them.

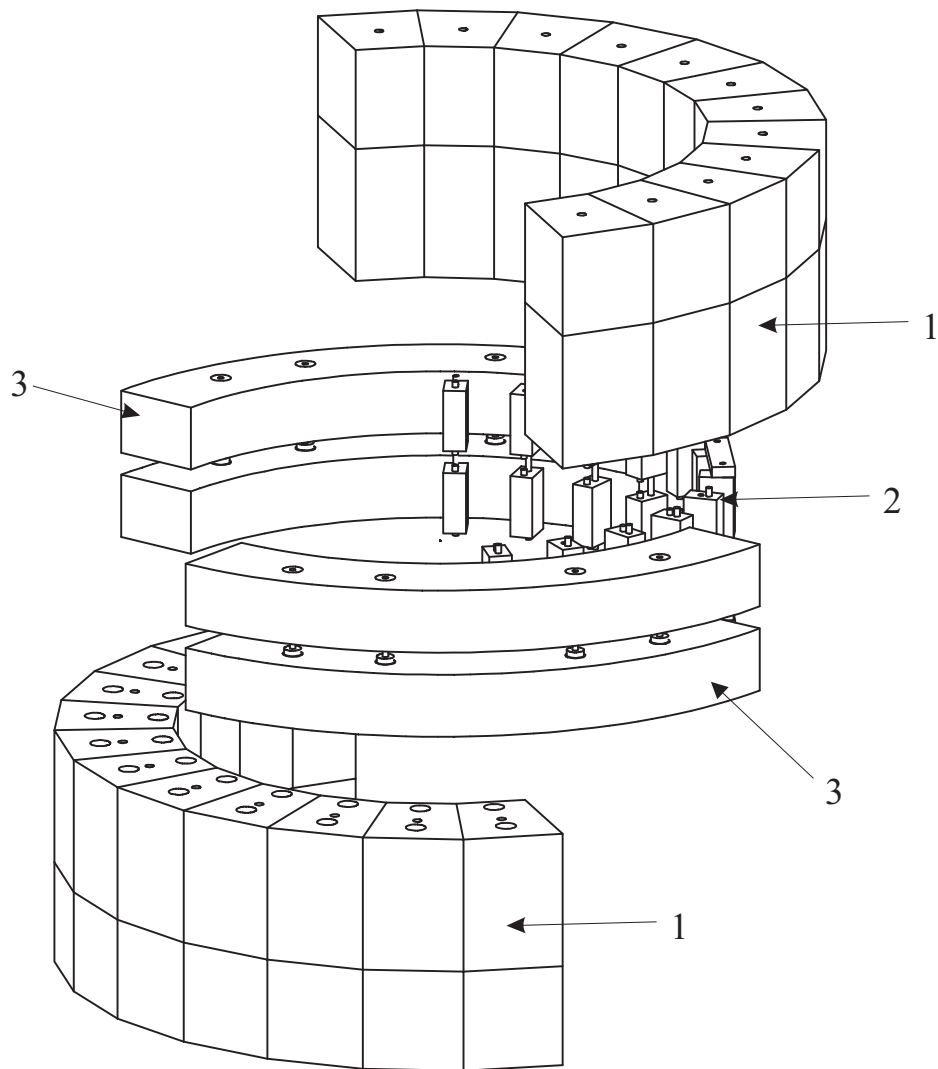


Figure 3.13: A 3 dimensional drawing of all gravity gradient compensators. 1:  $Q_{21}$  compensator, 2:  $Q_{31}$  compensator,  $Q_{22}$  compensator.

### 3.7.3 Temperature

We used solid state current devices (Analog Devices, Model AD590) to measure the temperature of the instrument. The sensors produce currents which are proportional to the absolute temperature at a rate of  $1 \mu\text{A}/\text{K}^\circ$ . The currents were converted to voltage and recorded by the data taking computer. We recorded the temperature at 15 places. Table 3.2 summarizes the location of the temperature sensors.

Table 3.2: The location of the temperature sensors.

Temperature sensor	Location
t1	lower outer thermal shield
t2	middle outer thermal shield
t3	upper outer thermal shield
t4	upper Naslab bath
t5	air of the turntable house
t6	air near the top AGI
t7	air near the autocollimator
t8	middle of column of vacuum vessel 1
t9	near the fiber positioner
t10	middle of column of vacuum vessel 2
t11	concrete exterior wall of the cyclotron room
t12	south side radiator
t13	north side radiator
t14	wall toward the center of the cyclotron room
t15	cyclotron room temperature

### **3.8 Shielding**

#### *3.8.1 Magnetic Shielding*

Four layers of the mu-metal magnetic shielding were installed around the torsion pendulum. One layer is stationary and three rotate with the turntable. The stationary magnetic shield is attached to a thermal shield around the balance. Two of the rotating magnetic shields are located inside the vacuum chamber and surround the torsion pendulum. One rotating shield was installed outside the vacuum chamber. All of the magnetic shields were degaussed and together reduced the magnetic field variations at the pendulum position by a factor of better than  $10^4$ . We have measured a reduction in magnetic field variations with a flux gate magnetometer.

#### *3.8.2 Thermal Shielding*

The copper heat shroud around the torsion fiber inside the vacuum vessel was used to isolate the fiber from outside temperature variations (described earlier, section 3.3.3). Two layers of passive thermal shields were installed around the vacuum vessel. One rotates with the turntable and surrounds the vacuum vessel. The other is a stationary shield, which covers all of the apparatus except for the turntable. We observed the temperature variation at the vacuum vessel with in  $\pm 0.01$  °C. The complete apparatus is insulated from the cyclotron room by an enclosure made from Styrofoam and plywood. The temperature inside this housing was controlled using a constant-temperature bath (Neslab Model RTE-221) that circulated water through two automobile radiators. The temperature variation inside the hosing was measured with  $\pm 0.5$  °C. The cyclotron room temperature was kept constant within  $\pm 1$  °C by a non cycling air temperature controller. The detail discussion of the temperature variation effect see the section 5.4.

## Chapter 4

# CALIBRATION AND DATA ANALYSIS

### **4.1 Calibration Constants**

Electronic signals from the turntable angle encoder, the autocollimator, two pairs of the rotating electronic tilt sensors, one pair of the stationary tilt sensors, 2 linear position sensors, 15 temperature sensors, and the ion pump current were recorded to a raw data file in raw ADU unit (bits) with a sampling time of 2.74 s. The sampling time was selected to have 72 data points for each free torsional period of the pendulum. The raw ADU values of the sensors were calibrated to real physical units. The angular deflection of the pendulum was proportional to the ratio of the difference ( $\Delta$ ) and sum ( $\Sigma$ ) of the currents from the ends of the position sensitive detector in the autocollimator. A nonlinear calibration of this ratio to angular deflection was used:

$$\theta = c_0 + c_1 \frac{\Delta}{\Sigma} + c_2 \left( \frac{\Delta}{\Sigma} \right)^2, \quad (4.1)$$

where  $c_i$  are calibration constants. The physical values of other sensors are proportional to the raw ADU values.

$$S_i \text{ (in physical unit)} = c_0 + c_1 S_i \text{ (in ADU)} + c_2 S_i^2 \text{ (in ADU)} \quad (4.2)$$

The calibration constants of each sensor were stored in a header file. In the next paragraphs a brief description of the calibration procedure is given.

### **4.2 Calibration of the Angular Deflection**

The most important calibration was the angular deflection of pendulum and the torsion constant ( $\kappa$ ) of the fiber. We used a "dynamic calibration" method to calibrate the angular deflection of the pendulum. The amplitude of the pendulum was excited by abruptly

changing the turntable rotation rate by a known amount ( $\Delta\omega$ ). We fitted the data with the equation of a damped harmonic oscillator from which we determined the amplitude, the free torsion period ( $T_0$ ) and the damping time ( $\tau$ ).

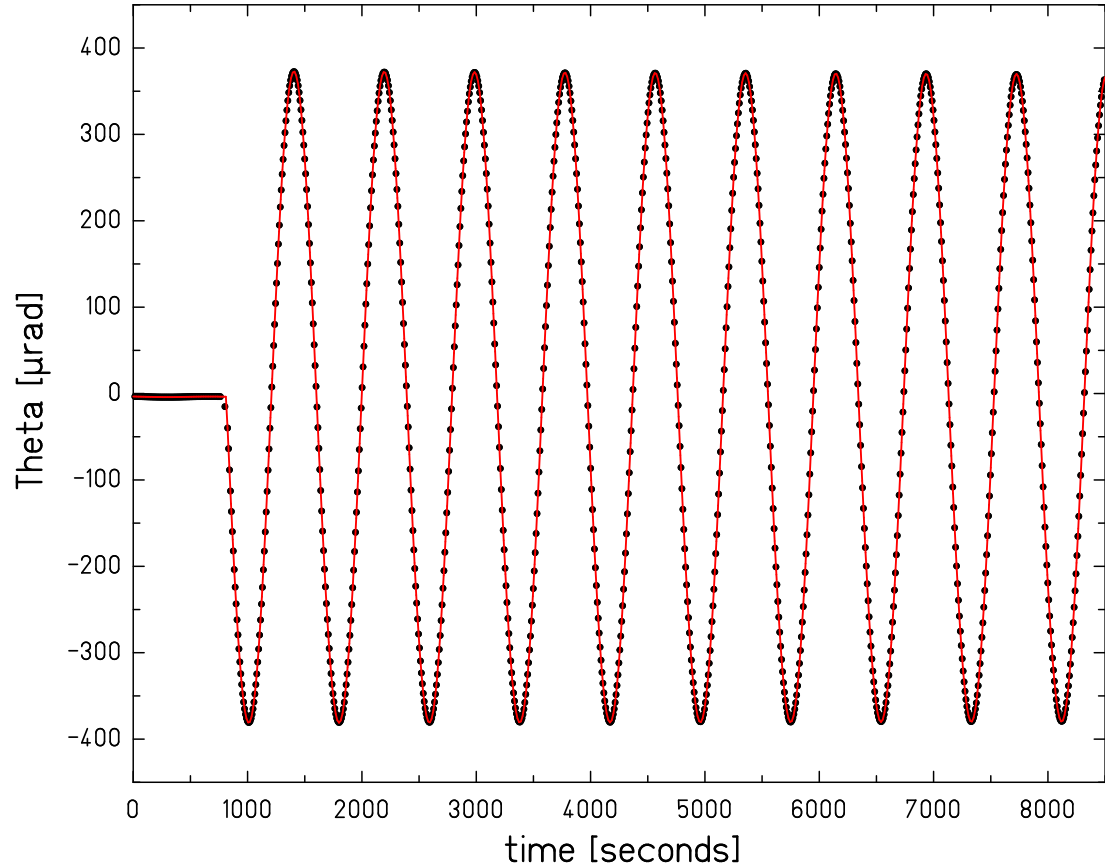


Figure 4.1: Dynamic calibration: at  $t = 800$  seconds the turntable rotation rate was changed from  $0 \mu\text{rad/s}$  to  $3 \mu\text{rad/s}$ .

Figure 4.1 shows a typical dynamic calibration run. The turntable rotation rate was changed by  $3 \mu\text{rad/s}$  at  $t = 800$  s. The line is the best fit. The dots are the data. From the fitting results we determined  $T_0$  and  $\tau$  which were  $(789.917 \pm 0.003)$  s and  $(1.160 \pm$

$0.004) \times 10^6$  s, respectively. The fiber restoring constant,  $\kappa$ , was determined to be  $(0.0239 \pm 0.0002)$  erg/rad using the calculated moment inertia of the pendulum  $I = 377.22$  g/cm<sup>2</sup>

$$\kappa = I \omega_0^2 = I \left(\frac{2\pi}{T_0}\right)^2. \quad (4.3)$$

Table 4.1 shows the summary of some calibration runs.

Table 4.1: The summary of the calibration runs.

Run number	date	$T_0$ (s)	Q	$\kappa$ (erg/rad)
run1510	06/28/04	789.972(2)	$4160 \pm 60$	0.0239(2)
run1544	07/24/04	790.009(7)	$4000 \pm 250$	0.0239(2)
run1747	02/02/05	789.996(2)	$5200 \pm 100$	0.0239(2)
run1809	03/18/05	789.917(3)	$4610 \pm 170$	0.0239(2)
run1890	05/17/05	789.829(3)	$3720 \pm 90$	0.0239(2)
run2026	09/07/05	789.992(3)	$5470 \pm 220$	0.0239(2)
run2093 <sup>†</sup>	10/22/05	795.296(9)	$3148 \pm 250$	0.0235(2)
run2100 <sup>†</sup>	10/30/05	795.065(3)	$8034 \pm 400$	0.0236(2)
run2106 <sup>†</sup>	11/01/05	795.073(3)	$6932 \pm 300$	0.0236(2)
run2206 <sup>†</sup>	12/20/05	795.070(3)	$5105 \pm 200$	0.0236(2)

<sup>†</sup> These runs used a new fiber.

### 4.3 Data Taking Procedures

During Equivalence Principle data taking, we reversed the orientation of the pendulum and hence the orientation of the composition dipole with respect to the vacuum vessel every day. A data set lasted usually 14 days. In the next cycle, we changed the orientation of the pendulum by 90° and took the data again while reversing the dipole direction daily. Then we repeated the two cycles, after which we conducted systematic tests. The systematic tests

are explained in Chapter 5. After the systematic tests, we reversed the dipole configuration by interchanging the test bodies on the pendulum body and repeated the data taking cycle.

#### 4.4 Data Reduction

##### 4.4.1 Raw Data

Figure 4.2 shows a typical raw data segment of  $\Delta$  and  $\Sigma$  of the autocollimator.

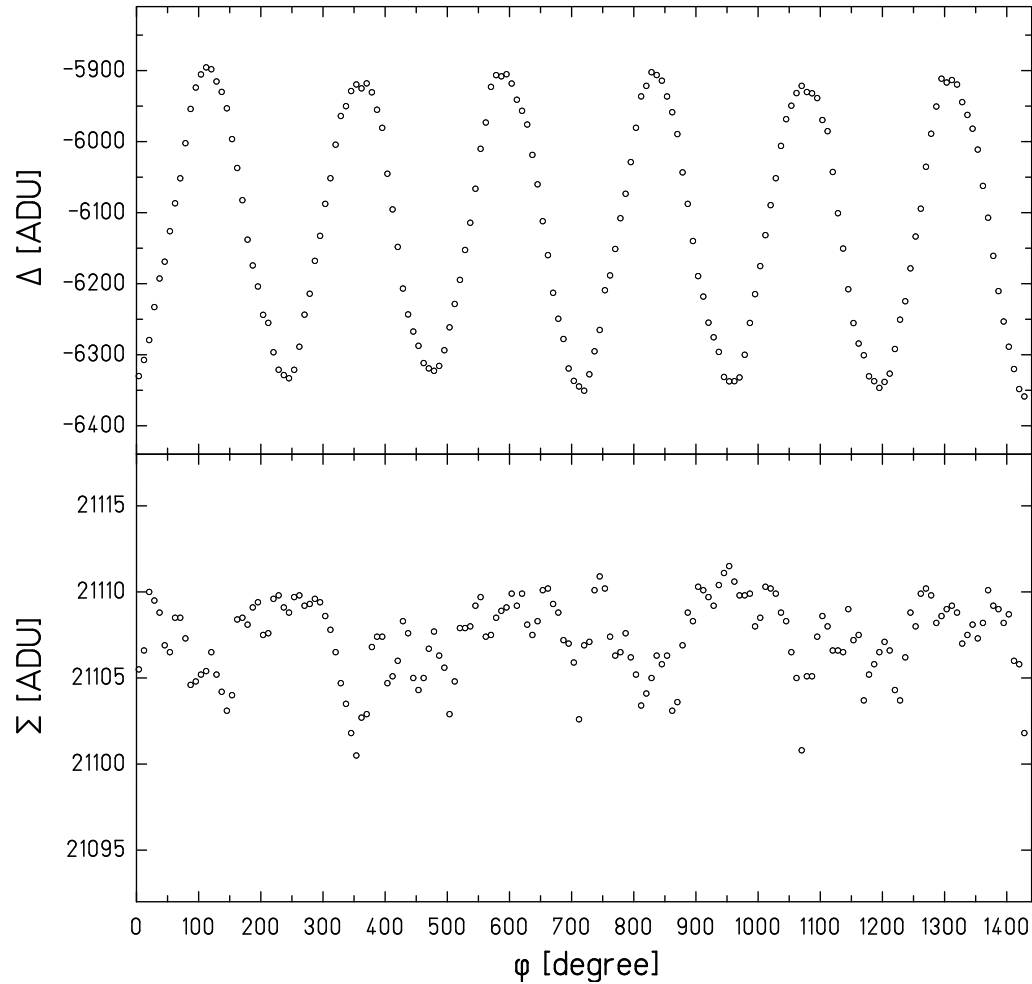


Figure 4.2: An example of the raw data. Top panel shows the autocollimator  $\Delta$  signal and the bottom panel shows a  $\Sigma$  signal.

#### 4.4.2 Filtering

As can be seen in Figure 4.2, the raw signal was usually dominated by the free torsional oscillation of the pendulum. Since the free torsional signal does not affect an Equivalence Principle violation signal, we used a digital filter, called "torsion filter", to remove the free torsional signal. The torsion filter averaged two data points that were a half a torsional period apart.

$$\theta_{filtered}(t) = \frac{1}{2} [\theta_{raw}(t - \frac{T_0}{4}) + \theta_{raw}(t + \frac{T_0}{4})] \quad (4.4)$$

$$= \frac{1}{2} [\theta_{raw}(t - \frac{\pi}{2\omega_0}) + \theta_{raw}(t + \frac{\pi}{2\omega_0})] \quad (4.5)$$

The top panel of Figure 4.3 shows the deflection angle of the pendulum with the torsional mode and the middle panel shows the results of the effect the torsion filter on this data. After applying the torsion filter, we binned the data in 5.48 s bins to reduce the computational effort.

#### 4.4.3 Cutting and Fitting of Data

We divided the filtered and averaged data into subsections which contained 4 revolutions of the turntable (about 80 minutes), i.e. six free torsional cycles, and 1728 data points. The subsections, called 'cuts', were fitted as a function of the angle of the turntable  $\phi$  with 9 harmonics terms and 3 drift terms (in total 21 parameters) :

$$\theta_{fit}(\phi) = \sum_{n=1}^9 [a_n^s \sin(-n\phi) + a_n^c \cos(-n\phi)] + \sum_{m=0}^2 c_m P_m \quad (4.6)$$

where  $P_m$  are the Legendre polynomials to account for fiber drift. Figure 4.3 shows filtered and averaged data with the corresponding fit and the residuals for one data cut.

#### 4.4.4 Elimination of Bad Data

We computed the fit quality parameter  $\chi^2$  to quantify how well the fit function described the data. Based on the  $\chi^2$  for each cut, we decided whether an individual cut would

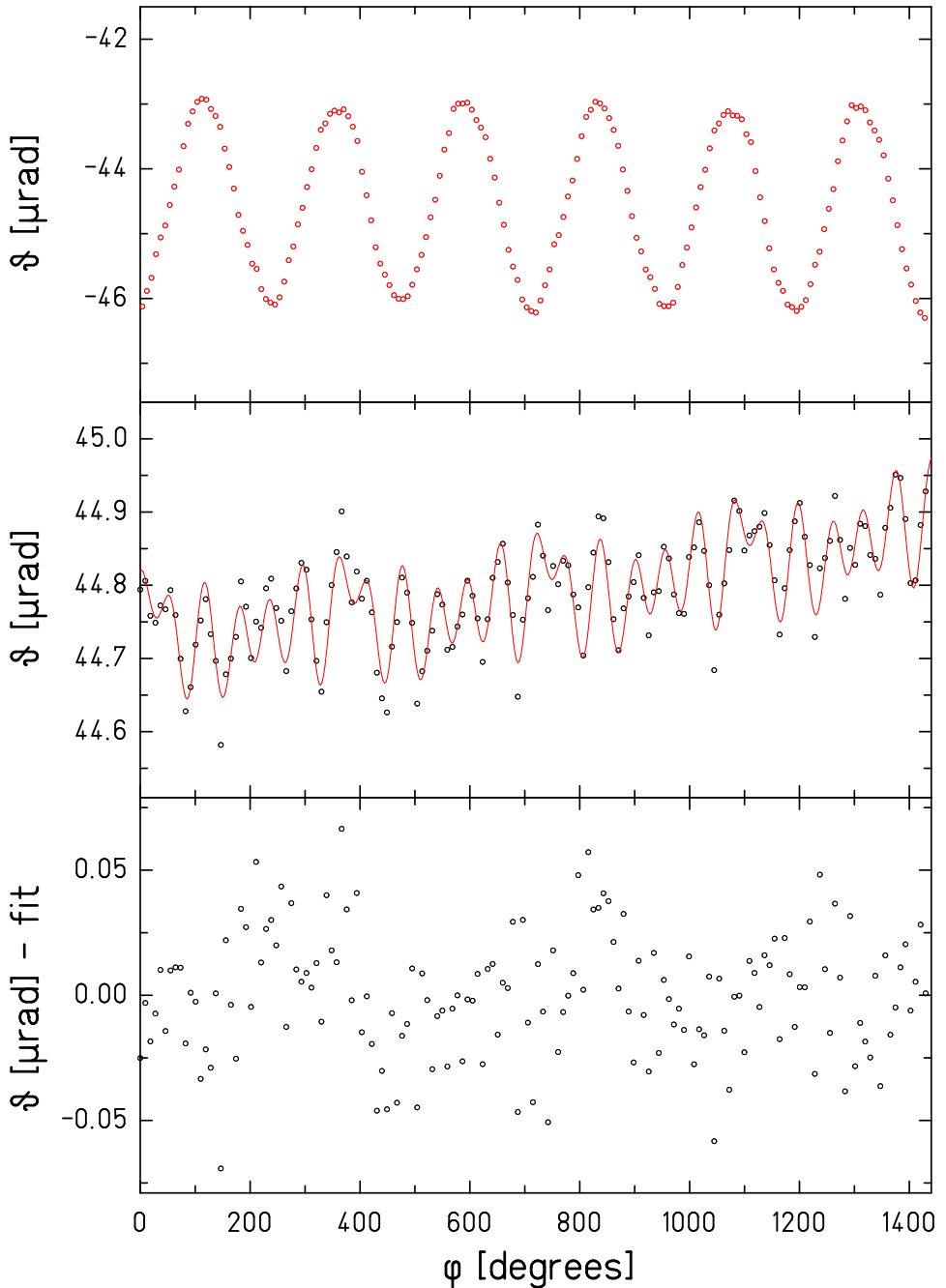


Figure 4.3: Data reduction and fits. Shown is a 4 revolution cut. The top panel displays the calibrated deflection angle of the pendulum. The middle panel shows the torsion filtered data and the best fit, shown as a solid line. The bottom panel shows the fit residuals.

be excluded from the data analysis. In addition, we checked for abnormal values in the monitoring sensors. Cuts with large value of the  $\chi^2$  and unusual signals in the monitoring sensors were rejected. The main sources of the bad cuts were ion pump pressure release spikes, a spontaneous jump in the signal caused by spurious untwisting of the torsion fiber (fiber quakes) and seismic activity. Figure 4.4 shows an example of the bad data caused by an earthquake. For a typical data taking period of one day consisting of 19 cuts,  $\approx 2$  cuts were rejected.

#### 4.4.5 Combining the Data

We recorded about 19 cuts with each day of data taking. After rejecting bad cuts, each good cut contributed equally to the mean. The uncertainty of one data set is described by the variance:

$$\sigma_{a_n} = \left[ \frac{1}{N(N-1)} \sum_{i=1}^N (a_{n i} - \bar{a}_n)^2 \right]^{1/2}, \quad (4.7)$$

where  $n$  denotes the harmonics of the fitting term,  $N$  is the number of data cuts,  $\bar{a}_n$  is the mean value, and  $\sigma_{a_n}$  is the uncertainty of the  $\bar{a}_n$ . Figure 4.5 shows the  $1\omega$  coefficients for a typical one-day data set.

#### 4.4.6 Attenuation Correction

Due to the pendulum inertia, filtering and averaging processes, the fitted amplitudes of data were attenuated and shifted in phase. We had to correct for these effects to get the true value of the torque and the true phase of the signal.

##### Pendulum Inertia

We can rewrite Equation 2.15 for the motion of an inertia-less pendulum( $\theta = \frac{T_0}{\kappa}$ ) with an attenuation factor  $A_n^p$  and a phase shift  $\Phi_n^p$ ,

$$\theta(t) = \sum_{n=1}^9 (A_n^p \left[ \frac{T_{0n}}{\kappa} \sin(n\omega t + \Phi_n^p) \right]), \quad (4.8)$$

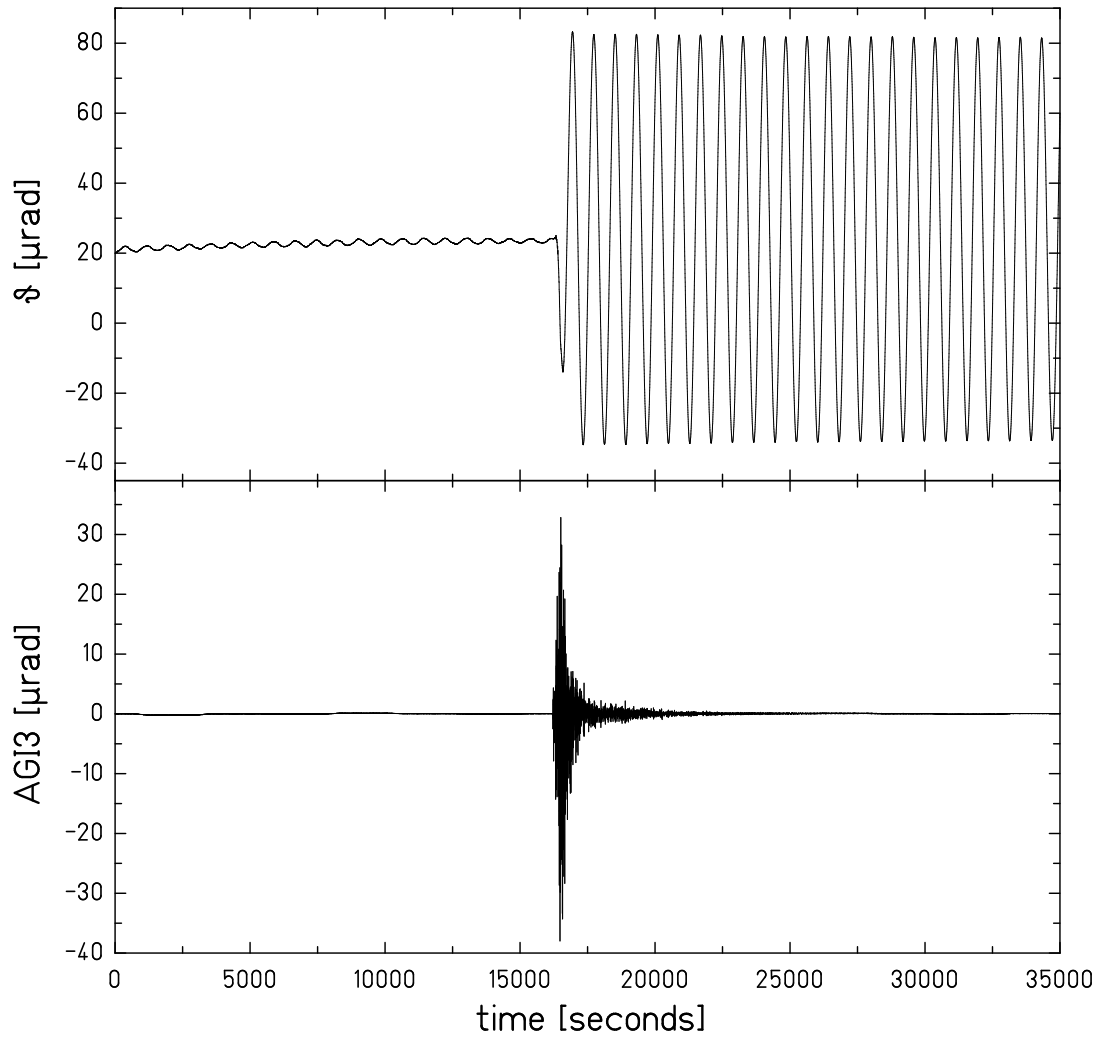


Figure 4.4: The data recorded during an earthquake at the coast of northern California : June 14, 2005. The top panel displays the pendulum deflection angle and the bottom shows the signal of one of the tilt sensors.

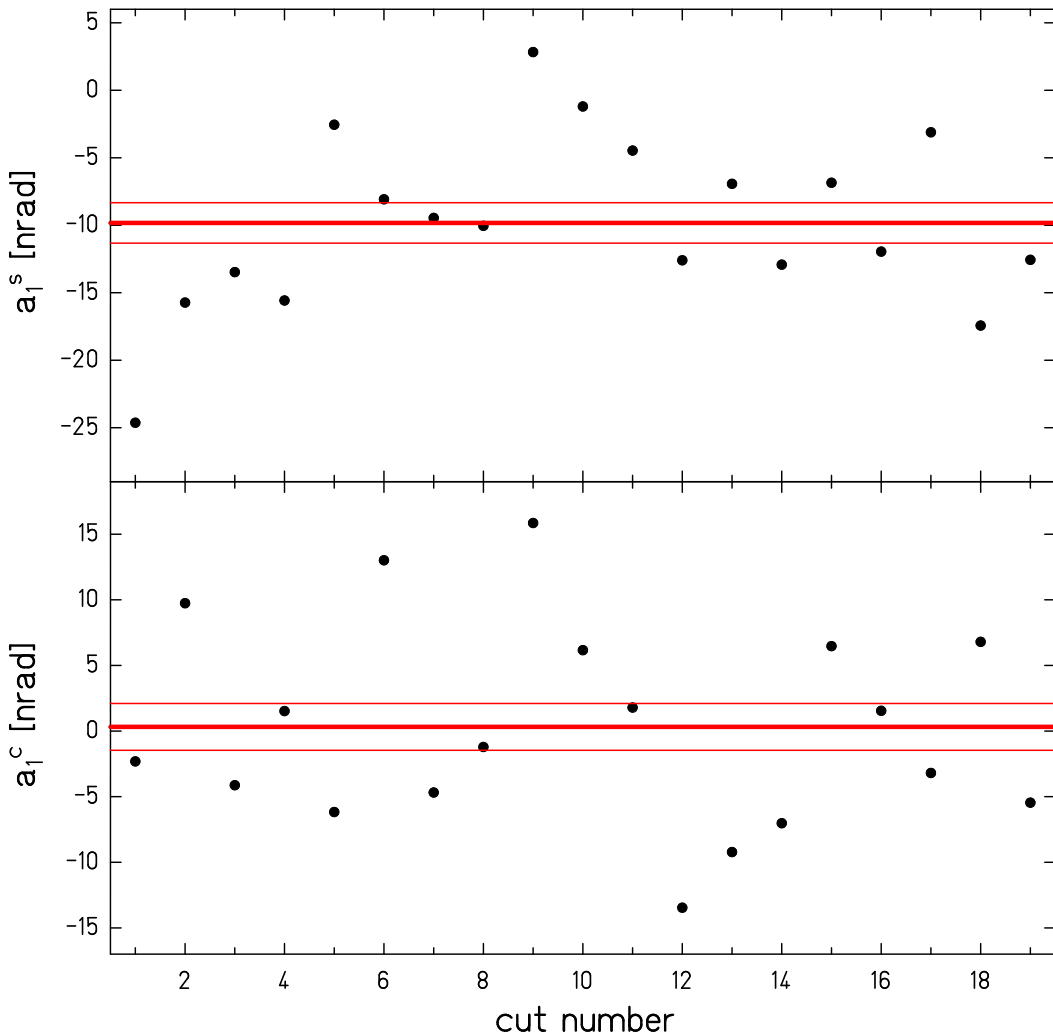


Figure 4.5:  $a_1^s$  and  $a_1^c$  coefficients indicate accelerations along the North-South component and the West-East component of the  $1\omega$  signal, respectively. The points are the coefficients of the individual cuts. The thick solid line indicates the mean value and thin lines show the uncertainty limits of the mean value.

where

$$A_n^p = \left[ \left( 1 - \frac{n^2 \omega^2}{\omega_0^2} \right)^2 + \left( \epsilon + \frac{2n\gamma\omega}{\omega_0^2} \right)^2 \right]^{-\frac{1}{2}} \quad (4.9)$$

$$\Phi_n^p = \tan^{-1} \left( \frac{-2n\gamma\omega - \epsilon\omega_0^2}{\omega_0^2 - n\omega^2} \right). \quad (4.10)$$

### *Torsion Filter*

The application of the torsion filter described in section 4.4.2, also attenuated the signal.

Consider a harmonic oscillator with an amplitude  $A$ , a period  $T = 2\pi/\omega$  and a phase  $\phi$ ,

$$\theta_{raw}(t) = A \sin(n\omega t + \phi) \quad (4.11)$$

then we can rewrite Equation 4.5 to

$$\theta_{filtered}(t) = \frac{1}{2} A \left[ \sin \left( n\omega t + \phi - \frac{n\pi\omega}{2\omega_0} \right) + \sin \left( n\omega t + \phi + \frac{n\pi\omega}{2\omega_0} \right) \right] \quad (4.12)$$

$$= A \cos \left( \frac{n\pi\omega}{2\omega_0} \right) \sin(n\omega t + \phi). \quad (4.13)$$

Thus, the torsion filter reduces the amplitude by

$$A_n^f = \cos \left( \frac{n\pi\omega}{2\omega_0} \right) \quad (4.14)$$

and there is no phase shift ( $\Phi_n^f = 0$ ).

### *Lock-in-Amplifier*

The 2 pole low pass filter with the characteristic time ( $t_c$ ) on the  $\Delta$  and  $\Sigma$  lock-in amplifier signals attenuated and phase shifted the signals by:

$$A_n^L = \frac{1}{1 + (n\omega t_c)^2} \quad (4.15)$$

$$\Phi_n^L = -2 \tan^{-1}(n\omega t_c). \quad (4.16)$$

### Averaging Process

The data averaging process also attenuated the true amplitudes. Let us consider averaging  $2m+1$  data points with a data interval  $\Delta$  over an averaging time  $t_{ave}$  for a sinusoidal signal,

$$\theta_{raw}(t) = A \sin(n\omega t) \quad (4.17)$$

Then the average data is

$$\theta_{ave}(t) = \frac{1}{2m+1} \sum_{k=-m}^m A \sin[n\omega(t+k\Delta)] \quad (4.18)$$

$$= \frac{1}{2m+1} \frac{\sin[(m+\frac{1}{2})n\omega\Delta]}{\sin(n\omega\Delta/2)} \theta_{raw}(t). \quad (4.19)$$

If we rewrite Equation 4.19 with  $N = 2m + 1$  and  $t_{ave} = N\Delta$ , then the attenuation factor is

$$\frac{\theta_{ave}(t)}{\theta_{raw}(t)} = \frac{1}{N} \frac{\sin(n\omega t_{ave}/2)}{\sin(n\omega t_{ave}/2N)} \quad (4.20)$$

and there is no phase shift. We used two averaging processes. One was done during the data taking and the other was done during the data analysis. The data acquisition system took the  $N$  samples, averaged them into a data point, which was recorded. The attenuation factor was:

$$A_n^{ave1} = \frac{1}{N} \frac{\sin(n\omega t_{sample}/2)}{\sin(n\omega t_{sample}/2N)} \quad (4.21)$$

When analyzing data, we averaged the  $m = t_{ave}/t_{sample}$  of data over  $t_{ave}$ . Yielding an attenuation factor:

$$A_n^{ave2} = \frac{1}{m} \frac{\sin(n\omega t_{ave}/2)}{\sin(n\omega t_{ave}/2m)} \quad (4.22)$$

$$= \frac{t_{sample}}{t_{ave}} \frac{\sin(n\omega t_{ave}/2)}{\sin(n\omega t_{sample}/2)} \quad (4.23)$$

The total attenuation factor due to averaging is

$$A_n^{ave} = A_n^{ave1} \times A_n^{ave2} \quad (4.24)$$

The corrected amplitude and phase from the attenuation are

$$\theta_{corrected}(n\omega) = \frac{\theta_{fitted}(n\omega)}{A_n^L \times A_n^L \times A_n^f \times A_n^{ave}} \quad (4.25)$$

$$n\phi_{corrected}(n\omega) = n\phi_{fitted}(n\omega) + \Phi^p + \Phi^L \quad (4.26)$$

Table 4.2 summarizes the attenuation factors and phase shifts for  $N = 46$ ,  $t_{sampling} = 2.74$  s and  $t_{ave} = 5.48$  s.

Table 4.2: The summary of the attenuation factors and phase shifts.

n	Pendulum <sup>†</sup>		Lock-In		Average + Filter		Total	
	$A_n^p$	$\Phi_n^p(^{\circ})$	$A_n^L$	$\Phi_n^L(^{\circ})$	$A_n^{f+ave}$	$\Phi_n^{f+ave}(^{\circ})$	$A_n^{tot}$	$\Phi_n^{tot}(^{\circ})$
1	1.80000	0.0	.99975	-1.8	.49999	0.0	.89975	-1.85
2	1.28572	-90.0	.99899	-1.8	-.49995	0.0	.64214	-1.81
3	.33333	-60.0	.99773	-1.8	-.99976	0.0	.33250	-1.82
4	.16364	-45.0	.99597	-1.8	-.49979	0.0	.08145	-1.82
5	.09890	-36.0	.99371	-1.8	.49967	0.0	.04911	-37.82
6	.06667	-30.0	.99097	-1.8	.99905	0.0	.06600	-31.82
7	.04813	-25.7	.98775	-1.8	.49935	0.0	.02374	-27.53
8	.03644	-22.5	.98406	-1.8	-.49915	0.0	.01790	-1.81
9	.02857	-20.0	.97991	-1.8	-.99786	0.0	.02794	-1.81

<sup>†</sup> The attenuation factors of the pendulum only applied to the deflection angle of the pendulum.

#### 4.4.7 Combining Different Dipole Direction Data

Since we took data by reversing the direction of the pendulum, we were able to separate the signal into a component that follows the composition dipole (e.g. Equivalence Principle violating signal) and a component that does not. Figure 4.6 shows the  $1\omega$  coefficients of a typical data set with the pendulum orientation changed daily. Half of the difference of  $1\omega$  signals from the two consecutive data runs contains an Equivalence Principle violating signal. Half of the sum of  $1\omega$  signals of the two consecutive data runs is due to systematic

effects such as turntable speed variations. We called these signals "offsets". Figure 4.7 and Figure 4.8 show the North-South and West-East components of the  $1\omega$  signal and the offset signal.

#### 4.5 Analyzing Data toward Astronomical Sources

Our North-South component ( $a_1^s$ ) and West-East component ( $a_1^c$ ) of the signal could contain an Equivalence Principle violating signal due to astronomical sources. This signal should result in a solar or sidereal day variation of the  $a_1^s$  and  $a_1^c$  coefficients. To extract the differential acceleration signal toward the astronomical sources, a set of the  $a_1^s$  and  $a_1^c$  coefficients from each data taking cycle was fitted by

$$a_1^s = k \cos \theta [-\cos(\phi - \phi_0) \Delta a - \sin(\phi - \phi_0) \Delta a^*] + d^s, \quad (4.27)$$

$$a_1^c = k \cos \theta [+ \sin(\phi - \phi_0) \Delta a - \cos(\phi - \phi_0) \Delta a^*] + d^c. \quad (4.28)$$

Here  $k = 1.56 \times 10^3$  rad s<sup>2</sup>/cm is a property of our torsion pendulum,  $\Delta a$  is the differential acceleration toward the astronomical sources,  $\Delta a^*$  is a quadrature acceleration that is expected to vanish within the error of the measurement, and  $\phi_0$  specifies the orientation of the composition dipole when  $\phi=0$ . The constants  $d^s$  and  $d^c$  account for effects fixed in the lab frame. The altitude of the astronomical source,  $\theta$ , and the azimuth,  $\phi$ , were computed at the midpoint of each data taking cycle and taken to be constant during that data taking cycle. Figure 4.9 shows the result of 6 months data analyzed toward the Sun. Figure 4.10 shows the result of 6 months data analyzed toward the galactic center.

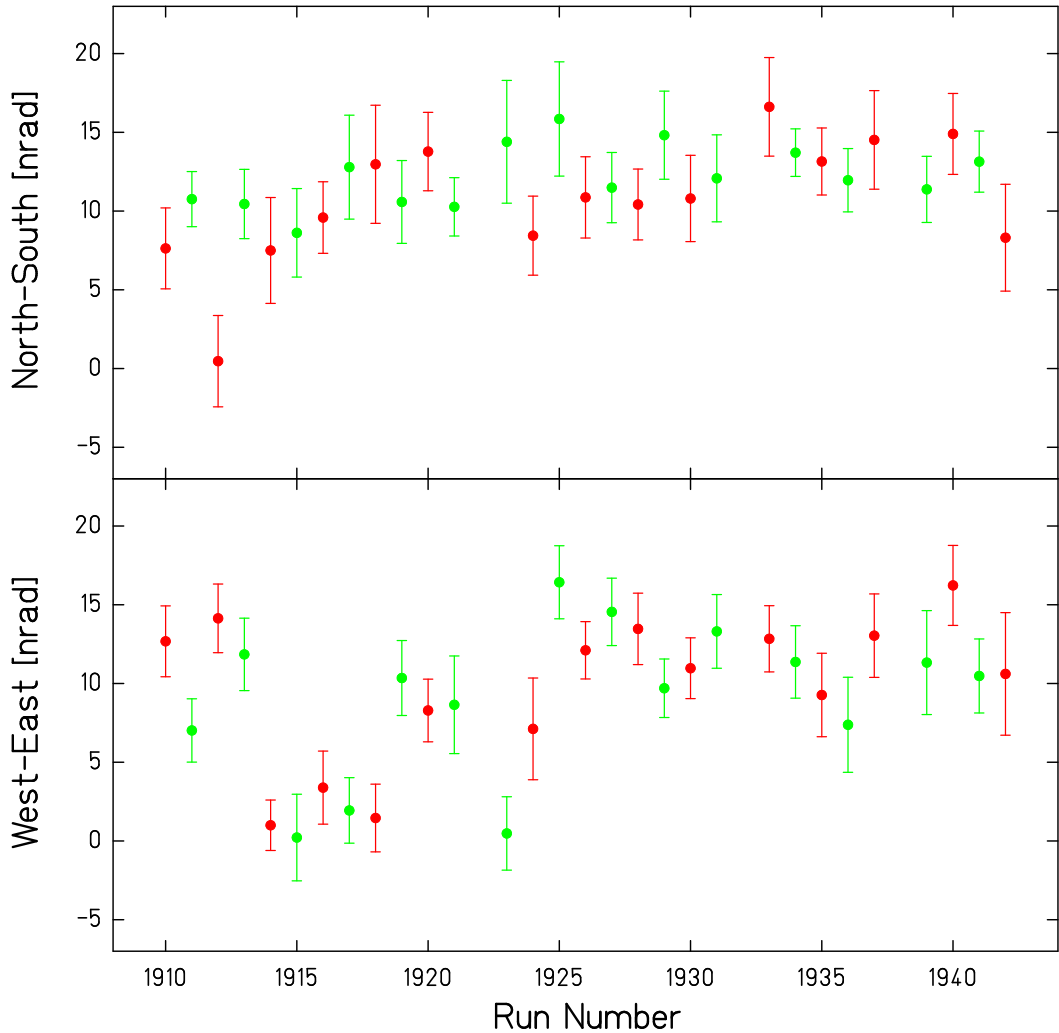


Figure 4.6: A typical data set taken with two different pendulum orientations, i.e. composition dipole orientations. Each vertical bar indicates the result of one day of measurement. The data points shown in dark were taken with the composition dipole pointing toward the autocollimator, called  $0^\circ$ . The data points shown in light were taken with the composition dipole pointing toward the opposite direction, called  $180^\circ$ .

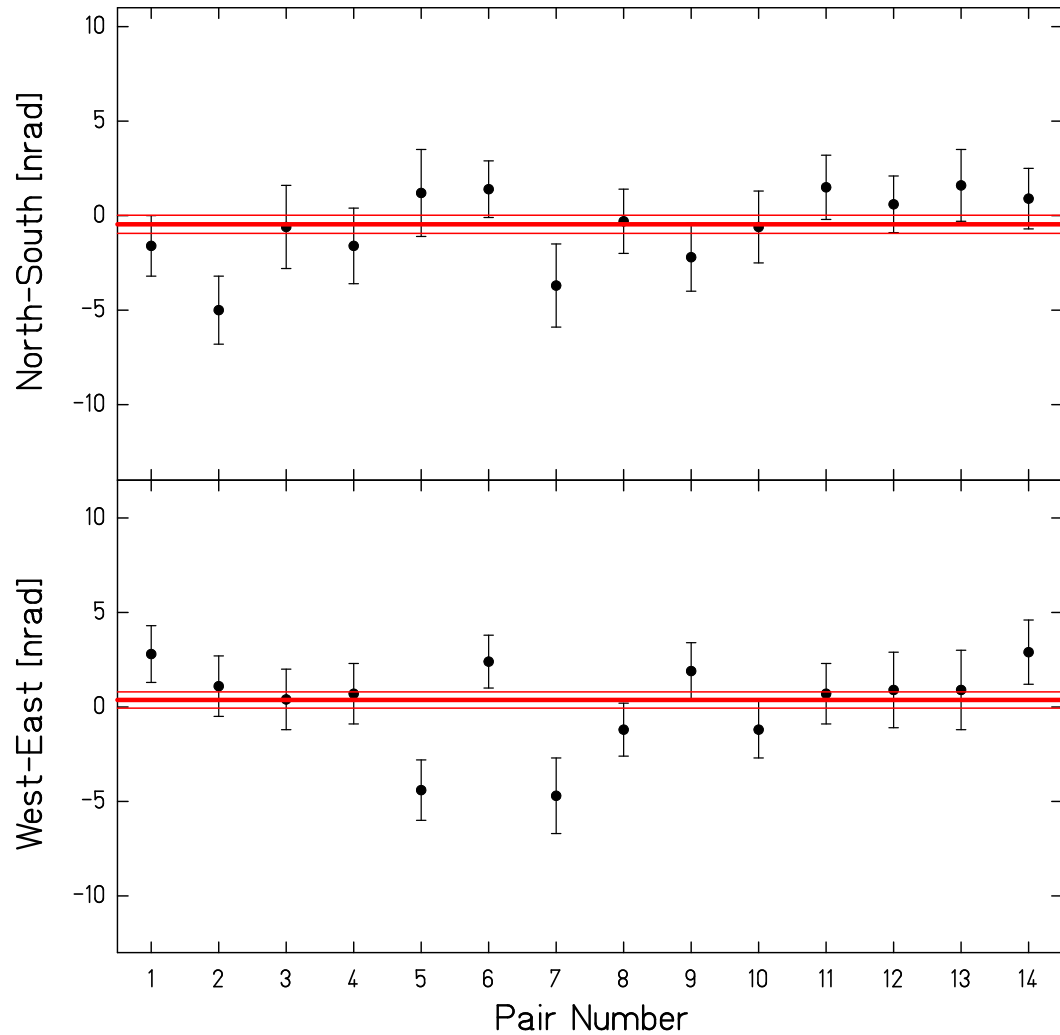


Figure 4.7: The  $1\omega$  signal which tracks the composition dipole. The lines reflect the average signal with a  $1\sigma$  error band.

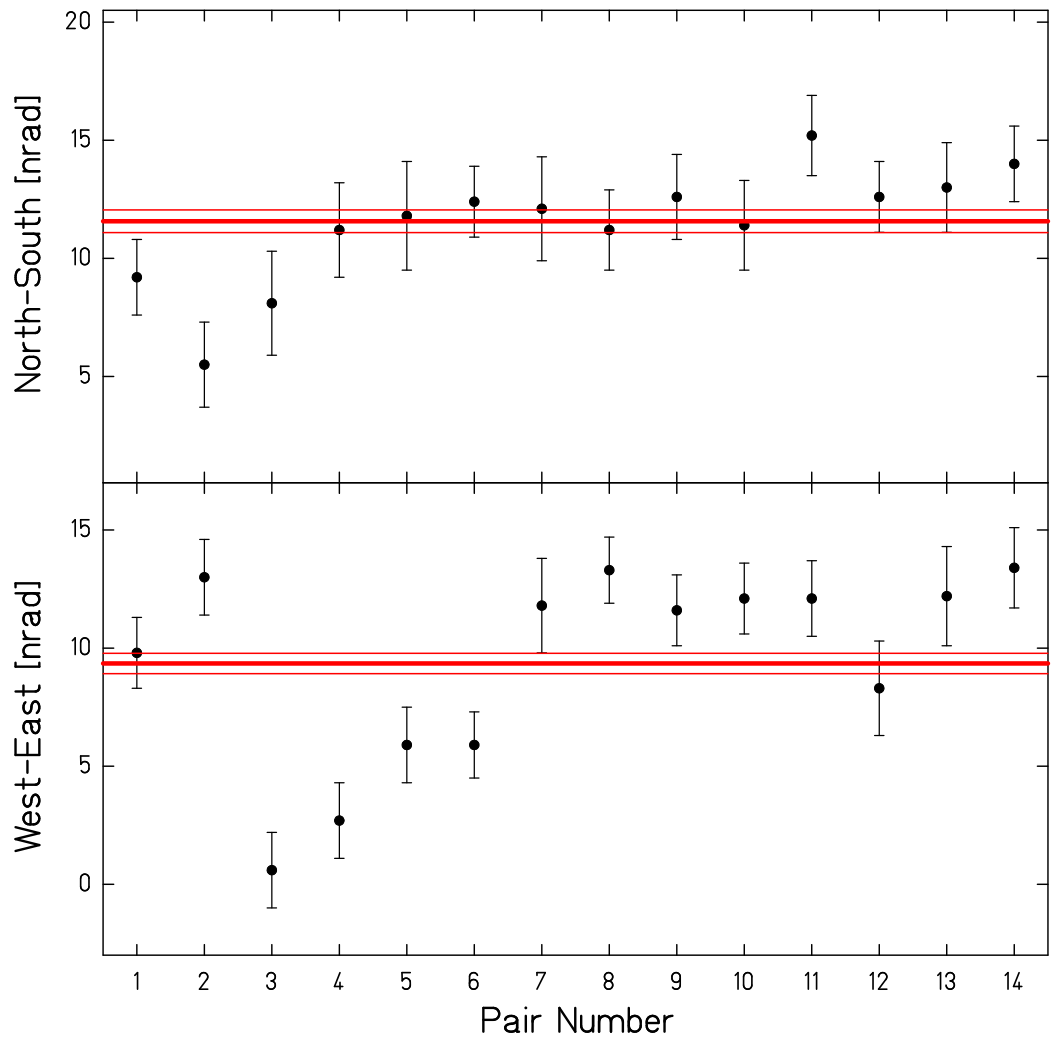


Figure 4.8:  $1\omega$  offset signals as defined in the text. The lines reflect the average signal with a  $1\sigma$  error band.

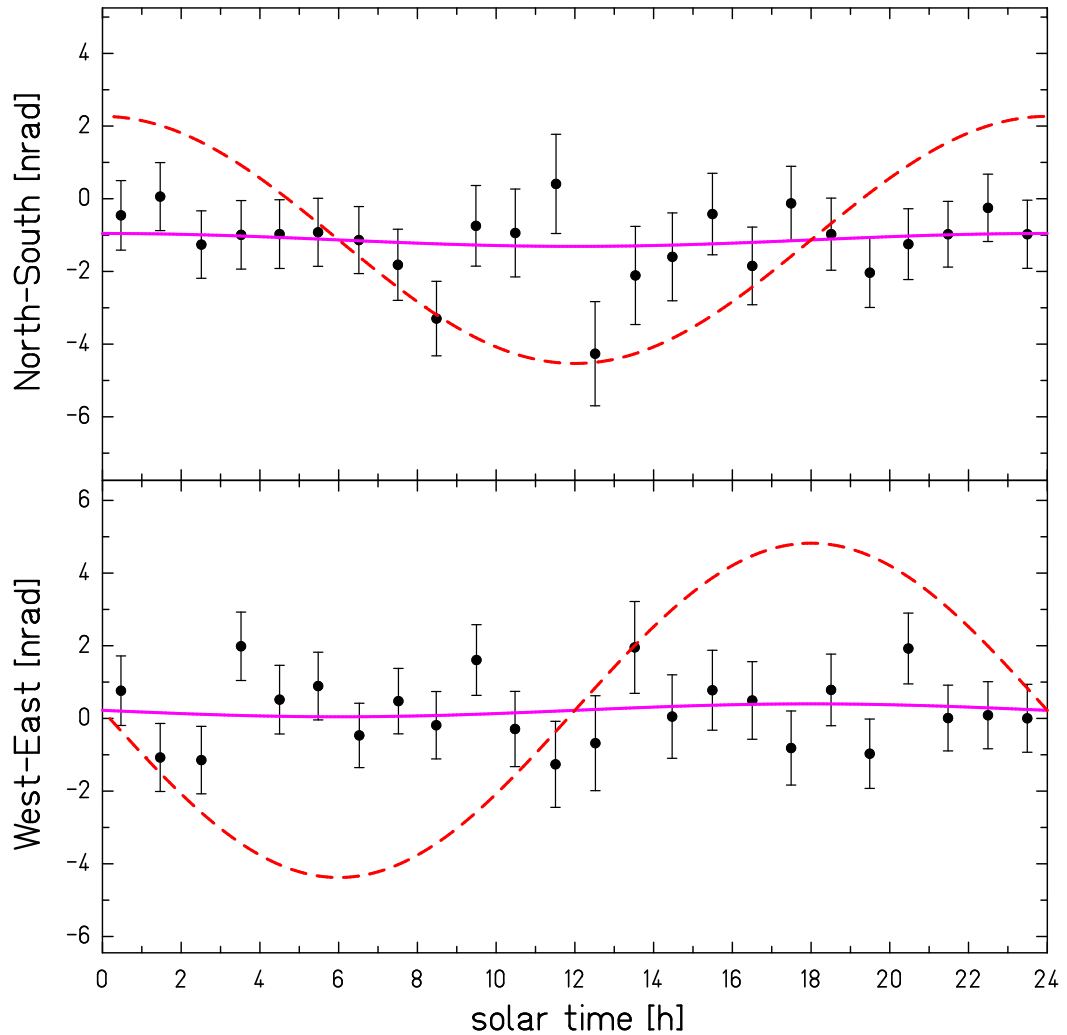


Figure 4.9: Cumulative results toward the Sun for North-South and West-East components of the signal histogrammed as a function of the solar time of day. The solid curves show the mean result of fitting the individual data cycles. The dashed curves show a hypothetical signal for  $\Delta a = 3 \times 10^{-12} \text{ cm/s}^2$

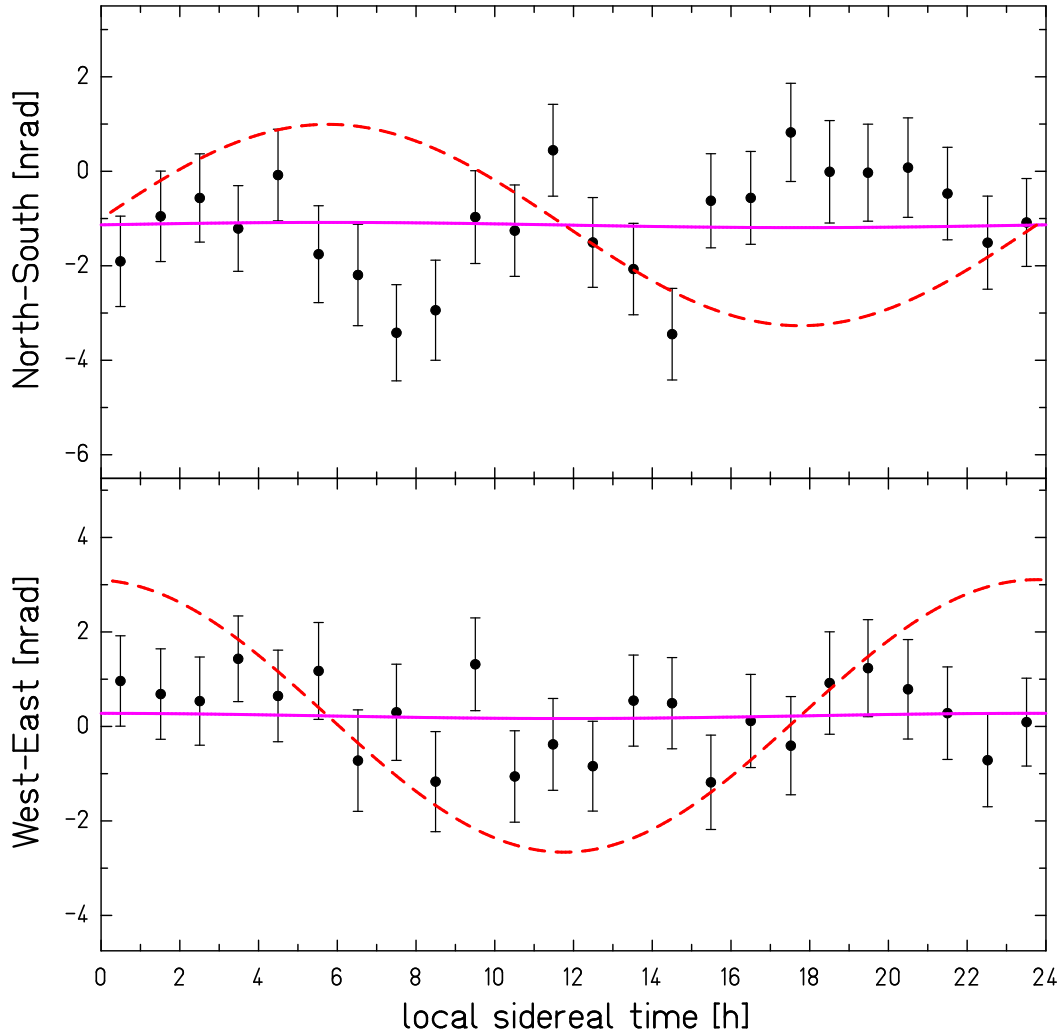


Figure 4.10: Cumulative results toward the galactic center for North-South and West-East components of the signal histogrammed as a function of the sidereal time of day. The solid curves show the mean result of fitting the individual data cycles. The dashed curves show a hypothetical signal for  $\Delta a = 2 \times 10^{-12} \text{ cm/s}^2$

## Chapter 5

### INVESTIGATION OF SYSTEMATIC EFFECTS

Understanding and controlling systematic effects is the most important task to make a convincing measurement. To determine our systematic effects, we exaggerated the source of each suspected systematic effect. Then we measured the response of the pendulum to the exaggerated source. The systematic sensitivity is defined by

$$S = \frac{\Delta a_1}{\Delta E_i} \quad (5.1)$$

where  $\Delta a_1$  is the amplitude measured by the pendulum at  $1\omega$  and  $\Delta E_i$  is the  $1\omega$  magnitude of the exaggerated quantity. The expected contribution of the systematic effect ( $\delta a_1$ ) to the Equivalence Principle data is then

$$\delta a_1 = \left( \frac{\Delta a_1}{\Delta E_i} \right) \delta E_i. \quad (5.2)$$

In this chapter, we discuss how we determined systematic effects and the systematic uncertainties.

#### **5.1 Gravity Gradient Effects**

One of the largest systematic effects in our measurements is due to the residual gravitational coupling between the pendulum and source masses around the pendulum. We used the multipole expansion to describe the pendulum and source masses in terms of gravity gradient moments ( $q_{lm}$ ) and the gravity gradient fields ( $Q_{lm}$ ) (section 2.4). The  $1\omega$  amplitude and phase of the residual coupling (Equation 2.21 and 2.46):

$$a_1 = \frac{8\pi G}{\kappa} \sum_{l=0}^{\infty} \frac{1}{2l+1} |\bar{q}_{l1}| |Q_{l1}|, \quad \phi_1 = \phi_{\bar{q}_{l1}} + \phi_{Q_{l1}}. \quad (5.3)$$

There are two ways to minimize this residual coupling. One way is to compensate the gravity gradient fields ( $Q_{l1}$ ) with gravity gradient compensators. The other way is to minimize the mass moments ( $q_{l1}$ ) of the pendulum. We used both techniques.

### 5.1.1 Gravity Gradient Fields

To measure the gravity gradient fields at the pendulum location, we used a gradiometer pendulum. Figure 5.1 shows the gradiometer pendulum in configurations that maximize its  $q_{21}$  and  $q_{31}$  moments, respectively. Table 5.1 summarizes the value of the gravity gradient moments of the gradiometer pendulum and of the fields of the compensators.

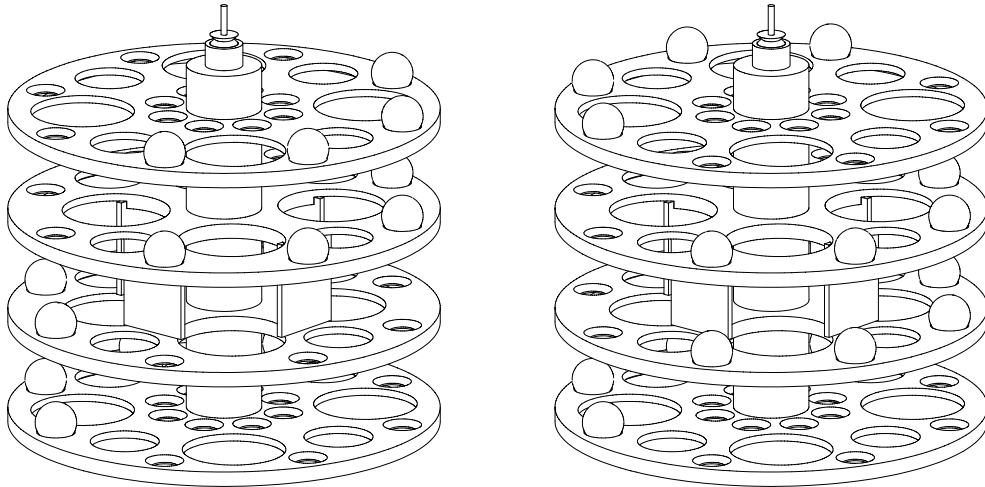


Figure 5.1: The gradiometer pendulum is shown in two configurations. The left side shows the  $q_{21}$  configuration and right side shows the  $q_{31}$  configuration.

The response of the  $q_{21}$ -gradiometer pendulum to the uncompensated gravity gradient field exceeds the dynamic range of our detector. Therefore, we took data with the gravity gradient compensators at angular positions that nearly compensated the field. We fitted our data with a circle. The center of the circle represents the signal generated by coupling of the gradiometer pendulum to the uncompensated ambient field and the radius gives the magnitude of the gradiometer pendulum coupling to the gravity gradient compensators

Table 5.1: Calculated values of mass moments of the gradiometers and compensators.

Calculated Gravity gradients	Amplitude	Phase(°)*
$q_{21}$ of Gradiometer	35.78 gcm <sup>2</sup>	
$q_{31}$ of Gradiometer	105.22 gcm <sup>3</sup>	
$Q_{21}$ of compensators	1.78 g/cm <sup>3</sup>	90.0
$Q_{22}$ of compensators	0.74 g/cm <sup>3</sup>	336.04
$Q_{31}$ of compensators	$1.06 \times 10^{-3}$ g/cm <sup>4</sup>	255.9

\* 0 ° is North and 90 ° is West.

alone. Typically, we measured the  $Q_{21}$  and  $Q_{31}$  gravity gradient fields before and after each data taking cycle.

#### $Q_{21}$ Gradient Field Measurements

The  $Q_{21}$  field was measured with the  $Q_{21}$ -compensator at several angular positions ( $\Theta = 0^\circ, 5^\circ, 10^\circ, -5^\circ$  and  $-10^\circ$ ). Figure 5.2 shows one of our  $Q_{21}$  measurements in which we compensated the source fields to within 0.9% of the original uncompensated magnitude. Our  $Q_{21}$  measurements are summarized in Table 5.2.

Table 5.2: The summary of the  $Q_{21}$  measurements.

Date	$Q_{21}$ of source	Phase(°)*	$Q_{21}$ of compensators
Jan. 2004	$(1.784 \pm 0.018)$ g/cm <sup>3</sup>	$270.2 \pm 0.1$	1.78 g/cm <sup>3</sup>
Feb. 2005	$(1.778 \pm 0.018)$ g/cm <sup>3</sup>	$270.3 \pm 0.1$	1.78 g/cm <sup>3</sup>
Oct. 2005	$(1.765 \pm 0.018)$ g/cm <sup>3</sup>	$270.0 \pm 0.1$	1.78 g/cm <sup>3</sup>
Feb. 2006	$(1.797 \pm 0.018)$ g/cm <sup>3</sup>	$270.0 \pm 0.1$	1.78 g/cm <sup>3</sup>

\* 0 ° is North and 90 ° is West.

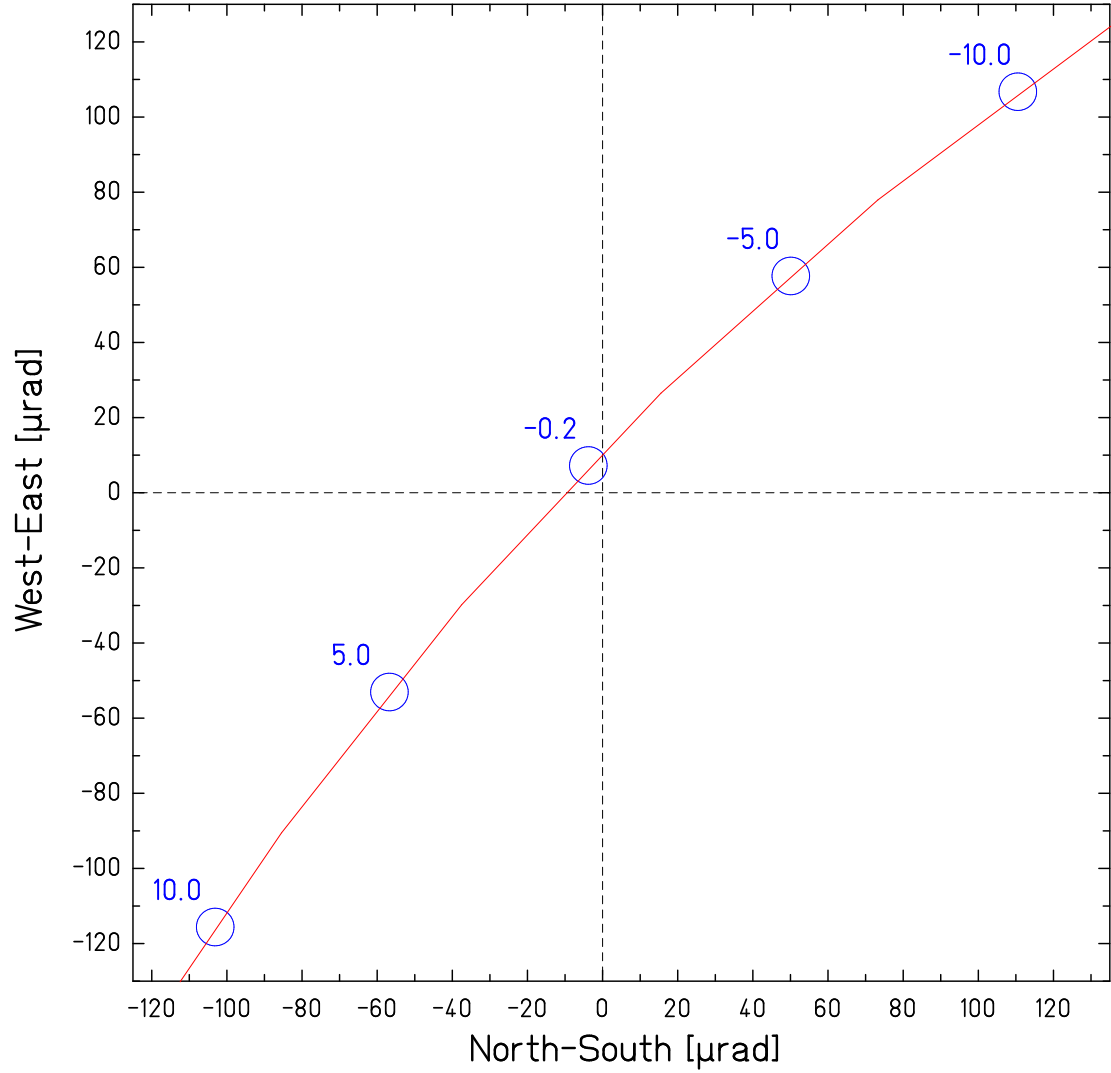


Figure 5.2: Measurement of the  $Q_{21}$  gravity gradient field. The uncertainties of the data points are typically 50 nrad and therefore too small to be shown. The numbers indicate the positions of the  $Q_{21}$  compensator and the uncertainties shown here are 5  $\mu\text{rad}$ .

### *$Q_{31}$ Gradient Field Measurements*

The  $Q_{31}$  source fields were measured with the  $Q_{31}$ -compensator at four compensator angular positions ( $\Theta = 0^\circ, 90^\circ, 180^\circ, 270^\circ$ ). Figure 5.3 shows one of our  $Q_{31}$  measurements in which we compensated the source fields to within 3.0% of the original uncompensated magnitude. The  $Q_{31}$  measurements are summarized in Table 5.3 .

Table 5.3: The summary of the  $Q_{31}$  measurements.

Date	$Q_{31}$ of source	Phase( $^\circ$ )*	$Q_{31}$ of compensators
Feb. 2005	$(1.08 \pm 0.01) \times 10^{-3} \text{ g/cm}^4$	$72.9 \pm 0.4$	$1.06 \times 10^{-3} \text{ g/cm}^4$
Mar. 2005	$(1.06 \pm 0.01) \times 10^{-3} \text{ g/cm}^4$	$73.6 \pm 0.2$	$1.06 \times 10^{-3} \text{ g/cm}^4$
Oct. 2005	$(1.09 \pm 0.01) \times 10^{-3} \text{ g/cm}^4$	$75.4 \pm 0.2$	$1.06 \times 10^{-3} \text{ g/cm}^4$
Feb. 2006	$(1.08 \pm 0.01) \times 10^{-3} \text{ g/cm}^4$	$77.6 \pm 0.4$	$1.06 \times 10^{-3} \text{ g/cm}^4$

\*  $0^\circ$  is North and  $90^\circ$  is West.

### *5.1.2 Gravity Gradient Moments of the Pendulum*

Since the 8 test body Eöt-Wash III torsion pendulum (Figure 3.3) is highly symmetric, the  $m = 1$  gravity gradient moments of the pendulum up to  $l=5$  are vanishing by design. Nevertheless, due to the machining imperfections, the pendulum has residual gravity gradient moments such as  $q_{21}$ ,  $q_{31}$  and etc .... We used four sets of the tuning screws on the pendulum to minimize its  $q_{21}$  and  $q_{31}$  moments. We monitored and measured the  $q_{21}$  and the  $q_{31}$  moments of the pendulum during our systematic tests.

#### *Minimizing the $q_{21}$ Moment of the Pendulum*

The  $q_{21}$  moment of the pendulum was about  $5 \times 10^{-2} \text{ gcm}^2$  before any adjustments. After several  $q_{21}$  tuning iterations, this value was reduced to about  $2 \times 10^{-3} \text{ gcm}^2$ . Figure 5.4

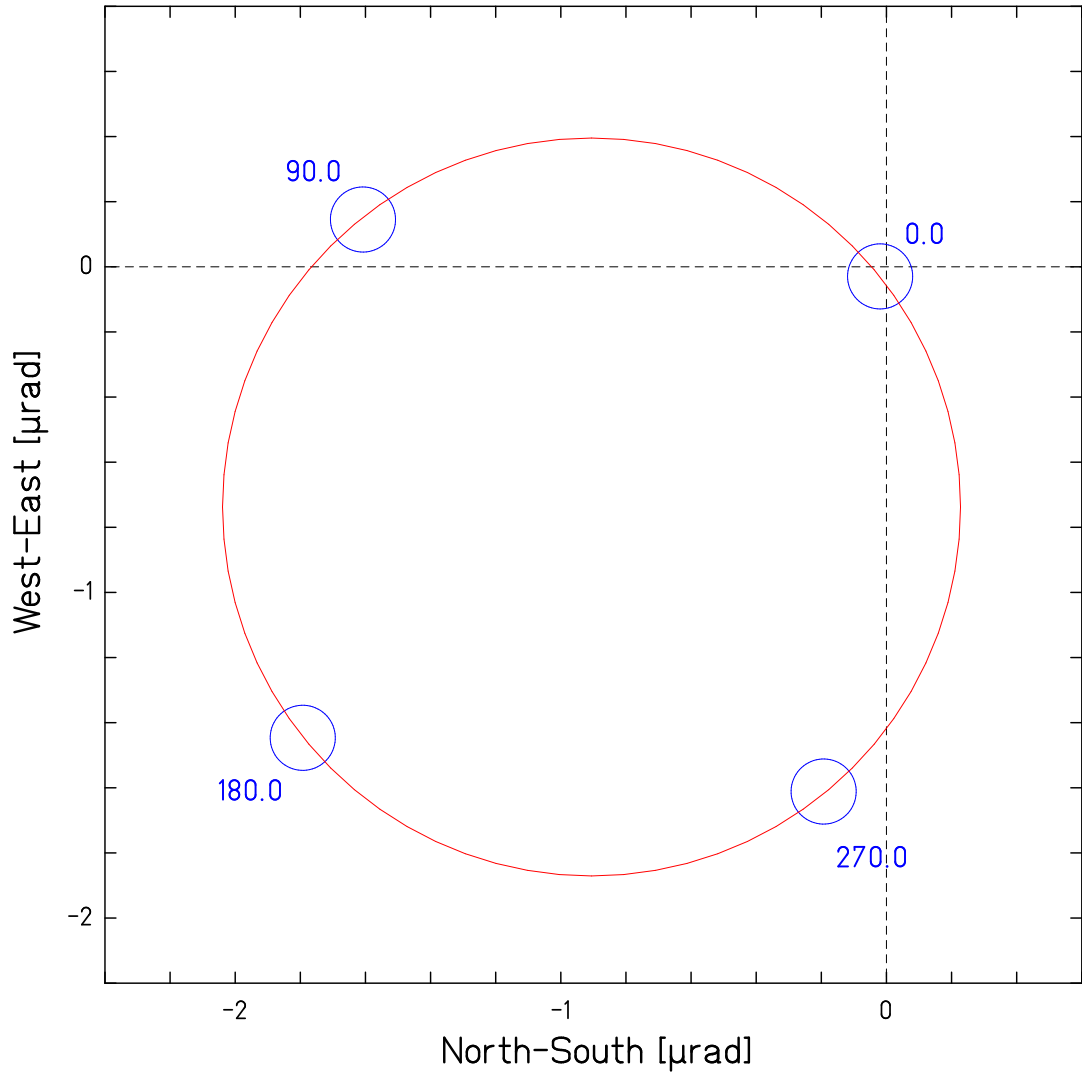


Figure 5.3: Measurement of the  $Q_{31}$  gravity gradient field. The uncertainties of the data points are typically 10 nrad and therefore too small to be shown. The numbers indicate the positions of the  $Q_{31}$  compensator and the uncertainties shown here are 100 nrad.

shows the deflection angle of the pendulum with the  $Q_{21}$  compensators at  $180^\circ$  (i.e. doubling the uncompensated ambient gradient field). The top panel shows the signal before the tuning procedure started and bottom panel shows the final signal after the tuning procedure was finished. Table 5.4 summarizes one of the tuning procedures of the  $q_{21}$  moment.

Table 5.4: Progression of the tuning procedure of the pendulum moment.

# of Trimming <sup>†</sup>	$q_{21}$ moment of the pendulum
1	$(5.01 \pm 0.06) \times 10^{-2} \text{ gcm}^2$
2	$(4.1 \pm 0.3) \times 10^{-3} \text{ gcm}^2$
3	$(1.64 \pm 0.06) \times 10^{-3} \text{ gcm}^2$

<sup>†</sup> We turned the tuning screws 3 times until we were satisfied with the magnitude of the residual moment.

#### *Measurements of $q_{21}$ and $q_{31}$ Moments of the Pendulum*

To determine the moments of the pendulum we took measurements with the compensators in two different positions ( $0^\circ$ ,  $180^\circ$ ) that virtually nulled and doubled the gradients. From the difference between the two measurements we found the signal that only coupled to the compensators. We calculated the moments of the pendulum using Equation 5.3. Figure 5.5 shows the configuration of the  $Q_{21}$  and  $Q_{31}$  compensators used to measure the moments of pendulum. Table 5.5 and 5.6 summarize the measured moments of the pendulum, after tuning of the trim screws was completed.

##### *5.1.3 Residual Gravity Gradient Signal*

The residual  $Q_{21}$  and  $Q_{31}$  fields of the source masses reduced by the compensators are summarized in Table 5.7. Table 5.8 shows the expected residual signals due to the residual gravitational coupling. We corrected our final data with these residual signals. (Chapter 7)

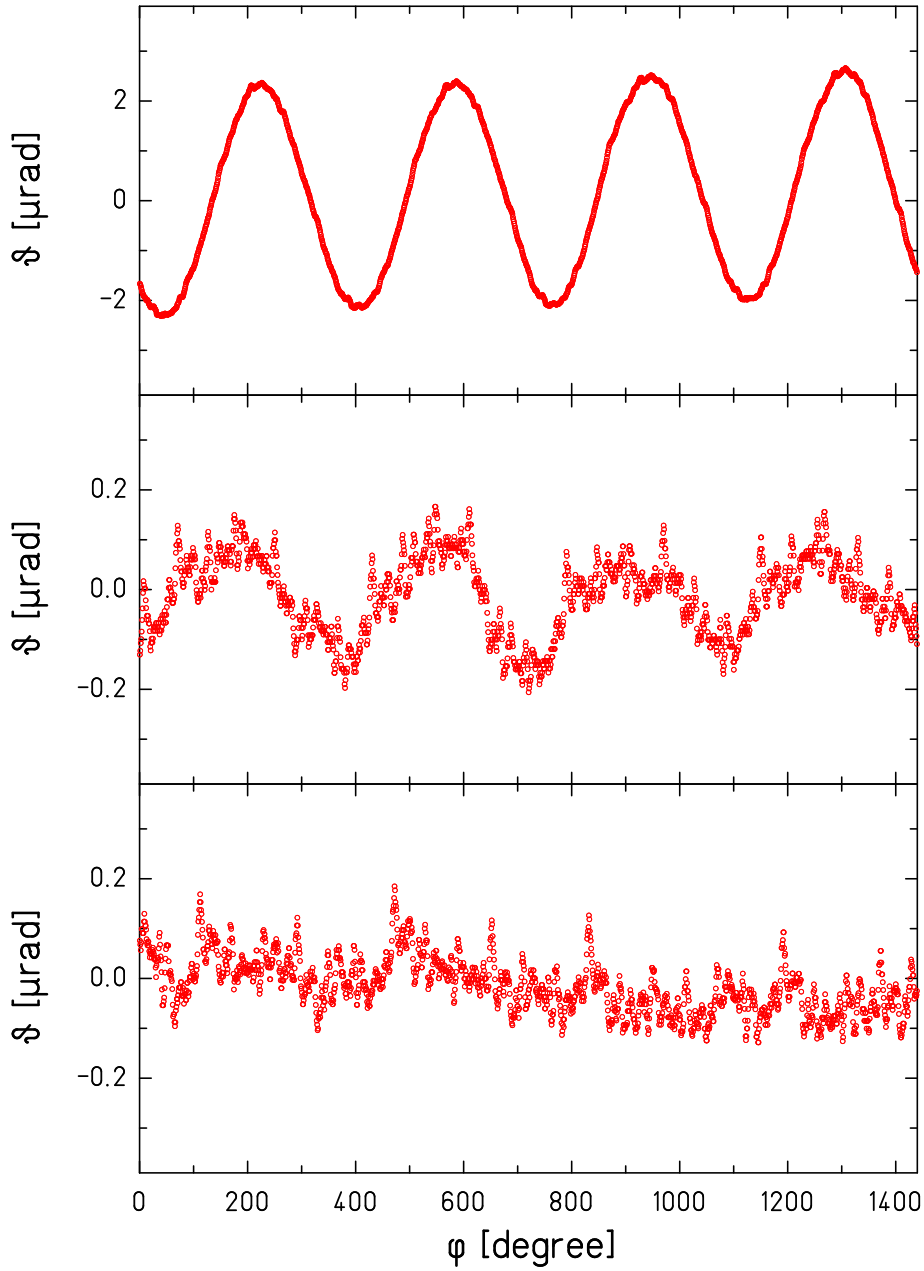


Figure 5.4: The deflection angle of the pendulum during the tuning iteration. The top panel shows the signal before the tuning procedure started, the middle panel shows the signal at an intermediate measurement, and bottom panel shows the final signal after the tuning procedure was finished. The data shown were taken with the  $Q_{21}$  compensator at  $180^\circ$  position.

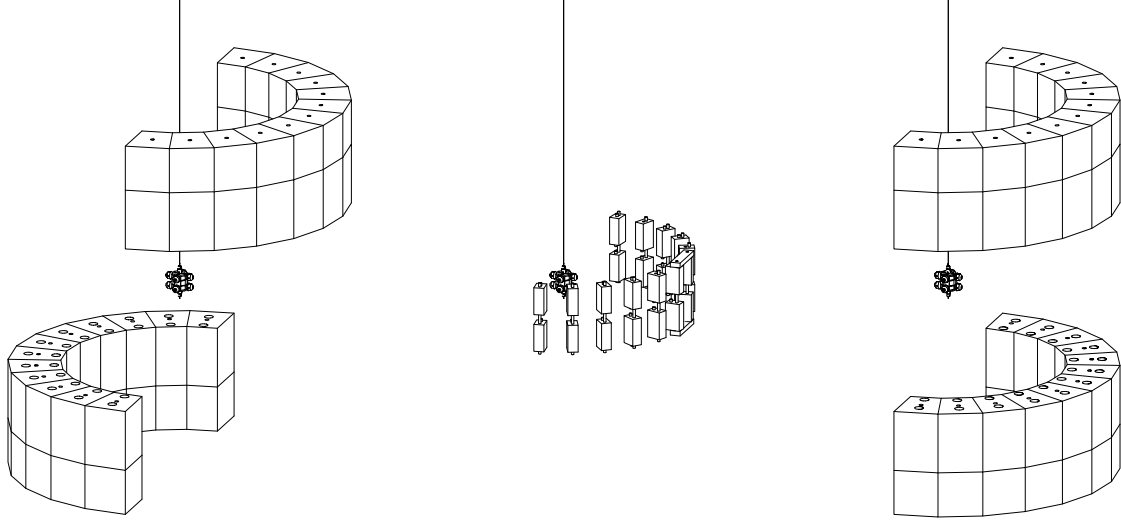


Figure 5.5: The left diagram shows the  $Q_{21}$  compensators configuration for the measurements of the  $q_{21}$  moment of the pendulum, the middle diagram shows  $Q_{31}$  compensators for measuring  $q_{31}$  moment of the pendulum and the right diagram shows exaggerated  $Q_{31}$  configuration of using the  $Q_{21}$  compensators to measure the  $q_{31}$  moment of the pendulum.

Table 5.5: Summary of the measurements of  $q_{21}$  moments of the pendulum.

Date	$q_{21}$ moment of the pendulum	Phase( $^{\circ}$ ) <sup>*</sup>	$Q_{21}$ of the compensators
Feb. 2004	$(1.4 \pm 0.1) \times 10^{-3} \text{ gcm}^2$	$54 \pm 3$	$1.78 \text{ g/cm}^3$
Nov. 2004	$(5.3 \pm 0.2) \times 10^{-3} \text{ gcm}^2$	$93 \pm 2$	$1.78 \text{ g/cm}^3$
Mar. 2005 <sup>†</sup>	$(1.3 \pm 0.1) \times 10^{-3} \text{ gcm}^2$	$96 \pm 4$	$1.78 \text{ g/cm}^3$
Aug. 2005 <sup>†</sup>	$(2.4 \pm 0.1) \times 10^{-3} \text{ gcm}^2$	$127 \pm 3$	$1.78 \text{ g/cm}^3$
Nov. 2005 <sup>†</sup>	$(1.6 \pm 0.1) \times 10^{-3} \text{ gcm}^2$	$358 \pm 2$	$1.78 \text{ g/cm}^3$
Jan. 2006 <sup>†</sup>	$(1.7 \pm 0.1) \times 10^{-3} \text{ gcm}^2$	$347 \pm 3$	$1.78 \text{ g/cm}^3$

\*  $0^{\circ}$  is North and  $90^{\circ}$  is West.

<sup>†</sup> Data were taken after we reversed the dipole configuration in Jan. 2005.

Table 5.6: Summary of the measurements of  $q_{31}$  moments of the pendulum.

Date	$q_{31}$ moment of the pendulum	Phase( $^\circ$ ) <sup>*</sup>	$Q_{31}$ of the compensators
Feb. 2004	$(9 \pm 13) \times 10^{-1} \text{ gcm}^3$	$160 \pm 60$	$6.61 \times 10^{-4} \text{ g/cm}^4$ †
Dec. 2004	$(2 \pm 3) \times 10^{-1} \text{ gcm}^3$	$240 \pm 120$	$1.06 \times 10^{-3} \text{ g/cm}^4$ †
Mar. 2005 <sup>§</sup>	$(1.3 \pm 0.1) \times 10^{-1} \text{ gcm}^3$	$337 \pm 3$	$2.68 \times 10^{-2} \text{ g/cm}^4$ ‡
Aug. 2005 <sup>§</sup>	$(1.6 \pm 0.1) \times 10^{-1} \text{ gcm}^3$	$333 \pm 4$	$2.68 \times 10^{-2} \text{ g/cm}^4$ ‡
Feb. 2006	$(1.0 \pm 0.1) \times 10^{-1} \text{ gcm}^3$	$17 \pm 9$	$2.68 \times 10^{-2} \text{ g/cm}^4$ ‡

\*  $0^\circ$  is North and  $90^\circ$  is West.

† We measured the  $q_{31}$  moment of pendulum with  $Q_{31}$  compensators.

‡ We measured the  $q_{31}$  moment of the pendulum with  $Q_{21}$  compensators configured to exaggerate the  $Q_{31}$  gravity gradient fields.

§ Data were taken after we reversed the dipole configuration in Jan. 2005.

Table 5.7: Summary of the residual  $Q_{21}$  and  $Q_{31}$  fields.

Date	$Q_{21}$ ( $\text{g/cm}^3$ )	Phase( $^\circ$ )	$Q_{31}$ ( $\text{g/cm}^4$ )	Phase( $^\circ$ ) <sup>*</sup>
Feb. 2005	$(7.3 \pm 0.3) \times 10^{-3}$	$327 \pm 2$	$(4.12 \pm 0.05) \times 10^{-4}$	$68.0 \pm 0.4$
Mar. 2005	$(1.0 \pm 0.1) \times 10^{-2}$	$14 \pm 2$	$(4.4 \pm 4.6) \times 10^{-5}$	$348 \pm 18$
Oct. 2005	$(1.54 \pm 0.03) \times 10^{-2}$	$86.2 \pm 0.1$	$(3.4 \pm 0.3) \times 10^{-5}$	$61 \pm 4$
Feb. 2006 <sup>†</sup>	$(1.69 \pm 0.06) \times 10^{-2}$	$267.4 \pm 0.1$	$(5.85 \pm 0.06) \times 10^{-4}$	$4 \pm 1$

\*  $0^\circ$  is North and  $90^\circ$  is West.

†  $Q_{31}$  compensator was accidentally at  $329^\circ$  position.

Table 5.8: The expected signals from gravity gradient fields.

Data set	North-South component	East-West component
I	(-1.36 ± 1.68) nrad	(-1.94 ± 1.93) nrad
II	(-0.19 ± 0.18) nrad	(-0.08 ± 0.18) nrad
III <sup>†</sup>	( 0.72 ± 0.13) nrad	( 0.26 ± 0.39) nrad

<sup>†</sup>  $Q_{31}$  compensator was accidentally at 329° position.

## 5.2 Turntable Effects

The turntable of the apparatus is rotated at an extremely constant angular speed using a feedback loop. The angle of the turntable is measured with an angle encoder with two optical readouts. Non-linearities in this readout causes small accelerations at the rotation frequency and at its higher harmonics. We can describe the turntable angle in the lab frame by

$$\phi = \omega t + \sum_{n=1}^{\infty} \Phi_n e^{in\omega t} \quad (5.4)$$

where the  $\Phi_n$  are the amplitudes of the non-linearities at the various harmonics of the angle encoder. The equation of the motion of the pendulum in the rotating frame (Equation 2.12 is:

$$\ddot{\theta} + 2\gamma\dot{\theta} + \omega_0^2(1 + i\epsilon)\theta = T(t)/I - \ddot{\phi}. \quad (5.5)$$

Let us assume the case of no damping term and no external torque term. Then Equation 5.5 becomes

$$\ddot{\theta} + \omega_0^2(1 + i\epsilon)\theta = \sum_{n=1}^{\infty} n^2 \omega^2 \Phi_n e^{in\omega t}. \quad (5.6)$$

And the solution is

$$\theta = \sum_{n=1}^{\infty} \frac{n^2 \omega^2}{(\omega_0^2 - n^2 \omega^2) + i\epsilon\omega_0^2} \Phi_n e^{in\omega t}. \quad (5.7)$$

To minimize the turntable speed variations, we corrected the angle readout by adding 9 harmonic correction terms to the angle used for running the turntable feedback. By com-

bining data with different dipole directions, we effectively eliminated residual turntable speed variation effects from the Equivalence Principle data as shown section 4.4.7.

### 5.3 Tilt Effects

#### 5.3.1 Tilt

Due to the imperfections in the torsion fiber support and due to imperfections of the mirrors on the pendulum, a tilt of the torsion balance produced a systematic angular excursion of the pendulum. This effect is particularly troublesome since it produces an effect that is at  $1\omega$  and is not eliminated by reversing the pendulum orientation. We used two pairs of electronic tilt sensors (AGIs) to monitor the tilt of the apparatus. One pair (top AGI) is located at 170 cm above the pendulum and its signal is used as the reference signal for our active thermal expansion feet leveling system. The other pair (bottom AGI) is located at 23 cm below the pendulum. We used this sensor to infer the direction of local vertical near the pendulum position. Because local vertical is different between top and bottom AGI positions, we observed a  $(51.39 \pm 0.25)$  nrad tilt angle with the bottom AGI. Figure 5.6 shows the tilt measurements of Data set III on the bottom AGI. The bottom AGI signal includes a signal from the  $Q_{21}$  compensator of  $(10.16 \pm 0.48)$  nrad. Since there was no effect of the compensator at the pendulum, we had to subtract this signal to calculate the tilt angle at the pendulum position. We assumed that the local vertical changed with height linearly for this calculation. Table 5.9 shows the summary of the tilt angles.

Table 5.9: The summary of the tilt angles.

	$t_1^s$	$t_1^c$
Tilt angle at bottom AGI	$(33.45 \pm 0.24)$ nrad	$(-39.01 \pm 0.25)$ nrad
Extra signal from compensator	$(-4.89 \pm 0.44)$ nrad	$(8.90 \pm 0.49)$ nrad
Expected tilt angle on pendulum	$(33.13 \pm 0.33)$ nrad	$(-42.34 \pm 0.36)$ nrad

### 5.3.2 Tilt Sensitivity

To determine the tilt sensitivity, we exaggerated the tilt of the apparatus and measured the response of the pendulum. From this measurement we calculated the tilt sensitivity. The expected signal ( $\Theta_{NS}, \Theta_{WE}$ ) on the pendulum from the tilt ( $t_1^s, t_1^c$ ) of the apparatus is given by

$$\begin{pmatrix} \Theta_{NS} \\ \Theta_{WE} \end{pmatrix} = \begin{pmatrix} m_t \cos \phi & m_t \sin \phi \\ -m_t \sin \phi & m_t \cos \phi \end{pmatrix} \begin{pmatrix} t_1^s \\ t_1^c \end{pmatrix} \quad (5.8)$$

where  $m_t$  is tilt feedthrough, which is the ratio between the expected signal on the pendulum and the tilt of the apparatus, and  $\phi$  is the direction along the tilt effect. Table 5.10 summarizes the sensitivities of all mirrors of the pendulum.

Table 5.10: The summary of the tilt sensitivities.

	0° mirror	90° mirror	180° mirror	270° mirror
$m_t$	(0.067 ± 0.004)	(0.028 ± 0.003)	(0.008 ± 0.003)	(0.019 ± 0.006)
$\phi$	(53 ± 6)°	(85 ± 7)°	(2 ± 28)°	(-30 ± 15)°

### 5.3.3 Expected Signal of the Tilt Effect

Based on the tilt sensitivities and the calculation of the expected tilt angle at the pendulum position (Table 5.9 and Table 5.10) we could calculate the expected signal due to tilt. Table 5.11 shows the expected signals of the tilt effect. We corrected our final data for these signals. (Chapter 7)

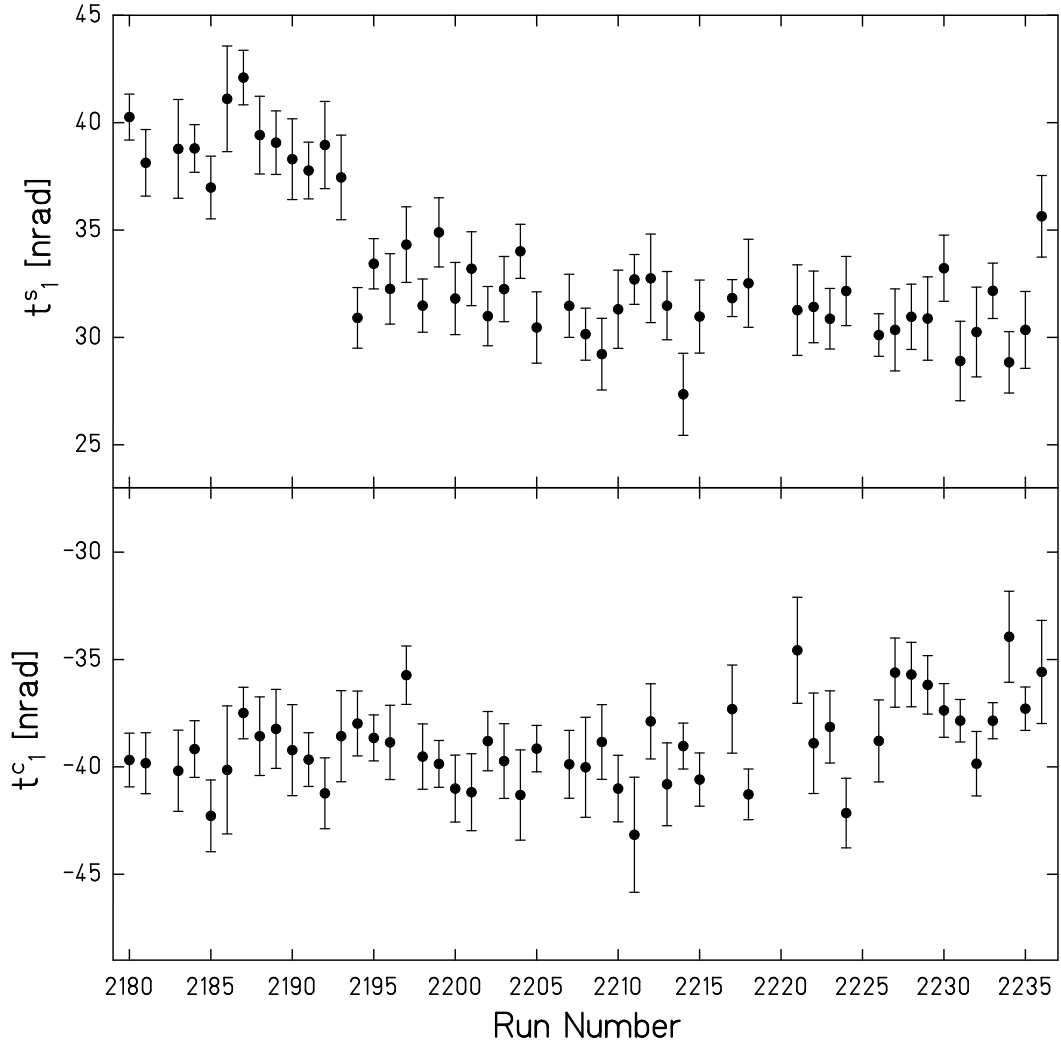


Figure 5.6: The tilt signal on bottom AGI for Data set III.  $t_1^s$  and  $t_1^c$  are the fitting parameters (4.6) of  $1\omega$  signal of the tilt. Since the tilt sensors installed with  $60^\circ$  offset respect to the autocollimator, there was  $60^\circ$  phase difference between  $1\omega$  signal of the tilt and the pendulum.

Table 5.11: The expected signals of the tilt effect.

Data set	data cycle	North-South component	East-West component
III	1	(-0.53 ± 0.52) nrad	(-1.68 ± 0.48) nrad
	2	(-0.62 ± 0.50) nrad	(-1.53 ± 0.48) nrad
	3	( 0.27 ± 0.38) nrad	(-1.01 ± 0.40) nrad
	4	(-0.59 ± 0.48) nrad	(-1.39 ± 0.46) nrad
	mean value*	(-0.27 ± 0.47) nrad	(-1.39 ± 0.46) nrad

\* The uncertainties given in this Table are systematic uncertainties and can not be treated as statistical uncertainties.

#### 5.4 Thermal Effects

To determine thermal effects we did temperature gradient tests with two water circulating systems near the apparatus. Figure 5.7 is a picture of the experimental setup of the test. To produce the exaggerated temperature gradient, hot water was circulated through one side and cold water was circulated through the other side. Figure 5.8 shows the temperature gradient set-point of the water circulating systems and the temperature pickup signal of the temperature sensor. Figure 5.8 shows the signals of all four mirrors measured at 7 C° difference in the set-points of the water circulating systems. With this setup the signal measured by the temperature sensor was  $(1147 \pm 2)$  mK and the signal on pendulum was  $(4.01 \pm 3.62)$  nrad. This resulted in a temperature feedthrough of  $(3.5 \pm 3.2) \times 10^{-3}$  nrad/mK. During normal runs this temperature sensor recorded a  $(56.4 \pm 0.2)$  mK signal, resulting in a temperature-driven effect of  $(0.20 \pm 0.18)$  nrad. We adopted  $\pm 0.38$  nrad as a conservative systematic uncertainty for the thermal effect. Since we could not properly resolve the direction of the uncertainty, we used  $\pm 0.38$  nrad for the uncertainties of both of North-South component and East-West component.



Figure 5.7: A picture of the setup of the temperature gradient test.

### **5.5 Magnetic Effects**

A magnetic moment on the pendulum could interact with any magnetization around pendulum. We measured the magnetic moment of the pendulum by applying external magnetic fields and observing its response. A permanent magnet was placed at 21.5 cm apart from the pendulum position. By changing the direction of the magnet we produced a differential horizontal 34 G field at the pendulum position and measured the induced  $(12.97 \pm 6.47)$  nrad signal. This resulted in a magnetic feedthrough of 0.382 nrad/G. During normal run the magnetic field at the pendulum position was  $\leq 0.1$  G which was measured by a flux gate magnetometer. Therefore, the uncertainty associated with a magnetic coupling was  $\pm 0.04$  nrad. Figure 5.10 shows the signals of the magnetic tests. The direction of the uncertainty for magnetic effects was treated the same way as the thermal effect uncertainty.

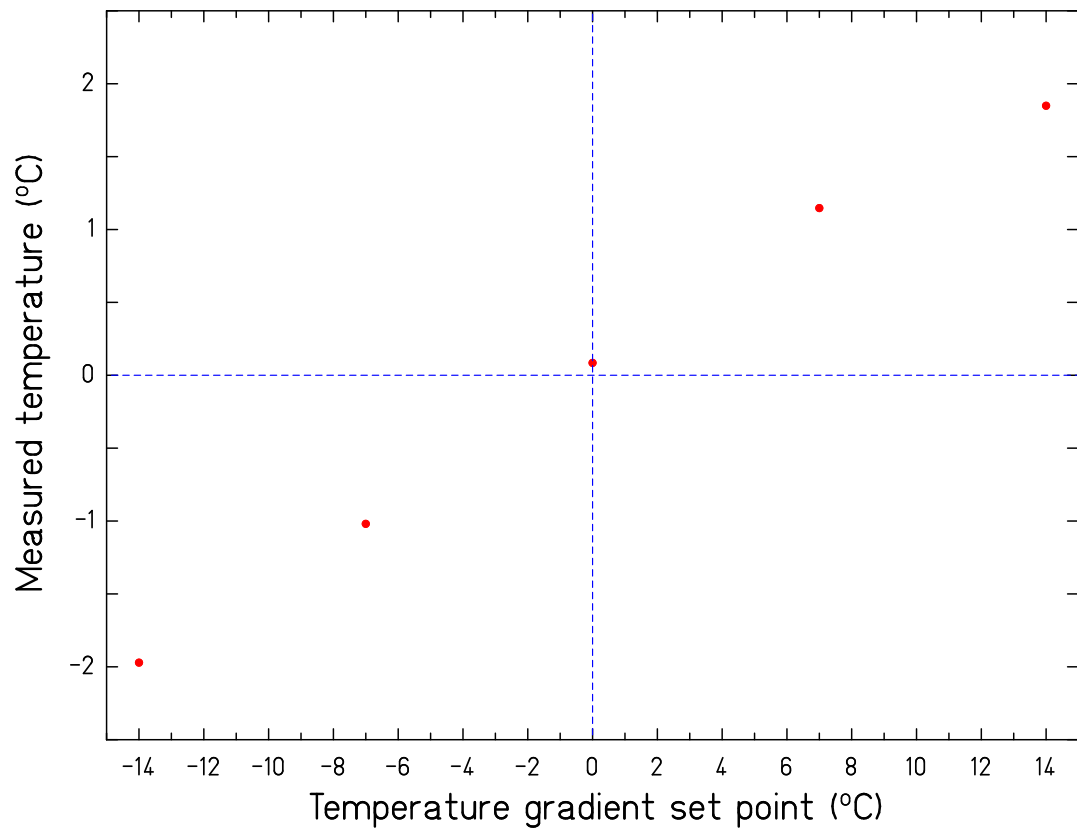


Figure 5.8: The measured temperature of gradient on the rotating part of the apparatus versus the set-point of the temperature gradient.

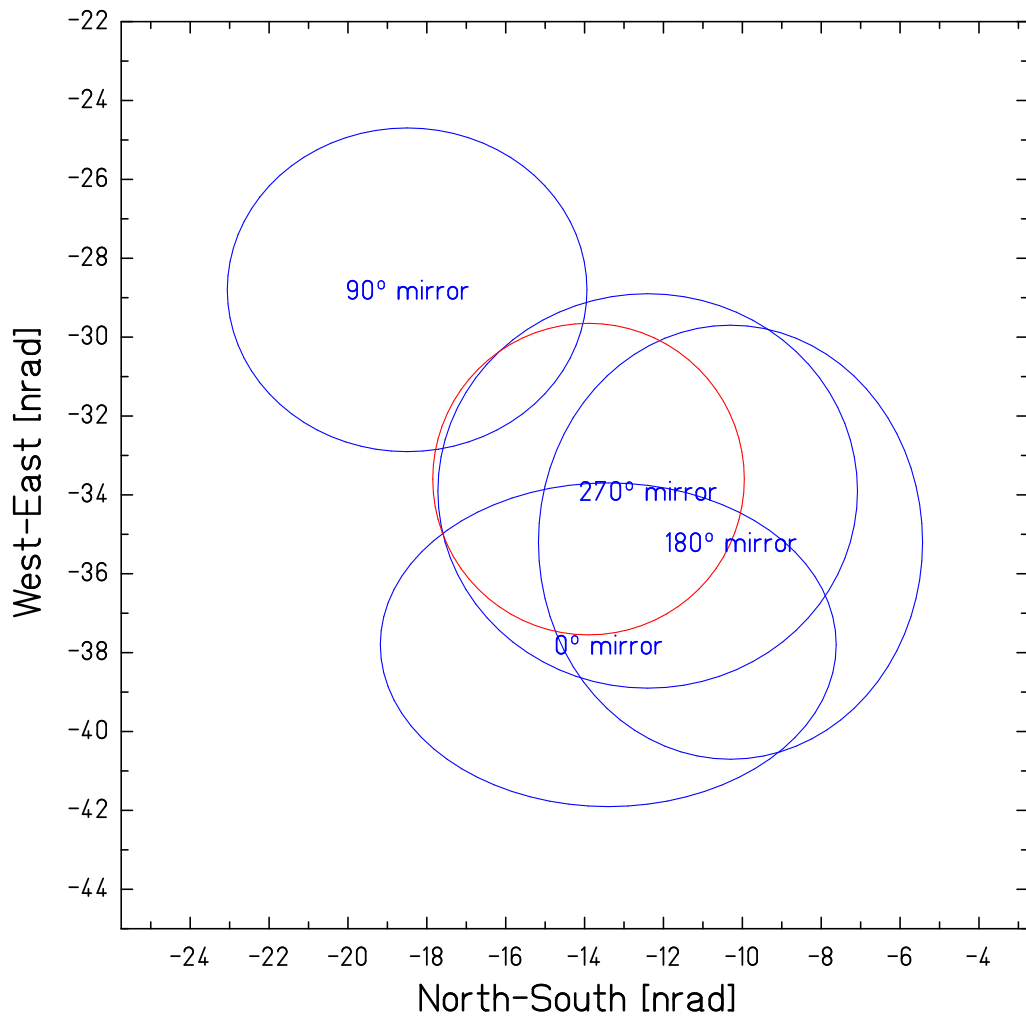


Figure 5.9:  $1\omega$  signal taken four pendulum dipole directions at 7° set-point of the temperature gradient.

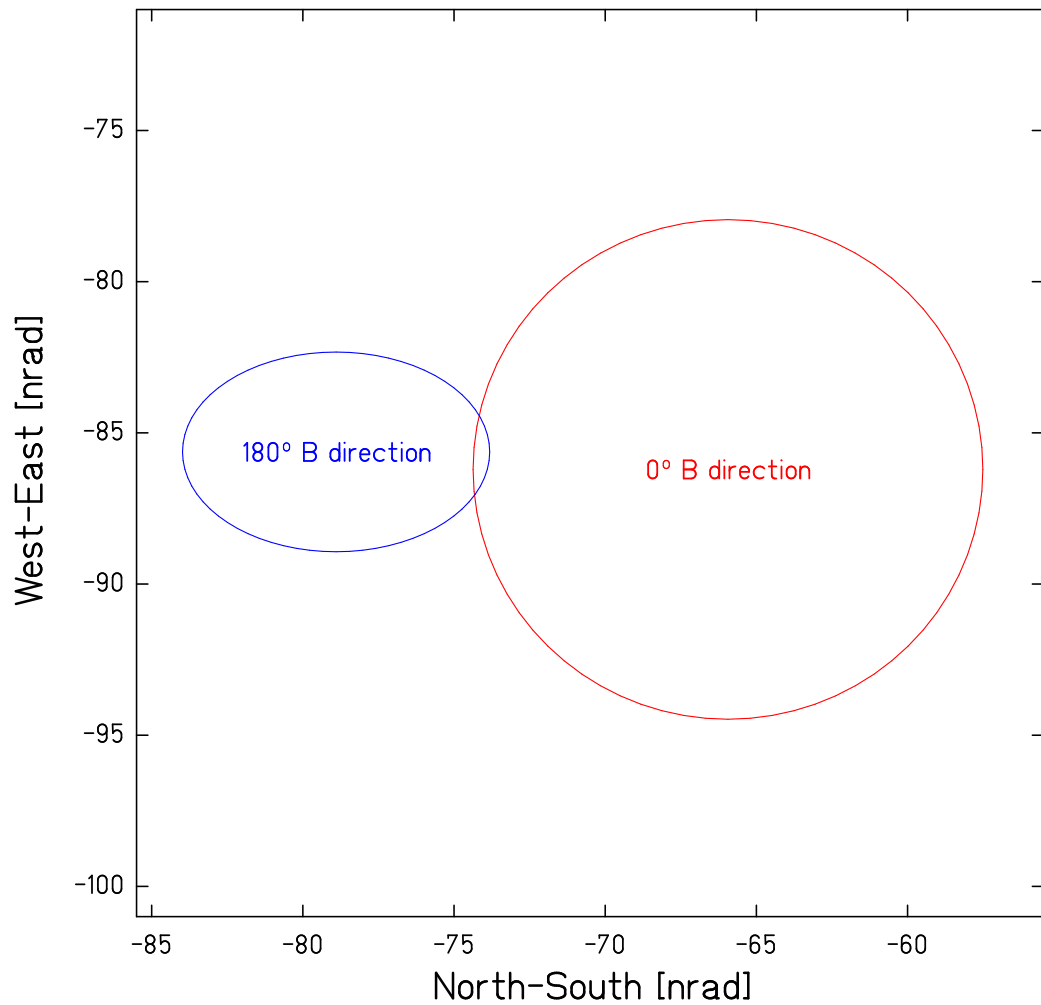


Figure 5.10: The  $1\omega$  signal measured with a magnetic field difference of 34 G.

### **5.6 Summary of the Systematic Uncertainties**

Table 5.12 summarizes the systematic uncertainties for the angular deflection angle. We added all of the uncertainties in quadrature. We used these uncertainties for our final data. (Chapter 7)

Table 5.12: Systematic uncertainty budget for the angular deflection angle.

Effects	North-South component	East-West component
Gravity gradient	0.13 nrad	0.39 nrad
Tilt	0.47 nrad	0.46 nrad
Temperature	0.38 nrad	0.38 nrad
Magnetic	0.04 nrad	0.04 nrad
Total	0.62 nrad	0.71 nrad

## Chapter 6

### THE SOURCE INTEGRATION

#### 6.1 The Source Strength

The field of a new composition dependent interaction can be described by a Yukawa potential,

$$V_{AB}(r) = \alpha_5 \left( \frac{q_5}{\mu} \right)_A \left( \frac{q_5}{\mu} \right)_B G \frac{m_A m_B}{r} e^{-r/\lambda}, \quad (6.1)$$

where  $\alpha_5$  denotes a dimensionless coupling constant,  $G$  is Newton's constant,  $m_i$  are the mass as of point-like test-bodies,  $r$  is the distance between the  $m_i$ . The  $q_5$  and  $\lambda$  are the composition-dependent test-body charges and the interaction range, and  $\mu$  is the test-body mass in atomic mass units (*amu*). We can generalize the Yukawa potential for a test-body on the pendulum and an arbitrary source mass distribution  $\rho_s(\vec{r}')$  to

$$V(|\vec{r} - \vec{r}'|) = \alpha_5 G m_A \left( \frac{q_5}{\mu} \right)_A \int d^3 r' \rho_s(\vec{r}') \left( \frac{q_5}{\mu} \right)_s \frac{e^{-|\vec{r} - \vec{r}'|/\lambda}}{|\vec{r} - \vec{r}'|}, \quad (6.2)$$

where  $\vec{r}$  and  $\vec{r}'$  denote the position of the test-body and the source mass elements. The origin is located at the center of mass of the pendulum. The force on the test-body caused by the Yukawa potential is

$$\vec{F} = -\nabla_r V = m_A \vec{a}, \quad (6.3)$$

and the acceleration on a test-body is

$$\vec{a} = -\alpha_5 G \left( \frac{q_5}{\mu} \right)_A \nabla_r \int d^3 r' \rho_s(\vec{r}') \left( \frac{q_5}{\mu} \right)_s \frac{e^{-|\vec{r} - \vec{r}'|/\lambda}}{|\vec{r} - \vec{r}'|}. \quad (6.4)$$

The differential acceleration of two different composition test-bodies caused by the Yukawa potential is given by

$$\Delta \vec{a} = -\alpha_5 G \Delta \left( \frac{q_5}{\mu} \right)_p \nabla_r \int d^3 r' \rho_s(\vec{r}') \left( \frac{q_5}{\mu} \right)_s \frac{e^{-|\vec{r} - \vec{r}'|/\lambda}}{|\vec{r} - \vec{r}'|}, \quad (6.5)$$

where the  $\Delta \left( \frac{q_5}{\mu} \right)_p$  denotes  $\left( \frac{q_5}{\mu} \right)_A - \left( \frac{q_5}{\mu} \right)_B$ .

$$\Delta \vec{a} = -\alpha_5 \Delta \left( \frac{q_5}{\mu} \right)_p \vec{I}. \quad (6.6)$$

where  $\vec{I}$  is called *the source strength*.

From the Equation 6.5 and 6.6,  $\vec{I}$  is defined by

$$\vec{I} = G \nabla_r \int d^3 r' \rho_s(\vec{r}') \left( \frac{q_5}{\mu} \right)_s \frac{e^{-|\vec{r}-\vec{r}'|/\lambda}}{|\vec{r}-\vec{r}'|} \quad (6.7)$$

$$= G \int d^3 r' \rho_s(\vec{r}') \left( \frac{q_5}{\mu} \right)_s e^{-|\vec{r}-\vec{r}'|/\lambda} \left( -\frac{(\vec{r}-\vec{r}')}{|\vec{r}-\vec{r}'|^3} - \frac{(\vec{r}-\vec{r}')}{\lambda |\vec{r}-\vec{r}'|^2} \right), \quad (6.8)$$

where the  $r$  and  $r'$  denote the radial coordinates of the point-like test-body on the pendulum and a source mass element, respectively. In our experiments,  $r \ll r'$  so that we can assume  $|\vec{r}-\vec{r}'| \approx r'$  and  $(\vec{r}-\vec{r}') \approx -\vec{r}'$ . Therefore,

$$\vec{I} \approx G \int d^3 r' \rho_s(\vec{r}') \left( \frac{q_5}{\mu} \right)_s e^{-r'/\lambda} \left( \frac{\vec{r}'}{r'^3} + \frac{\vec{r}'}{\lambda r'^2} \right) \quad (6.9)$$

$$= G \int d^3 r' \rho_s(\vec{r}') \left( \frac{q_5}{\mu} \right)_s \left( \frac{1}{r'} + \frac{1}{\lambda} \right) \frac{e^{-r'/\lambda}}{r'} \hat{r}'. \quad (6.10)$$

For our experiments, we are interested in the horizontal component of the differential acceleration because only the horizontal component of the differential acceleration produces a torque on the torsion pendulum. From Equation 6.6

$$\Delta \vec{a}_\perp = -\alpha_5 \Delta \left( \frac{q_5}{\mu} \right)_p \vec{I}_\perp. \quad (6.11)$$

The horizontal and vertical components of the source strength are

$$\vec{I}_\perp = G \int d^3 r' \rho_s(\vec{r}') \left( \frac{q_5}{\mu} \right)_s \left( \frac{1}{r'} + \frac{1}{\lambda} \right) \frac{e^{-r'/\lambda}}{r'} (\hat{i} \sin \theta' \cos \phi' + \hat{j} \sin \theta' \sin \phi') \quad (6.12)$$

$$\vec{I}_\parallel = G \int d^3 r' \rho_s(\vec{r}') \left( \frac{q_5}{\mu} \right)_s \left( \frac{1}{r'} + \frac{1}{\lambda} \right) \frac{e^{-r'/\lambda}}{r'} (\hat{k} \cos \theta'). \quad (6.13)$$

In this chapter, we will explain how we calculate the horizontal components of the source strength.

## 6.2 The Location of the Apparatus

Our apparatus is located in the cyclotron room (Figure 6.1) of the Center for Experimental Nuclear Physics and Astrophysics (CENPA). The CENPA building (Figure 6.2) is located in the northeast corner of the campus of the University of Washington at a longitude of  $122.30^\circ$  West and latitude of  $47.66^\circ$  North. Our pendulum is located 76.2 cm from the wall on the west side of the cyclotron room and 241.3 cm above the floor.

## 6.3 Calculation

To calculate the source strength, we have to model the mass distribution surrounding the pendulum. This includes such things as the cyclotron room, the nearby hillside, the surrounding terrain of the Seattle, Lake Washington, etc.

### 6.3.1 The Effective Source Masses

All the objects around the pendulum must be considered as source masses. Not all of them, however, affect the calculation significantly, so that we need to consider only the effective masses. Equation 6.12 indicates the conditions for the effective mass:

1. the  $r'$ -dependence of  $\vec{I}_\perp$  requires the effective masses to lie within a certain distance,  $\lambda$ , from the pendulum. We can ignore sources with  $r' \gg \lambda$ .
2. masses directly above and below contribute insignificantly.
3. the angular dependence of  $\vec{I}_\perp$  requires that the effective masses should be asymmetric to the horizontal plane because the symmetrically distributed source mass cannot contribute to  $\vec{I}_\perp$ .

### 6.3.2 Model of the CENPA Building and Contributions inside the Cyclotron Room

To model the contribution of the CENPA building to the source, we pay more attention to the cyclotron room rather than to the rest of the CENPA building. We used the MULTI

and M2CAD14 program, written by Eric Adelberger and Nathan Collins, and AutoCad to model the source near the pendulum.

In our model of the cyclotron room, we take into account the following structures: the cyclotron magnet and coils which are located at the center of cyclotron room, a large excavation under the magnet (pit), the crane 670 cm above the floor, a concrete base and beams connecting the magnet on which the Eöt-wash III apparatus is located, a box filled with sand which is located 123 cm toward the magnet and 121 cm upward from the pendulum (Figure 6.1), the pond above the cyclotron room, the walls of the cyclotron room, the rest of the CENPA building (Figure 6.2), and the dirt covering the building. Table 6.1 contains the effective masses near the pendulum and the description of the structure of the effective masses. Table 6.2 shows the densities and the charge-to-mass ratios used in the source calculation.

Table 6.1: The significant effective masses of the cyclotron room.

Effective mass	Length (cm)	Width (cm)	Height (cm)	Radius (cm)	Mass (Tons)	Material
magnet	521	173	351		147.56	Fe
magnet coils			67	147	71.58	Cu
crane	1168	91	61		5.71	Fe
pit	305	305	221 <sup>†</sup>		0	Air
concrete base	42	143	47		0.65	Concrete
concrete beams	392	15	91		1.18	Concrete
sand box	25	111	86		0.63	Sand
pond			77 <sup>†</sup>	610	90.01	Water
wall of room		25 <sup>‡</sup>	914	610	196.62	Concrete

<sup>†</sup> Depth of the pit and the pond

<sup>‡</sup> Wall thickness of the cyclotron room

Table 6.2: The density and the charge-to-mass ratio ( $B/\mu$  and  $L/\mu$ ) of the sources.

Material	Density (g/cm <sup>3</sup> )	$B/\mu$	$L/\mu$
Fe	7.8	1.00116	0.46556
Cu	7.8	1.00112	0.45636
Concrete	2.2	1.00046	0.50468
Sand	2.6	1.00055	0.49930
Water	1.0	0.99930	0.56202
Dirt <sup>†</sup>	2.2	1.0	0.5
Bedrock <sup>†</sup>	2.7	1.0	0.5

<sup>†</sup> We assume densities,  $B/\mu$ , and  $L/\mu$  of dirt and bedrock.

### 6.3.3 Topological Model of the Mass Distribution Apart from the Building for Ranges of up to 10 km : $1 \text{ m} < \lambda < 10 \text{ km}$

In these ranges, we include the hillside of the University of Washington, the topographical features of Seattle up to 40 km, the bedrock down to 20 km, Lake Washington, and parts of Puget Sound. To model these source we used manually digitized contour maps. We assume the material below the sea level to be dirt (density = 2.2 g/cm<sup>3</sup>). It does not contribute to the effective mass because it is evenly distributed in the horizontal plane. The contribution of Lake Washington and Puget Sound is water (density = 1.0 g/cm<sup>3</sup>). For the bedrock we assume a density of  $\rho = 2.7 \text{ g/cm}^3$ . We take the origin to be the center of mass of the pendulum and use rectangular coordinates with  $\hat{x}$  = East,  $\hat{y}$  = North, and  $\hat{z}$  = up.

From the digitized contour maps, we made 10 sub-maps based on the distance from the pendulum because we needed to describe the source mass near the pendulum precisely. Table 6.3 shows the distances from the pendulum for these maps. “lakes” and “lakeb”

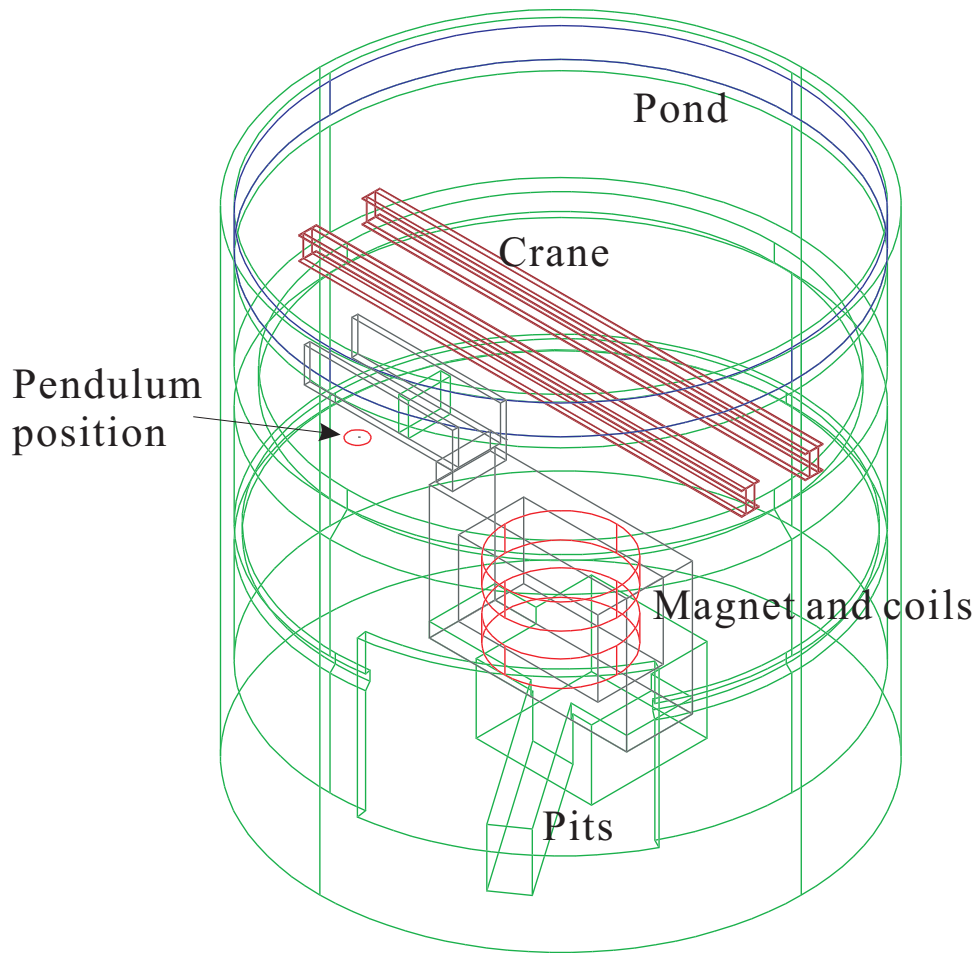


Figure 6.1: Our model of the cyclotron room

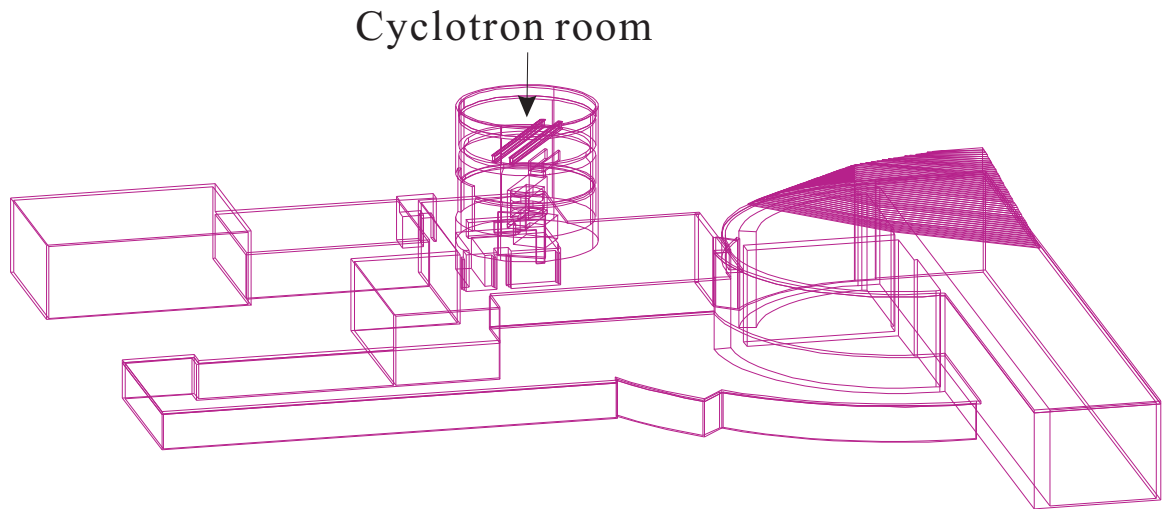


Figure 6.2: Our model of the CENPA Building

Table 6.3: Description of the digitized contour maps.

Maps	Range	# of grid points	Grid size
near	$r_{\perp} \leq 20$ m	$193^3$	20.83 cm
mids	$r_{\perp} \leq 60$ m	$97^3$	1.25 m
midb	$r_{\perp} \leq 180$ m	$97^3$	3.75 m
large	$r_{\perp} \leq 1400$ m	$97^3$	29.17 m
seattle	$r_{\perp} \leq 8$ km	$97^3$	166.67 m
far	$r_{\perp} \leq 40$ km	$97^3$	833.33 m
lakes	$r_{\perp} \leq 1400$ m	$97^3$	29.17 m
lakeb	$r_{\perp} \leq 14$ km	$97^3$	291.67 m
puget	$r_{\perp} \leq 40$ km	$97^3$	833.33 m
bedrock	$r_{\perp} \leq 20$ km	$97^3$	416.67 m

refers to Lake Washington, “puget” is for Puget Sound, and “bedrock” is for bedrock. The first six rows are models of the terrain. We used a commercial program called “Surface Display System” (SDS) to produce a grid file, which has the z-value at evenly spaced grid points. The input to the SDS program were the digitized contour maps, which had randomly distributed data points. The SDS program generated a contour plot based on its regular grid. Table 1.3 shows the number of grid points and grid sizes for the contour maps. The shorter range maps have a smaller grid size. The “near” map ( $r_{\perp} \leq 20$  m) contained more grid points in order to include more detail about nearby the source mass. Figures 6.3 and 6.4 show the SDS output contour maps of the surrounding terrain.

We produced grid files for the terrain (from  $r_{\perp} \leq 20$  m to  $r_{\perp} \leq 40$  km). We integrated each source part separately on the 3-dimensional rectangular grid using the Richardson method[18]. Table 6.4 shows the contribution of  $|\vec{I}_{\perp}|$  for  $q_5 = B$ .

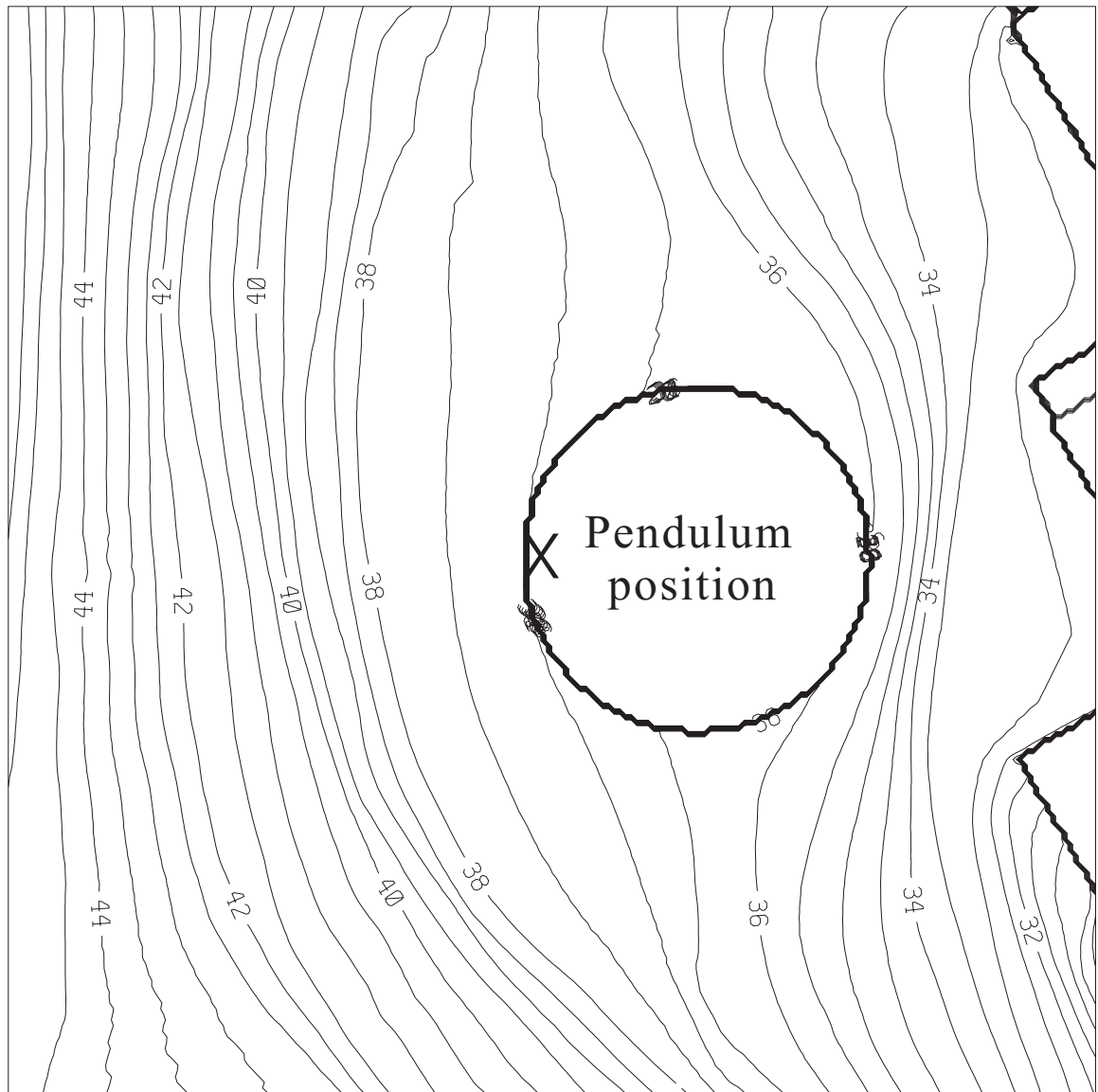


Figure 6.3: Contour line plots made by the SDS program. The typical radius from the pendulum is 20 m. The center of the figure is the location of the pendulum. The circle indicates the excavation of the cyclotron room

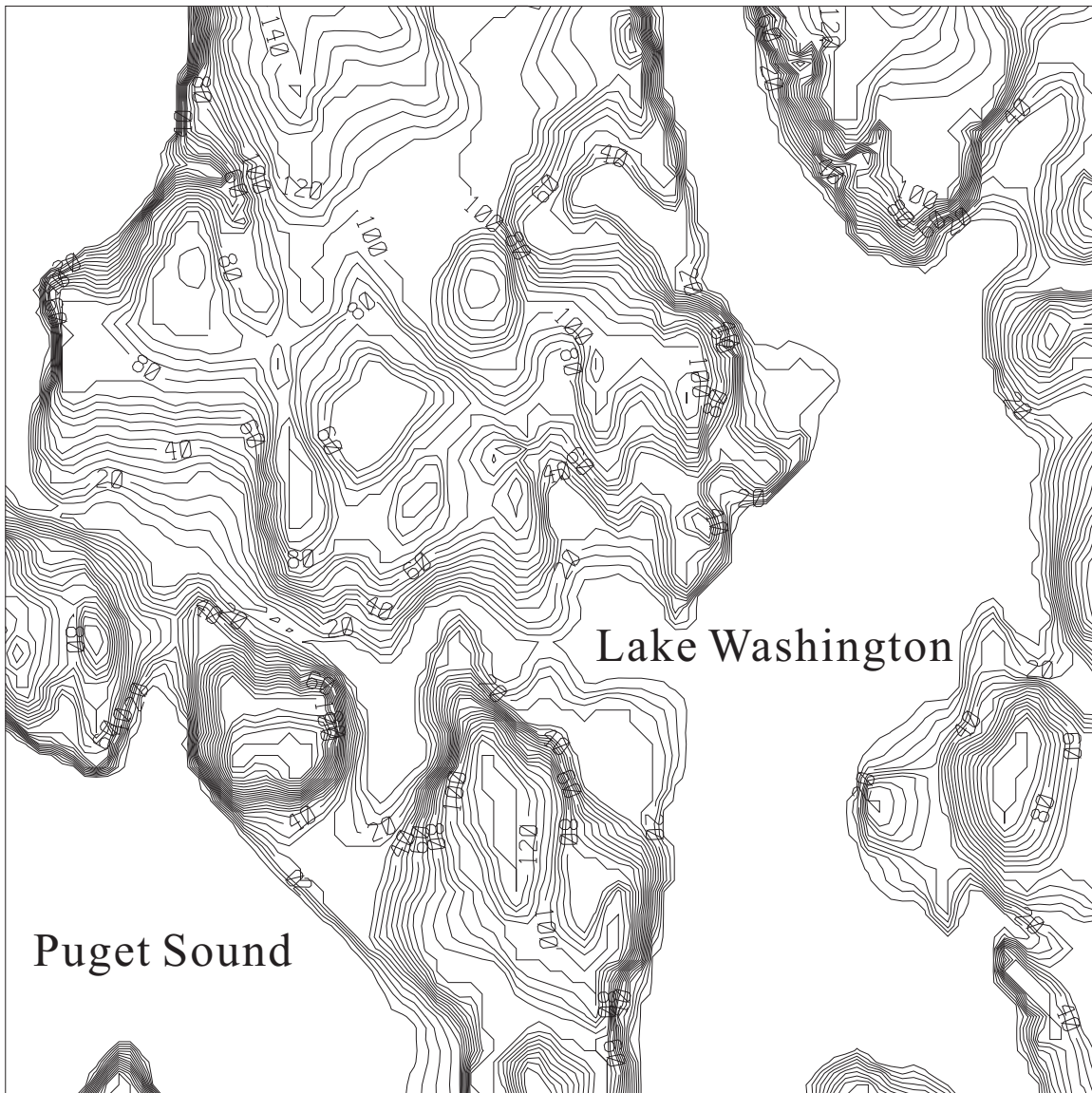


Figure 6.4: Contour line plots made by the SDS program. The typical radius from the pendulum is 8 km. The center of the figure is the location of the pendulum.

Table 6.4: Contributions (in %) to  $|\vec{I}_\perp|$  for  $q_5 = B$ .

$\lambda :$	0.5 m	1 m	10 m	100 m	1000 m	10000 m
CENPA Building	30	10	15	4	2	1
$r_\perp \leq 20$ m	70	90	101	28	10	7
$r_\perp \leq 60$ m	0	0	14	28	11	8
$r_\perp \leq 180$ m	0	0	0	34	19	14
$r_\perp \leq 1400$ m	0	0	0	14	45	37
$r_\perp \leq 8$ km	0	0	0	0	10	33
$r_\perp \leq 40$ km	0	0	0	0	0	18
lake $r_\perp \leq 1400$ m	0	0	0	0	0	0
lake $r_\perp \leq 14$ km	0	0	0	0	1	5
puget $r_\perp \leq 40$ km	0	0	0	0	0	11
bedrock $r_\perp \leq 20$ km	0	0	0	0	14	44

Note: the CENPA building includes objects near the pendulum inside the cyclotron room and the rest of building. The sum of the contributions may be larger than 100% because  $\vec{I}_\perp$  of each contribution can point in a different direction.

### 6.3.4 Model for Long Ranges: $\lambda > 1000 \text{ km}$

In this region, we used the multi-layer ellipsoidal earth model[17]. And we refer to the Preliminary Reference Earth Model (PREM)[19][20] for the density and composition of the earth. Figure 6.5 shows the density of the earth interior as a function of the distance from the center of the earth. Table 6.5 shows the charge-mass ratio of the earth interior.

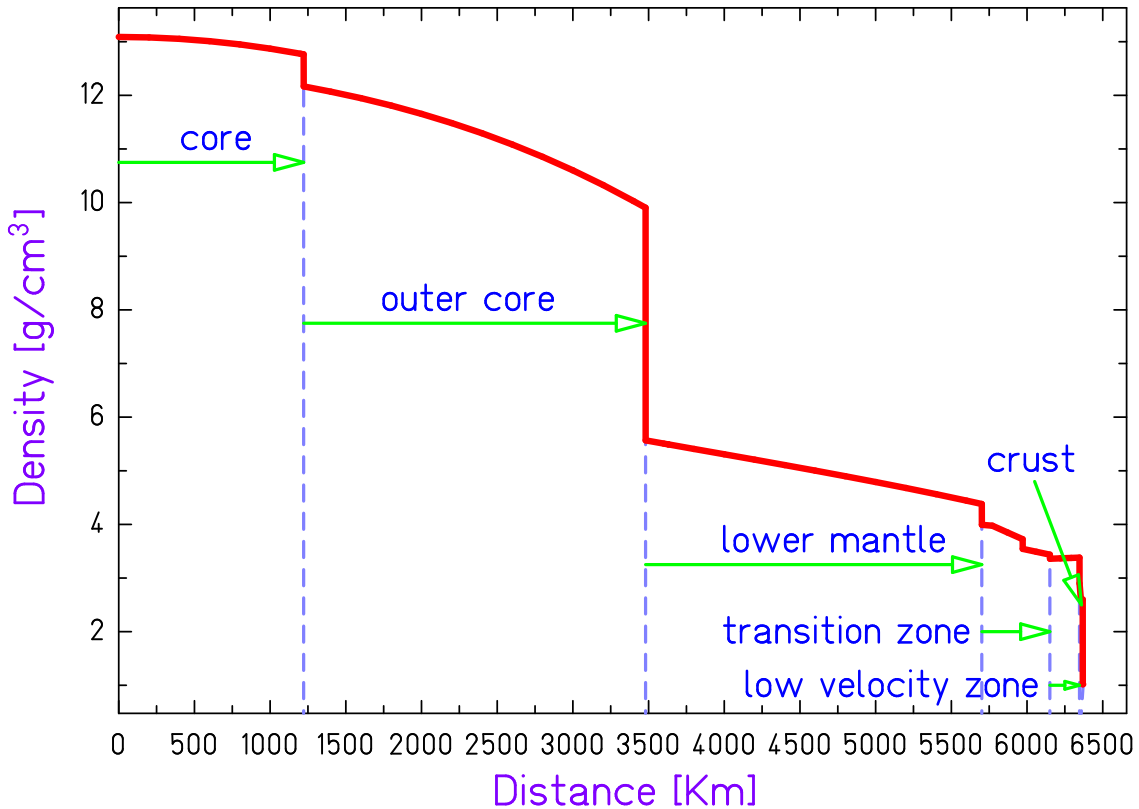


Figure 6.5: Preliminary Reference Earth Model

Table 6.5: The charge-mass ratio of the earth.

Region	$B/\mu$	$L/\mu$
core & outer core	1.00100	0.46780
lower mantle & crust	1.00041	0.49110

#### 6.4 Result and Discussion

Table 6.6 shows the results of the source integration. A list of the magnitude of  $\vec{I}_\perp$  and the direction  $\gamma$  in the NS-WE frame for  $q_5=B$ ,  $L$  and  $(B-L)/\sqrt{2}$  is presented. Figure 6.6 shows our result for  $q_5=B$ .  $|\vec{I}_\perp|$  is getting larger as  $\lambda$  gets bigger because we add more mass such as the hillside of University of Washington and surrounding terrain of the city of Seattle. The increase of  $|\vec{I}_\perp|$  is smaller as  $\lambda$  gets bigger and ceases to grow as the distance gets bigger and the source masses become more homogenous in the horizontal direction. The apparent rolls off near  $\lambda = 10$  km is due to the lack of detail on the contour maps. As  $\lambda$  increases the direction of the  $\vec{I}_\perp$  points toward the west ( $90^\circ$ ) and then turns to the north. For ranges  $\leq 100$  m, near the wall of the cyclotron room and the hillside,  $\vec{I}_\perp$  points to the west. For longer ranges ( $> 100$  m), the north part of Seattle dominates over the lower parts of Seattle to the south, so that the direction of the  $\vec{I}_\perp$  changes from west to north. This result is consistent with intuition. Then, there remains a gap in the prediction of  $\vec{I}_\perp$  between 20 km and 1000 km. This gap is due to of the lack of the information of the earth's interior in that region. Finally, for far ranges ( $> 10000$  km),  $|\vec{I}_\perp|$  becomes a constant at  $1.63 \text{ cm/s}^2$ , which is slightly smaller than  $1.67 \text{ cm/s}^2$ <sup>1</sup> as reported by Su.

---

<sup>1</sup>This value was calculated with the perfect sphere earth model.

Table 6.6: Source strength of Eöt-Wash III experiment.

$\lambda$ (meter)	$q_5 = B$		$q_5 = L$		$q_5 = (B - L)/\sqrt{2}$	
	$ \vec{I}_\perp $ (cm/sec <sup>2</sup> )	$\gamma^*$ (degree)	$ \vec{I}_\perp $ (cm/sec <sup>2</sup> )	$\gamma^*$ (degree)	$ \vec{I}_\perp $ (cm/sec <sup>2</sup> )	$\gamma^*$ (degree)
0.5	$1.10 \times 10^{-5}$	87.9	$5.11 \times 10^{-6}$	87.9	$3.86 \times 10^{-6}$	87.9
1	$4.22 \times 10^{-5}$	87.5	$2.13 \times 10^{-5}$	87.5	$1.48 \times 10^{-5}$	87.6
2	$1.01 \times 10^{-4}$	87.1	$5.14 \times 10^{-5}$	87.1	$3.53 \times 10^{-5}$	87.1
5	$2.24 \times 10^{-4}$	87.1	$1.13 \times 10^{-4}$	87.0	$7.81 \times 10^{-5}$	87.1
10	$3.65 \times 10^{-4}$	88.8	$1.84 \times 10^{-4}$	88.8	$1.28 \times 10^{-4}$	88.9
20	$5.92 \times 10^{-4}$	91.1	$2.98 \times 10^{-4}$	91.0	$2.08 \times 10^{-4}$	91.1
50	$1.09 \times 10^{-3}$	93.3	$5.47 \times 10^{-4}$	93.3	$3.84 \times 10^{-4}$	93.4
100	$1.69 \times 10^{-3}$	93.7	$8.45 \times 10^{-4}$	93.7	$5.95 \times 10^{-4}$	93.7
200	$2.49 \times 10^{-3}$	91.6	$1.25 \times 10^{-3}$	91.5	$8.81 \times 10^{-4}$	91.6
500	$3.71 \times 10^{-3}$	82.6	$1.86 \times 10^{-3}$	82.6	$1.31 \times 10^{-3}$	82.6
1000	$4.76 \times 10^{-3}$	71.2	$2.38 \times 10^{-3}$	71.2	$1.68 \times 10^{-3}$	71.2
2000	$6.12 \times 10^{-3}$	59.5	$3.05 \times 10^{-3}$	59.5	$2.17 \times 10^{-3}$	59.5
5000	$7.19 \times 10^{-3}$	44.1	$3.60 \times 10^{-3}$	44.3	$2.54 \times 10^{-3}$	44.0
10000	$6.80 \times 10^{-3}$	23.0	$3.41 \times 10^{-3}$	30.4	$2.40 \times 10^{-3}$	29.5
20000	$6.11 \times 10^{-3}$	15.3	$3.60 \times 10^{-3}$	16.1	$2.16 \times 10^{-3}$	14.4
...	not calculated		not calculated		not calculated	
$1 \times 10^6$	$4.88 \times 10^{-2}$	0	$2.40 \times 10^{-2}$	0	$1.75 \times 10^{-2}$	0
$2 \times 10^6$	$2.77 \times 10^{-1}$	0	$1.36 \times 10^{-1}$	0	$1.00 \times 10^{-1}$	0
$5 \times 10^6$	$9.47 \times 10^{-1}$	0	$4.65 \times 10^{-1}$	0	$3.41 \times 10^{-1}$	0
$1 \times 10^7$	1.36	0	0.665	0	0.491	0
$2 \times 10^7$	1.54	0	0.757	0	0.554	0
$5 \times 10^7$	1.62	0	0.793	0	0.585	0
$1 \times 10^8$	1.63	0	0.800	0	0.587	0
$2 \times 10^8$	1.63	0	0.802	0	0.585	0

\*  $0^\circ$  is North and  $90^\circ$  is West.

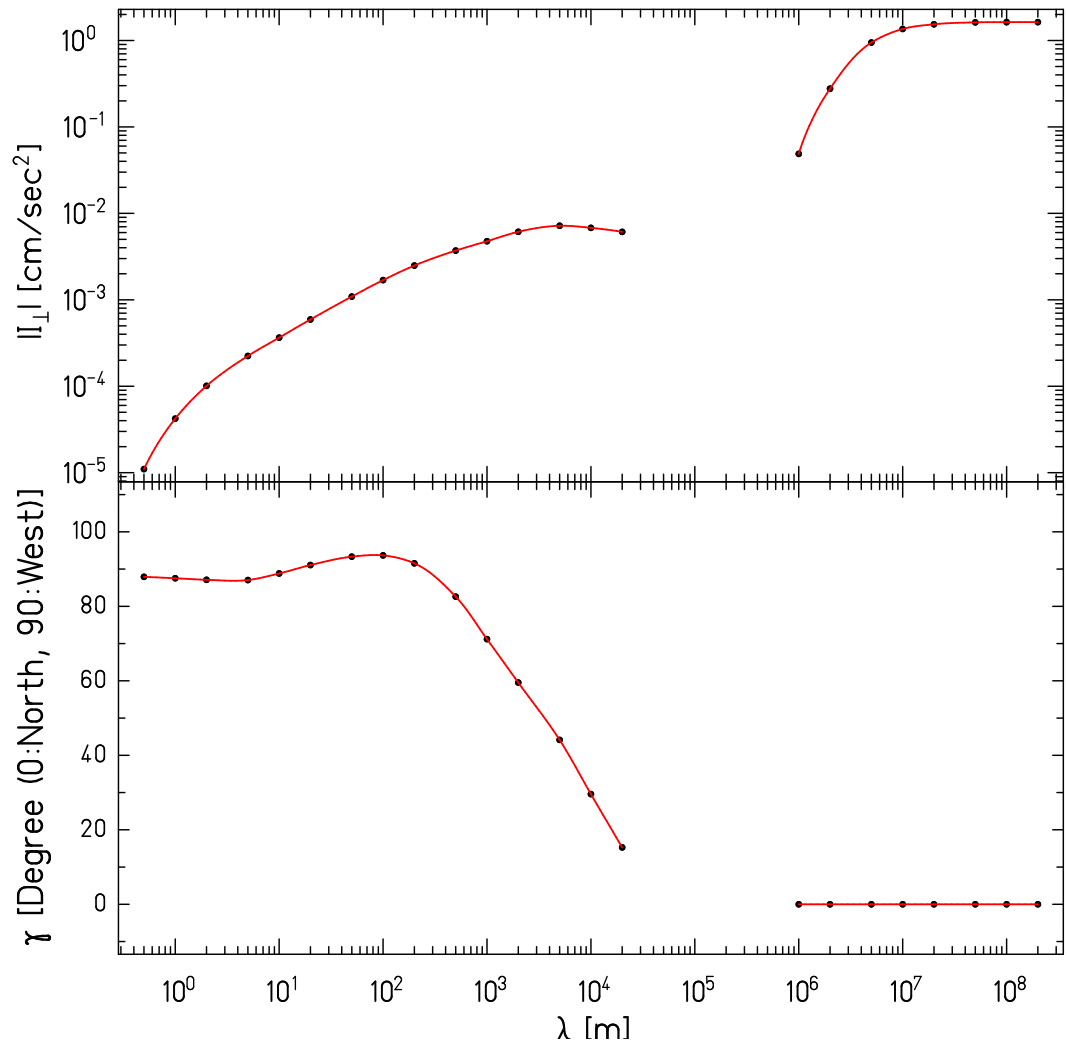


Figure 6.6: The magnitude and direction of  $|\vec{I}_{\perp}|$  for  $q_5=B$

## 6.5 Gravity Gradients

The calculation of the source strength is based on our models. We can test the models by calculating the gravity gradient fields and then comparing them to actual measurements with our apparatus.

### 6.5.1 Predicted Gravity Gradients

The gravitational potential energy for two test masses which have a separation  $r$  is described by

$$V_{12}(r) = -G \frac{m_A m_B}{r}. \quad (6.14)$$

We can generalize the gravitational potential energy between the pendulum and the arbitrary source masses with

$$V(|\vec{r} - \vec{r}'|) = -G \int d^3 r \rho_p(\vec{r}) \int d^3 r' \rho_s(\vec{r}') \frac{1}{|\vec{r} - \vec{r}'|}, \quad (6.15)$$

where  $\rho_p(\vec{r})$  and  $\rho_s(\vec{r}')$  denote the mass distribution densities of the pendulum and the source mass. We expand  $1/|\vec{r} - \vec{r}'|$  with a multipole expansion,

$$\frac{1}{|\vec{r} - \vec{r}'|} = 4\pi \sum_{l=0}^{\infty} \sum_{m=-l}^l \frac{1}{2l+1} \frac{r^l}{r'^{l+1}} Y_{lm}^*(\hat{r}) Y_{lm}(\hat{r}') \quad (6.16)$$

then,

$$V(|\vec{r} - \vec{r}'|) = -4\pi G \sum_{l=0}^{\infty} \frac{1}{2l+1} \sum_{m=-l}^l \int d^3 r \rho_p(\vec{r}) r^l Y_{lm}^*(\hat{r}) \int d^3 r' \frac{\rho_s(\vec{r}')}{r'^{l+1}} Y_{lm}(\hat{r}') \quad (6.17)$$

$$= -4\pi G \sum_{l=0}^{\infty} \frac{1}{2l+1} \sum_{m=-l}^l q_{lm} Q_{lm} \quad (6.18)$$

where

$$q_{lm} = \int d^3 r \rho_p(\vec{r}) r^l Y_{lm}^*(\hat{r}), \quad (6.19)$$

and

$$Q_{lm} = \int d^3 r' \frac{\rho_s(\vec{r}')}{r'^{l+1}} Y_{lm}(\hat{r}'). \quad (6.20)$$

The  $q_{lm}$  are called the gravity gradient moments. These integrals only contain the properties of the pendulum. The  $Q_{lm}$  are called the gravity gradient fields and contain the source mass distribution.

### 6.5.2 The Result of the Calculation of the Gravity Gradient Fields

We calculated the gravity gradient fields ( $Q_{lm}$ ) using the same models as we used for calculation of the source strength. Table 6.7 shows the magnitudes and directions of the gravity gradient fields up to  $l=5$ . The  $Q_{21}$  fields are dominated by the hillside ( $r_\perp \leq 20$  m and  $r_\perp \leq 60$  m) and the CENPA building. The walls of the cyclotron room have the biggest contribution associated with the cyclotron room. For the  $Q_{31}$  field, the magnet compensates the contributions from other objects inside the cyclotron room and the contribution of CENPA building is small. The hillside ( $r_\perp \leq 20$  m and  $r_\perp \leq 60$  m) dominates the most of the  $Q_{31}$  field.

In this calculation, we did not include the “rain effect”, which is caused by a variable water content in the dirt. This variation of  $Q_{21}$  is estimated to be within about 1% of the total  $Q_{21}$ . The maximum gravity gradient field changes due to the rotation of the crane are 0.06% for  $Q_{21}$  and 0.6% for  $Q_{31}$ , respectively.

Table 6.7: The calculated values of  $Q_{lm}$ .

$Q_{lm}$	$ Q_{lm} $	Direction( $^{\circ}$ ) <sup>*</sup>
$Q_{00}(\text{g/cm}^1)$	$2.83 \times 10^{11}$	270.0
$Q_{10}(\text{g/cm}^2)$	$1.28 \times 10^5$	90.0
$Q_{11}(\text{g/cm}^2)$	$3.00 \times 10^4$	163.0
$Q_{20}(\text{g/cm}^3)$	$6.01 \times 10^0$	90.0
$Q_{21}(\text{g/cm}^3)$	$1.93 \times 10^0$	270.9
$Q_{22}(\text{g/cm}^3)$	$4.82 \times 10^{-1}$	261.2
$Q_{30}(\text{g/cm}^4)$	$6.36 \times 10^{-4}$	90.0
$Q_{31}(\text{g/cm}^4)$	$1.06 \times 10^{-3}$	85.2
$Q_{32}(\text{g/cm}^4)$	$1.28 \times 10^{-3}$	81.1
$Q_{33}(\text{g/cm}^4)$	$5.81 \times 10^{-3}$	75.5
$Q_{40}(\text{g/cm}^5)$	$1.03 \times 10^{-5}$	270.0
$Q_{41}(\text{g/cm}^5)$	$9.62 \times 10^{-6}$	266.4
$Q_{42}(\text{g/cm}^5)$	$1.53 \times 10^{-6}$	84.8
$Q_{43}(\text{g/cm}^5)$	$8.37 \times 10^{-6}$	79.6
$Q_{44}(\text{g/cm}^5)$	$2.41 \times 10^{-5}$	71.4
$Q_{50}(\text{g/cm}^6)$	$1.01 \times 10^{-6}$	270.0
$Q_{51}(\text{g/cm}^6)$	$5.49 \times 10^{-7}$	266.4
$Q_{52}(\text{g/cm}^6)$	$3.15 \times 10^{-7}$	262.8
$Q_{53}(\text{g/cm}^6)$	$1.58 \times 10^{-7}$	79.2
$Q_{54}(\text{g/cm}^6)$	$1.51 \times 10^{-7}$	255.6
$Q_{55}(\text{g/cm}^6)$	$5.95 \times 10^{-9}$	345.0

<sup>\*</sup> 0  $^{\circ}$  is North and 90  $^{\circ}$  is West.

Table 6.8: Contributions (in %) to gravity gradient fields  $Q_{21}$  and  $Q_{31}$ .

i	contribution	$ Q_{21} $	$ Q_{31} $
1	cyclotron room wall	41.68	62.81
2	magnet & coils	13.43	83.37
3	concrete base & beams	1.94	12.69
4	sandbox	0.91	5.14
5	crane	0.27	0.93
6	pond	2.56	5.39
7	rest of CENPA Building	4.89	15.72
8	$r_{\perp} \leq 20m$	37.07	83.28
9	$r_{\perp} \leq 60m$	15.84	11.54
10	$r_{\perp} \leq 180m$	3.74	2.90
11	$r_{\perp} \leq 1400m$	0.45	0.70
12	$r_{\perp} \leq 8km$	0.03	0.01
13	$r_{\perp} \leq 40km$	0.00	0.00
14	lake $r_{\perp} \leq 1400m$	0.00	0.00
15	lake $r_{\perp} \leq 14km$	0.01	0.00
16	puget $r_{\perp} \leq 40km$	0.01	0.00
17	bedrock $r_{\perp} \leq 20km$	2.03	0.02

Note: The sum of contributions may be larger than 100% because each contribution can point in different directions.

### 6.5.3 Test the Calculation Result

We measured the gravity gradient fields ( $Q_{21}$  and  $Q_{31}$ ) with a gradiometer pendulum that has exaggerated gravity gradient moments (section 5.1.1). Table 6.9 shows the comparison between the calculated values and the actual experimental values of  $Q_{21}$  and  $Q_{31}$ . The calculation and measurements of the  $Q_{21}$  and  $Q_{31}$  are consistent with 8% and 2% respectively.

These results provide a good test of the model within 100 m from the pendulum because the  $Q_{21}$  and  $Q_{31}$  fields are dominated by mass distribution within 100 m (Table 6.5.2). And we confirm that our topographical model within 100 m from the pendulum is fine with these results because the  $Q_{21}$  and  $Q_{31}$  fields (Equation 6.20) have more  $r'$  dependence than the source strength (Equation 6.10).

Table 6.9: The comparison of the result with measured gravity gradient fields.

Gravity gradient fields	Calculation		Measurement	
	Magnitude	Phase	Magnitude	Phase
$Q_{21}$	1.93 g/cm <sup>3</sup>	270.9°	(1.78 ± 0.01) g/cm <sup>3</sup>	(270.2±0.1)°
$Q_{31}$	$1.06 \times 10^{-3}$ g/cm <sup>4</sup>	85.2°	$(1.08 \pm 0.01) \times 10^{-3}$ g/cm <sup>4</sup>	(74.2±0.2)°

## Chapter 7

### RESULTS AND DISCUSSION

The data taking sequence is summarized in Table 7.1. Only Data set III was used to analyze with the Earth as a source mass. All of Data sets (I, II, and III) were used in the astronomical sources analysis. For the data shown here only Beryllium (Be) and Titanium (Ti) were used to form the composition dipole.

Table 7.1: The summary of data taking sequence.

Data set	Composition dipole configuration	Data taking period
I	Ti - Be	92 days
II	Be - Ti (reversed)	78 days
III	Ti - Be	52 days

#### 7.1 Differential Acceleration in Earth's Field

The results of our analysis (Data set III) toward the Earth are summarized in Table 7.2. Since the tilt and the gravity gradient effects were well resolved, we corrected the final data with these. Table 7.3 summarizes the expected signals from the tilt and gravity gradient effects and all of our systematic uncertainties on Data set III. Table 7.4 summarizes the result corrected with the systematic effects. The final combined the Equivalence Principle violating signals and associated  $1\sigma$  statistical uncertainties and systematic uncertainties (Table 7.4) we get

$$\text{Ti - Be : } a_1^s = (-1.2 \pm 0.4 \pm 0.6) \text{ nrad}, \quad a_1^c = (1.2 \pm 0.4 \pm 0.7) \text{ nrad}, \quad (7.1)$$

where the first uncertainties are the statistical uncertainties and the second are systematic uncertainties. The corresponding horizontal differential acceleration<sup>1</sup>

$$\Delta a_{\perp} = a_{\perp}^{Ti} - a_{\perp}^{Be} = [(-7.7 \pm 4.8) \hat{n} + (8.0 \pm 5.3) \hat{w}] \times 10^{-13} \text{ cm/s}^2 \quad (7.2)$$

where  $\hat{n}$  and  $\hat{w}$  are unit vectors pointing north and west, respectively. The uncertainties were given by the quadrature sum of the statistical and systematic uncertainties.

Table 7.2: The summary of results for analyzing toward the Earth (included local masses).

Data set	data cycle	North-South component	East-West component
III	1	( 0.4 ± 0.9) nrad	(-0.2 ± 0.8) nrad
	2	(-1.8 ± 0.8) nrad	(-0.4 ± 0.8) nrad
	3	(-1.1 ± 0.8) nrad	( 0.6 ± 0.9) nrad
	4	(-0.7 ± 0.9) nrad	( 0.3 ± 0.8) nrad
	mean value	(-0.8 ± 0.4) nrad	( 0.1 ± 0.4) nrad

All the uncertainties are  $1\sigma$  statistical uncertainties.

## 7.2 Differential Acceleration toward Astronomical Sources

All of the uncertainties in this section are statistical because the systematic uncertainties are negligible. For example, the tilt of the Data set III modulated with a sidereal day toward the Sun yields  $4.2 \times 10^{-2}$  nrad. This could produce a systematic effect of  $\pm 2.1 \times 10^{-3}$  nrad.

The differential accelerations<sup>1</sup> toward the Sun and associated  $1\sigma$  statistical uncertainties are

$$\Delta a^{sun}(\text{Ti-Be}) = (1.1 \pm 1.6) \times 10^{-13} \text{ cm/s}^2, \quad (7.3)$$

$$\Delta a^*(\text{Ti-Be}) = (-0.2 \pm 1.6) \times 10^{-13} \text{ cm/s}^2, \quad (7.4)$$

---

<sup>1</sup>The + sign states that the Ti test mass is more attracted toward the source mass than the Be test mass.

Table 7.3: The combined signals from the systematic effect corrections.

Data set	data cycle	North-South component	East-West component
III	1	( 0.2 ± 0.6) nrad	(-1.4 ± 0.7) nrad
	2	( 0.1 ± 0.6) nrad	(-1.3 ± 0.7) nrad
	3	( 1.0 ± 0.6) nrad	(-0.8 ± 0.7) nrad
	4	( 0.1 ± 0.6) nrad	(-1.2 ± 0.7) nrad
	mean value	(0.4 ± 0.6) nrad	(-1.1 ± 0.7) nrad

All the uncertainties are  $1 \sigma$  systematic uncertainties (see Table 5.12).

Table 7.4: The result corrected with the systematic effects.

Data set	data cycle	North-South component	East-West component
III	1	( 0.2 ± 0.9 ± 0.6) nrad	( 1.3 ± 0.8 ± 0.7) nrad
	2	(-1.8 ± 0.8 ± 0.6) nrad	( 0.9 ± 0.8 ± 0.7) nrad
	3	(-2.0 ± 0.8 ± 0.6) nrad	( 1.3 ± 0.9 ± 0.7) nrad
	4	(-0.8 ± 0.9 ± 0.6) nrad	( 1.5 ± 0.8 ± 0.7) nrad
	mean value	(-1.2 ± 0.4 ± 0.6) nrad	( 1.2 ± 0.4 ± 0.7) nrad

The first uncertainties are the statistical uncertainties and the second are systematic uncertainties.

where  $\Delta a^{sun}$  is the differential acceleration toward the sun and  $\Delta a^*$  is a quadrature acceleration. Table 7.5 summarizes the results of our analysis toward the sun.

Table 7.5: The summary of results for analyzing toward the Sun.

Data set	data cycle	$\Delta a^{sun}$ (cm/s <sup>2</sup> )	$\Delta a^*$ (cm/s <sup>2</sup> )
I	1	$(4.1 \pm 5.6) \times 10^{-13}$	$(1.3 \pm 5.6) \times 10^{-13}$
	2	$(-0.6 \pm 6.4) \times 10^{-13}$	$(0.4 \pm 6.4) \times 10^{-13}$
	3	$(3.9 \pm 4.5) \times 10^{-13}$	$(0.7 \pm 4.5) \times 10^{-13}$
	4	$(-1.0 \pm 4.1) \times 10^{-13}$	$(-0.6 \pm 4.1) \times 10^{-13}$
	mean value	$(1.5 \pm 2.5) \times 10^{-13}$	$(0.3 \pm 2.5) \times 10^{-13}$
II	1	$(-0.4 \pm 4.7) \times 10^{-13}$	$(0.2 \pm 4.7) \times 10^{-13}$
	2 & 3	$(3.8 \pm 3.8) \times 10^{-13}$	$(-0.5 \pm 3.8) \times 10^{-13}$
	4	$(-4.3 \pm 6.2) \times 10^{-13}$	$(0.4 \pm 6.2) \times 10^{-13}$
	5	$(-2.6 \pm 7.3) \times 10^{-13}$	$(-8.3 \pm 7.3) \times 10^{-13}$
	mean value	$(1.1 \pm 2.5) \times 10^{-13}$	$(-1.1 \pm 2.5) \times 10^{-13}$
III	1 & 2	$(-3.4 \pm 4.7) \times 10^{-13}$	$(4.6 \pm 4.7) \times 10^{-13}$
	3 & 4	$(6.0 \pm 5.7) \times 10^{-13}$	$(-5.0 \pm 5.7) \times 10^{-13}$
	mean value	$(0.4 \pm 3.6) \times 10^{-13}$	$(0.8 \pm 3.6) \times 10^{-13}$
mean value all		$(1.1 \pm 1.6) \times 10^{-13}$	$(-0.2 \pm 1.6) \times 10^{-13}$

All the uncertainties are statistical uncertainties.

The differential accelerations toward the galactic center and associated  $1\sigma$  statistical uncertainties are

$$\Delta a^{gal}(\text{Ti-Be}) = (0.4 \pm 1.7) \times 10^{-13} \text{ cm/s}^2, \quad (7.5)$$

$$\Delta a^*(\text{Ti-Be}) = (0.3 \pm 1.7) \times 10^{-13} \text{ cm/s}^2, \quad (7.6)$$

where  $\Delta a^{gal}$  is the differential acceleration toward the galactic center and  $\Delta a^*$  is a quadra-

ture acceleration. Table 7.6 summarizes the results of our analysis toward the galactic center.

Table 7.6: The summary of results for analyzing toward the galactic center.

Data set	data cycle	$\Delta a^{gal}$ (cm/s <sup>2</sup> )	$\Delta a^*$ (cm/s <sup>2</sup> )
I	1	$(5.8 \pm 6.3) \times 10^{-13}$	$(-2.0 \pm 6.3) \times 10^{-13}$
	2	$(1.1 \pm 7.0) \times 10^{-13}$	$(3.1 \pm 7.3) \times 10^{-13}$
	3	$(4.1 \pm 4.8) \times 10^{-13}$	$(-6.6 \pm 4.8) \times 10^{-13}$
	4	$(-1.3 \pm 4.4) \times 10^{-13}$	$(-1.2 \pm 4.4) \times 10^{-13}$
	mean value	$(2.0 \pm 2.7) \times 10^{-13}$	$(-0.4 \pm 2.7) \times 10^{-13}$
II	1	$(0.2 \pm 4.9) \times 10^{-13}$	$(0.6 \pm 4.9) \times 10^{-13}$
	2 & 3	$(-4.5 \pm 4.0) \times 10^{-13}$	$(-4.4 \pm 4.0) \times 10^{-13}$
	4	$(5.4 \pm 6.7) \times 10^{-13}$	$(1.5 \pm 6.7) \times 10^{-13}$
	5	$(-8.7 \pm 8.0) \times 10^{-13}$	$(2.6 \pm 8.0) \times 10^{-13}$
	mean value	$(-2.0 \pm 2.7) \times 10^{-13}$	$(0.5 \pm 2.7) \times 10^{-13}$
III	1 & 2	$(-2.1 \pm 4.9) \times 10^{-13}$	$(4.8 \pm 4.9) \times 10^{-13}$
	3 & 4	$(7.7 \pm 6.1) \times 10^{-13}$	$(-4.4 \pm 6.1) \times 10^{-13}$
	mean value	$(1.8 \pm 3.8) \times 10^{-13}$	$(1.1 \pm 3.8) \times 10^{-13}$
mean value all		$(0.4 \pm 1.7) \times 10^{-13}$	$(0.3 \pm 1.7) \times 10^{-13}$

All the uncertainties are statistical uncertainties.

The differential accelerations in the direction of the cosmic microwave background (CMB) dipole and associated  $1\sigma$  statistical uncertainties are

$$\Delta a^{CMB}(\text{Ti-Be}) = (-0.6 \pm 1.5) \times 10^{-13} \text{ cm/s}^2, \quad (7.7)$$

$$\Delta a^*(\text{Ti-Be}) = (-0.5 \pm 1.5) \times 10^{-13} \text{ cm/s}^2, \quad (7.8)$$

where  $\Delta a^{CMB}$  is the differential acceleration toward the direction of the cosmic microwave background (CMB) dipole and  $\Delta a^*$  is a quadrature acceleration. Table 7.7 summarizes the results of our analysis toward the direction of the cosmic microwave background (CMB) dipole.

Table 7.7: The summary of results for analyzing toward the direction of the cosmic microwave background (CMB) dipole.

Data set	data cycle	$\Delta a^{gal}$ (cm/s <sup>2</sup> )	$\Delta a^*$ (cm/s <sup>2</sup> )
I	1	$(0.2 \pm 5.5) \times 10^{-13}$	$(2.8 \pm 5.5) \times 10^{-13}$
	2	$(-4.5 \pm 6.4) \times 10^{-13}$	$(1.8 \pm 6.4) \times 10^{-13}$
	3	$(-1.8 \pm 4.3) \times 10^{-13}$	$(5.2 \pm 4.3) \times 10^{-13}$
	4	$(0.7 \pm 3.9) \times 10^{-13}$	$(-1.2 \pm 3.9) \times 10^{-13}$
	mean value	$(-0.9 \pm 2.4) \times 10^{-13}$	$(1.9 \pm 2.4) \times 10^{-13}$
II	1	$(0.2 \pm 4.5) \times 10^{-13}$	$(-2.4 \pm 4.5) \times 10^{-13}$
	2 & 3	$(0.7 \pm 3.7) \times 10^{-13}$	$(-5.3 \pm 3.7) \times 10^{-13}$
	4	$(-2.3 \pm 6.0) \times 10^{-13}$	$(3.7 \pm 6.0) \times 10^{-13}$
	5	$(-2.6 \pm 7.0) \times 10^{-13}$	$(-9.6 \pm 7.0) \times 10^{-13}$
	mean value	$(-0.3 \pm 2.4) \times 10^{-13}$	$(-3.5 \pm 2.4) \times 10^{-13}$
III	1 & 2	$(-3.1 \pm 4.5) \times 10^{-13}$	$(-2.5 \pm 4.5) \times 10^{-13}$
	3 & 4	$(3.0 \pm 5.3) \times 10^{-13}$	$(4.7 \pm 5.3) \times 10^{-13}$
	mean value	$(-0.6 \pm 3.4) \times 10^{-13}$	$(0.4 \pm 3.4) \times 10^{-13}$
mean value all		$(-0.6 \pm 1.5) \times 10^{-13}$	$(-0.5 \pm 1.5) \times 10^{-13}$

All the uncertainties are statistical uncertainties.

### 7.3 Conclusion

#### 7.3.1 Test of the Equivalence Principle

##### *Test of the Equivalence Principle in the Earth's Field*

The differential acceleration limits given in Equation 7.2 imply  $1\sigma$  limits on violation of the Equivalence Principle in the field of the Earth

$$\eta(\text{Ti},\text{Be}) = \frac{\Delta a_{\perp} \cdot \hat{n}}{g \sin \delta} = \left( \frac{m_g}{m_i} \right)_{\text{Ti}} - \left( \frac{m_g}{m_i} \right)_{\text{Be}} = (-4.7 \pm 2.4) \times 10^{-13}. \quad (7.9)$$

Here we used  $g = 981 \text{ cm/s}^2$  and  $\delta = 1.67 \times 10^{-3}$  is the angle between the local vertical and a line passing through our laboratory and the center of the earth.

##### *Test of the Equivalence Principle Toward the Sun*

The differential acceleration limits given in Equation 7.3 imply  $1\sigma$  limits on violation of the Equivalence Principle in toward sun of

$$\eta(\text{Ti},\text{Be})^{sun} = \frac{\Delta a^{sun}}{a_{sun}} = (1.9 \pm 2.7) \times 10^{-13}. \quad (7.10)$$

Here we used  $a_{sun} = 0.593 \text{ cm/s}^2$  is the acceleration toward the sun [8].

##### *Test of the Equivalence Principle Toward Galactic Dark Matter*

Since 25% of the differential acceleration towards the center of our galaxy is caused by galactic dark matter[21], we can test the equivalence principle for ordinary matter falling towards galactic dark matter. The acceleration of the Solar System toward the galactic center is

$$a_{gal} = \omega_{gal}^2 R_{gal} = 1.9 \times 10^{-8} \text{ cm/s}^2 \quad (7.11)$$

where  $\omega_{gal} \approx 8.4 \times 10^{-16} \text{ rad/s}$  is the rotation frequency of the our Galaxy and  $R_{gal} \approx 8.5 \text{ kpc}$  is the distance from the Sun to the galactic center. Since 25% of the differential acceleration towards the center of our galaxy is caused by galactic dark matter[21], we

assumed that

$$a_{gal}^{DM} \approx 5 \times 10^{-9} \text{ cm/s}^2. \quad (7.12)$$

The differential acceleration limits given in Equation 7.5 imply  $1\sigma$  limits on violation of the Equivalence Principle in toward the galactic dark matter of

$$\eta(\text{Ti,Be})^{DM} = \frac{\Delta a^{gal}}{a_{gal}^{DM}} = (0.7 \pm 3.4) \times 10^{-5}. \quad (7.13)$$

*Test of the Equivalence Principle in the Direction of the Cosmic Microwave Background (CMB) Dipole*

Our local group of galaxies is moving about 600 km/s with respect to the frame in which the cosmic microwave back ground (CMB) is isotropic[22][23]. We estimated the corresponding acceleration by this peculiar velocity by the Hubble time  $t_H = 1/H_0$ , where  $H_0 \approx 85 \text{ km s}^{-1}\text{Mpc}^{-1}$  [24], to obtain  $a_{CMB} = 1.7 \times 10^{-10} \text{ cm/s}^2$ . This allowed us to test the equivalence principle for laboratory objects in the direction of the cosmic microwave back ground (CMB). The differential acceleration limits given in Equation 7.7 imply  $1\sigma$  limits on violation of the Equivalence Principle in toward the cosmic microwave background (CMB) dipole direction of

$$\eta(\text{Ti,Be})^{CMB} = \frac{\Delta a^{CMB}}{a_{CMB}} = (-3.6 \pm 8.9) \times 10^{-4}. \quad (7.14)$$

### 7.3.2 Constraints on New Yukawa Interactions

To set upper limits on new composition dependent interaction, our limits on differential acceleration given by Equation 7.2 combined with the calculation of source strength (Table 6.6). Figure 7.1 shows  $2\sigma$  upper limit on the new Yukawa interaction for  $q_5 = B$ .

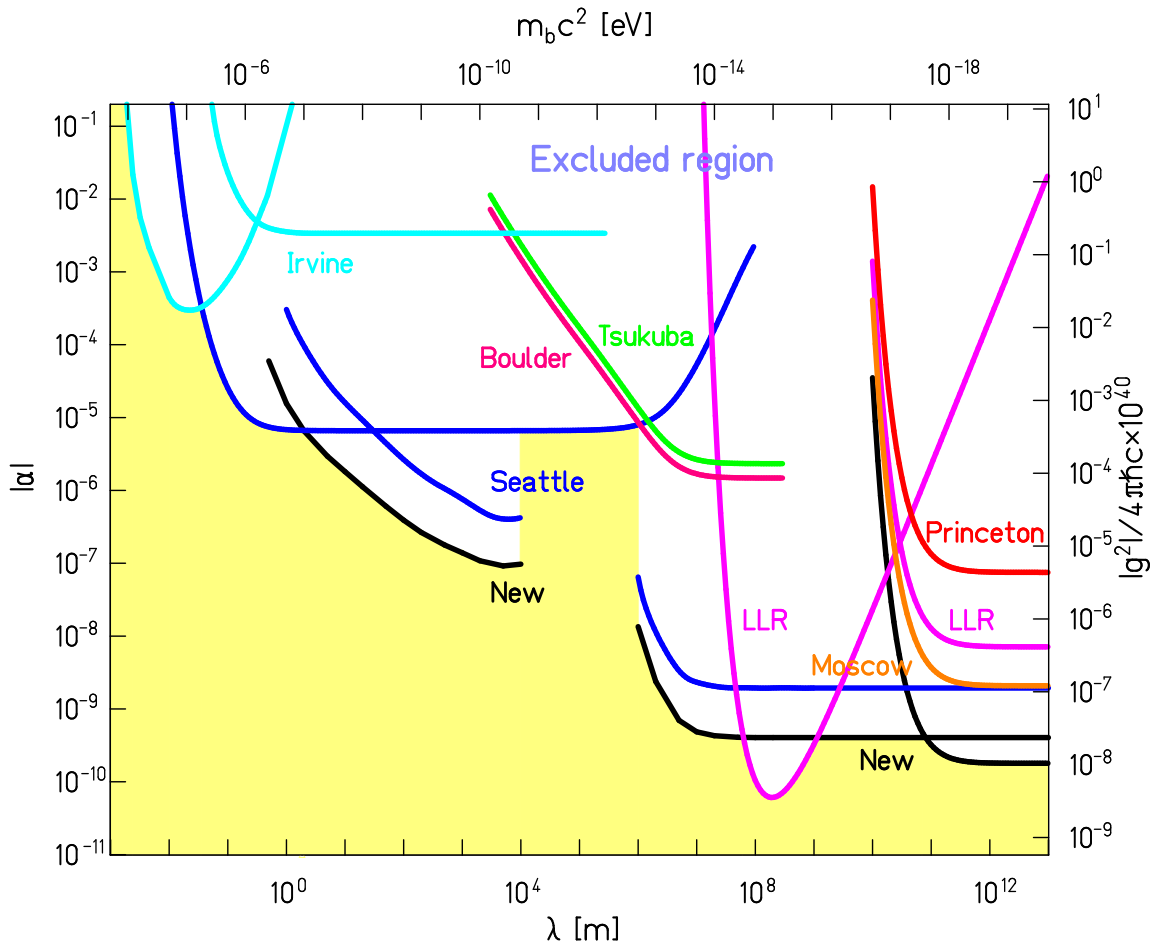


Figure 7.1: New  $2\sigma$  upper limit on the Yukawa interactions with  $q_5 = B$ . The previous results labeled as follows: Seattle[8][9], Irvine[10][11], Tsukuba[12], Boulder[13], Moscow[14], Princeton[15], and LLR[16]. The curves labeled New are from this work.

## BIBLIOGRAPHY

- [1] T. Damour and A.M. Polyakov. *Gen. Rel. Grav.*, 26:1171, 1994.
- [2] J.P. Ostiker and P. Steinhardt. *Science*, 300:1909, 2003.
- [3] V. Trimble. *Annu. Rev. Astron. Astrophysics.*, 25:425, 1987.
- [4] S. Tremane. *Physics Today*, 45(2):28, 1992.
- [5] T. Damour and K. Nordtvedt. *Phys. Rev. D*, 48:3436, 1994.
- [6] R.R. Caldwell, R. Dave, and P.J. Steinhart. *Phys. Rev. Lett.*, 80:1582, 1998.
- [7] S.M. Carroll. *Phys. Rev. Lett.*, 81(15):3067, 1998.
- [8] Y. Su, B.R. Heckel, E.G. Adelberger, J.H. Gundlach, M. Harris, G.L. Smith, and H.E. Swanson. *Phys. Rev. D*, 50:3614, 1994.
- [9] G.L. Smith, C.D Hoyle, J.H. Gundlach, E.G. Adelberger, B.R. Heckel, and H.E. Swanson. *Phys. Rev. D*, 61:022001, 1999.
- [10] J.K. Hoskins, R.D Newman, R. Spero, and J. Schultz. *Phys. Rev. D*, 32:3084, 1985.
- [11] P.G Nelson, D.M. Graham, and R.D Newman. *Phys. Rev. D*, 42:963, 1987.
- [12] K. Kuruda and N. Mio. *Phys. Rev. D*, 42:3903, 1990.
- [13] T.M. Niebauer, M.P. MacHugh, and J.E. Faller. *Phys. Rev. Lett.*, 59:609, 1987.
- [14] V.G. Braginsky and V.I. Panov. *Sov. Phys. JETP*, 34:463, 1972.
- [15] P.G. Roll, R. Krotkovand, and R.H. Dicke. *Ann. phys. (N.Y.)*, 26:442, 1964.
- [16] J.G Williams, X.X. Newhall, and J.O. Dickey. *Phys. Rev. D*, 53(12):6730, 1996.
- [17] Yue Su. *A New Test of the Weak Equivalence Principle*. PhD thesis, University of Washington, 1992.

- [18] Germund Dahlquist. *Numerical Methods*. Prentice-Hall, Inc., 1974.
- [19] A.M. Dziewonski and D.C. Anderson. *Phys. Earth Planet. Inter.*, 25:297, 1980.
- [20] J.W. Morgan and E. Anders. *Proc. Natl. Acad. Sci.*, 77:6973, 1980.
- [21] C.W. Stubbs. *Phys. Rev. Lett.*, 70(2):119, 1993.
- [22] P. Lubin *et al.* *Astrophys. J. Lett.*, 298:L1, 1985.
- [23] G.F. Smoot *et al.* *Astrophys. J. Lett.*, 396:L1, 1992.
- [24] J.P. Huchra. *Science*, 256:321, 1992.

## VITA

Ki-Young Choi was born in Seoul, Korea on October 8, 1968. He attended Sogang University in Seoul, Korea and earned a B.S. in Physics in 1991. He served in the Korean army for 3 years. He began to work with the Eöt-Wash Gravity Group in July 1999. He earned his M.S degree in 2000 and entered the University of Washington Ph.D. program in the same year. He is married to Sangyi Lee and they have a son Eric Sung-Moo Choi.